STELLAR COMPANIONS TO

A LUCKY IMAGING SURVEY OF TRANSITING EXOPLANET SYSTEMS

EXOPLANET HOST STARS

BY MARIA WÖLLERT

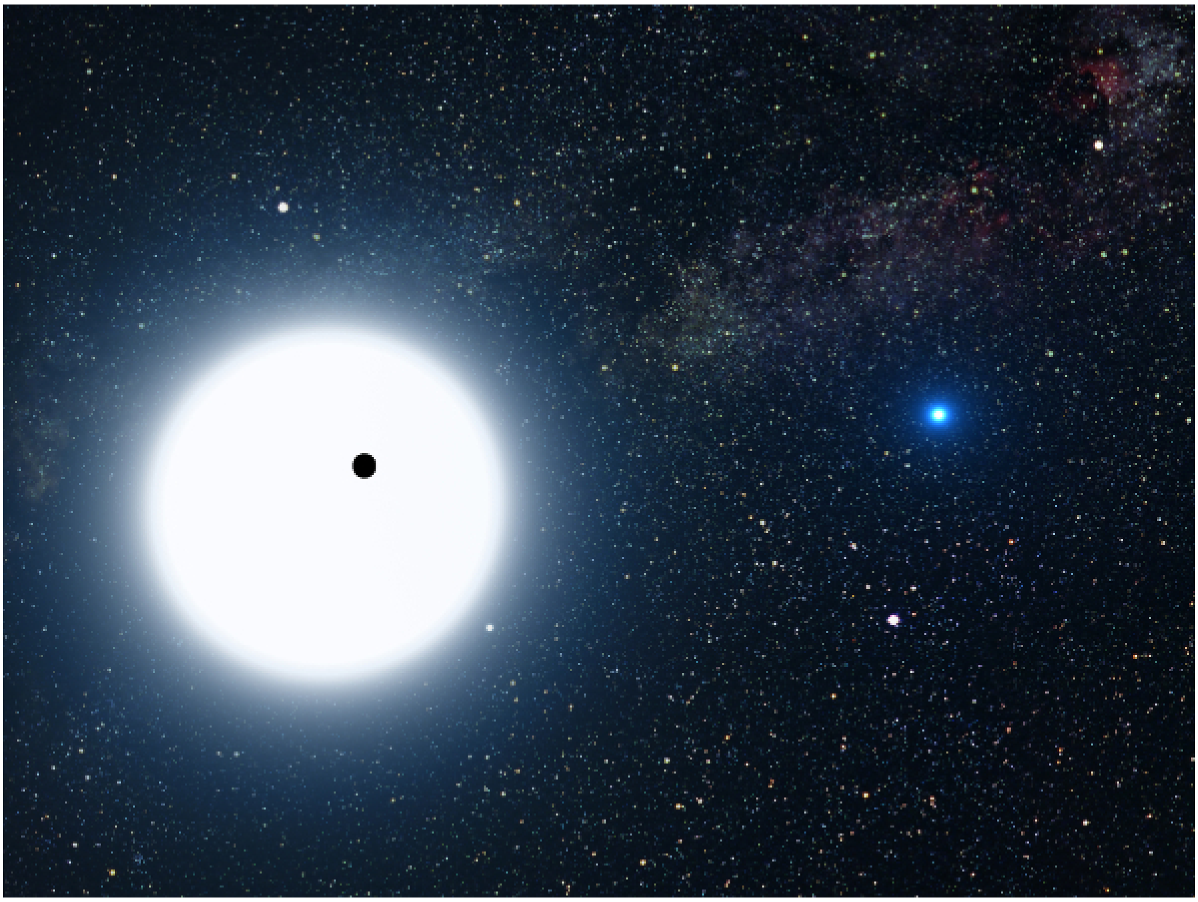

Dissertation submitted to the Combined Faculties for the
Natural Sciences and for Mathematics of the
Ruperto-Carola Universtity of Heidelberg, Germany
for the degree of Doctor of Natural Sciences

Put forward by Dipl.-Phys. Maria Wöllert,
born in Potsdam-Babelsberg, Germany.
Oral examination: February 4, 2016

Stellar companions to exoplanet host stars:
A Lucky Imaging survey of transiting exoplanet systems

Referees: Prof. Dr. Thomas Henning
Prof. Dr. Joachim Wambsganß

Zusammenfassung

Etwa die Hälfte aller Sterne in der Sonnenumgebung sind Teil eines Doppel- oder Mehrfachsystems. Dennoch ist wenig bekannt darüber, inwiefern stellare Begleiter die Entstehung und Entwicklung von Planetensystemen beeinflussen. Zum Beispiel könnten stellare Begleiter die Einwärtswanderung von Heißen Jupitern vereinfachen oder, abhängig von den Systemparametern, eine Abweichung zwischen der Planetenumlaufbahn und der Rotationsachse des Muttersterns hervorrufen. Ferner können ungesehene Doppelsternkomponenten die Bestimmung der Planeteneigenschaften in Transitsystemen verfälschen.

In der vorliegenden Doktorarbeit stelle ich die Ergebnisse unserer Lucky-Imaging-Suche nach stellaren Begleitern um mehr als 100 Sterne mit Transitplaneten vor. Neben der Charakterisierung der Begleiterkandidaten berechne ich mit zwei verschiedenen statistischen Ansätzen die Wahrscheinlichkeit, dass die gefundenen Sterne gravitativ gebunden sind und ich untersuche, ob ein Zusammenhang zwischen der Doppelsternhäufigkeit und dem Vorhandensein von Heißen Jupitern mit parallelen bzw. gekippten Umlaufbahnen besteht. Ich bestimme überdies den Einfluss unaufgelöster stellarer Begleiter auf die ermittelten Planetenparameter und berechne insbesondere die Radiusänderung für zwei Planeten.

Zusätzlich präsentiere ich fotometrische und spektroskopische Beobachtungen von dem jungen Doppelstern HD 102077, für den ich neue Orbitparameter bestimme, wie auch den Spektraltyp der beiden Komponenten, ihre Raumbewegung und ihr Alter. Diese Daten nutze ich, um zu überprüfen, ob HD 102077 einer Bewegungsgruppe angehört.

Abstract

About half of all nearby stars are part of a binary or multiple star system, yet little is known about how multiplicity affects the formation and subsequent evolution of planetary systems. For instance, stellar companions may promote the inward migration of massive planets into very short orbits or cause misalignment between the planetary orbit and the stellar spin axis depending on the properties of the system. Moreover, the ignorance about the presence of a close stellar companion to a transiting exoplanet host star may introduce biases in the derivation of planetary parameters.

In this thesis, I present the results of our Lucky Imaging search for stellar companions around more than 100 transiting exoplanet host stars. Besides characterizing the companion candidates, I calculate the probability that the companion candidates are gravitationally bound using two different statistic approaches, and I look for a correlation between binarity and hot Jupiters with aligned/misaligned orbits. I calculate the effect of unresolved stellar companions on the deduced planetary parameters, in particular the correction for the radii for two planets.

Additionally, I present photometric and spectroscopic observations of the young binary HD 102077 for which I determine the orbital parameters, the spectral type of the two components, the space motion, age, and moving group membership.

Contents

1

Introduction

Since the proposition of the heliocentric model by Nicolaus Copernicus in 1543 (Copernicus, 1543) many philosophers and scientists have been speculating that planets could exist around stars other than the sun (e.g. Newton, 1687). Now we know: they exist and we found them at diverse places in manifold configurations. But first things first. The first exoplanetary system was discovered in 1992, surprisingly not around a main sequence star, but the millisecond pulsar PSR 1257+12 (Wolszczan & Frail, 1992). The presence of planets closer than 1 AU around this object was very unlikely due to the violence of the supernova explosion and the accompanying mass loss that leads to the ejection of planetary companions due to the virial theorem. It took three more years until the first planet around the main-sequence solar type star 51 Pegasi was announced (Mayor & Queloz, 1995). Again the system was different than expected from only knowing our solar system as 51 Peg b is a gas giant that orbits its star in a few stellar radii distance only.

Since then, almost 2000[1] planets have been found mainly by radial velocity or transit measurements. Especially the Kepler space observatory (Borucki et al., 2010; Batalha et al., 2013; Burke et al., 2014) yielded a huge amount of planets and planetary candidates by continuously monitoring the brightness of more than 145 000 main sequence stars. Yet, also techniques with a smaller planet yield as Direct imaging, gravitational microlensing, pulsar timing and astrometry made important detections as they are sensitive to planets at different separations, distances, or with different ages compared to radial velocity and transit searches. The observed configurations of planetary systems are diverse. Besides massive planets located very close to their host star, planets with

---

[1] As of August 2015 on exoplanet.eu

very eccentric or inclined orbits in single or multi-planet systems have been found. Some of the multi-planet systems are closely packed (Lissauer et al., 2011). In addition, a lot of planets have been found in binary/multiple stellar systems. This diversity challenged the first planet formation theories and provoked a huge number of studies about the open questions: How do planets form? What mechanisms are responsible for the evolution of the planetary system architecture? Which conditions are needed for life to occur?

In this work, I focus on one aspect of the first two questions and I investigate binarity as one possible mechanism to shape planetary systems. So far about 15 circumbinary planets around eclipsing binaries (P-type orbit) both in close $\sim 1\,\mathrm{AU}$ (Doyle et al., 2011; Welsh et al., 2012; Orosz et al., 2012) and wide $\gtrsim 100\,\mathrm{AU}$ (Currie et al., 2014) orbits have been found. Yet, planets can also circle around one of the two components (S-type orbit). In this case, the binary stars are usually more widely separated to allow for a stable planetary system and a lot of them can be resolved by high resolution imaging techniques. These are the systems that I look for in this work using Lucky Imaging. Up to date, about 100 of them are known (e.g. Ginski et al., 2012; Ngo et al., 2015). The detections of binary systems make it possible to study the occurrence rate of planets in binary/multiple stellar systems, but also allow to study the correlation of planetary and binary properties which sets constraints on planet formation and evolution theories. It additionally enables us to unbias planetary bulk and atmospheric properties from primary and secondary eclipse measurements for those systems where an unknown star is situated within the photometric aperture during the eclipse observations and added light to the light curve.

Besides the search for stellar companions to transiting planet host stars, I investigated the young, K-type binary system HD 102077 which was proposed as a candidate member of the TW Hydrae association. In determining the age of the system using different age indicators as well as its kinematic properties taking its orbital motion into account I show that HD 102077 is most likely not a member of this or any other young moving group.

In the following of this introduction, I will first review transiting exoplanet systems in detail since those are the targets of our search. At the start of my thesis a fair amount of them lacked high-resolution imaging. Then I will discuss the effects of close stellar sources, both chance alignments and true companions, on eclipse measurements and how binarity is believed to influence planet formation and evolution. Finally, I will describe the Lucky Imaging technique which I used throughout my thesis.

1.1 Transiting exoplanets

Transiting exoplanets are planets that happen to pass in front or behind their parent star from the observers view, thus masking a small part of the star or hiding behind it, respectively. Obviously, chances are low to observe a transiting system. A hot Jupiter with $R_p \approx R_J$ and $P \approx 3$ days around a solar type star will transit in 10% of all possible orbit configurations, an Earth-sized planet in an Earth-size orbit in only 0.5%. That is the reason why most transiting surveys observe large areas of the sky. This approach works very successfully. By now, ground based surveys as SuperWASP (Pollacco et al., 2006) and HATNet (Bakos et al., 2002) and space based surveys as CoRoT (Baglin et al., 2007) and Kepler yielded thousands of planets in total, both in single and multiple planet systems. Most discoveries came from the Kepler satellite whose large aperture and space location allowed the measurement of extremely high precision, consecutive light-curves. Though Kepler is not fully functioning any longer, future missions like CHEOPS (Broeg et al., 2013), TESS (Ricker et al., 2014), and PLATO (Rauer et al., 2014) will detect many more transiting planets. Transiting exoplanets offer the unique opportunity to learn something about the planetary composition since the radius and the mass of these objects can be determined when transit observations and radial velocity data are combined as I will describe in the following. To show the variety of planetary properties, the mass-radius diagram of known exoplanet systems is plotted in Fig. 1.1.

1.1.1 Determine mass, radius, and orbital parameters

The shape of a transiting light curve contains many information about the star-planet system. First of all the transit depth is directly related to the ratio of the radius of the planet to the radius of the star, leading to a stronger dim for a bigger planet independently of its separation, i.e. the hot Jupiter planet from our example above creates a transit depth of $d \approx 1\%$ and the Earth-size planet of $d \approx 0.01\%$ when passing in front of their solar-type host stars. Secondly, the duration of the transit is determined by the radius of the star and the orbital semi-major axis of the planet, it is about $\tau \approx 3\,\mathrm{hr}$ for the hot Jupiter and $\tau \approx 15\,\mathrm{hr}$ for the Earth-sized planet in the Earth-like orbit. Thirdly, the duration of the partial phases of the transit, e.g. when the planet does not fully cover the star, allows to extract the inclination of the system.

For planetary systems with only one planet, transit measurements alone do not allow to determine the mass or eccentricity of the planet (Southworth, 2015). In fact, it is not even possible to be sure about the planetary nature of the object as brown dwarfs and late M dwarfs have similar radii than Jupiter mass planets (see also Fig. 1.1). In addition, blended eclipsing binaries and instrumental effects can mimic planetary transits, and a misclassification of a red giant host star as a main-sequence star from photometry can also lead to an erroneous detection. The number of these false candidates depends very much on the survey layout. For ground based surveys, typically 7% (e.g. Hellier et al., 2011) turn out to be planetary mass companions. For the CoRoT 27 cm-space telescope 6% of the candidates were later confirmed. In contrast, the rate of true planetary companions is much higher for the 1.4 m Kepler telescope due to its higher resolution and the observed field which is out of the Galactic plane where contamination by eclipsing binaries in the background becomes much less likely. It is roughly 90% (Fressin et al., 2013). Consequently, transiting planet candidates need to be confirmed using a different detection method, usually radial velocity (RV) measurements, or by showing that false-alarm scenarios are very unlikely. The latter has been done for a number of Kepler targets as most of them are too faint to achieve the required signal-to-noise ratio to measure velocity variations of the star due to the planet. Radial velocity observations are, however, also an important source of information on the planetary system. Firstly, the radial velocity semi-amplitude can be used to determine the minimum mass of the planet $M_P \sin i$ if the star mass is known. Secondly, the eccentricity and the argument of periastron of the planetary orbit can be inferred. Putting this together with the information from the transit light curve fit, the system parameters are almost determined. Still, an additional constraint is needed, e.g. the stellar mass or radius. It is usually inferred from the spectroscopic properties of the host star using stellar evolutionary models. This introduces, however, systematic uncertainties by 0.6% and more on the planetary mass depending on the model used (Southworth, 2015). Besides compositional variations of the planets, this may be one reason for the observed scattering in the mass-radius relation of transiting exoplanets in Fig. 1.1 especially for the lower mass planets. Note that in the near future the Gaia parallax measurements and the resulting luminosity estimates can replace the additional constraint.

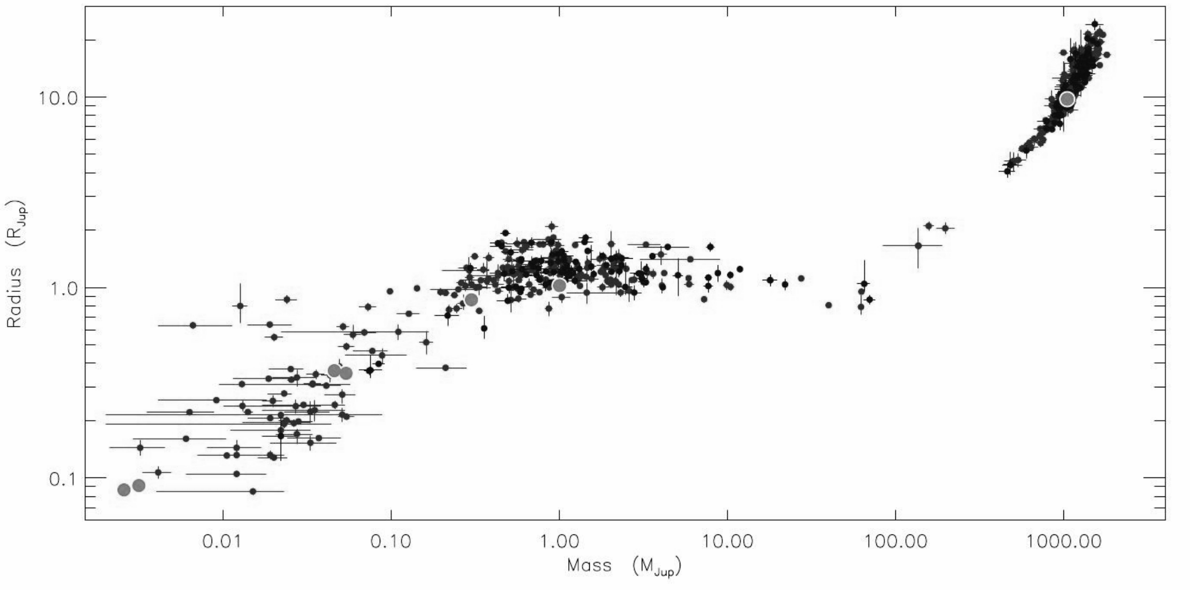

Figure 1.1: Mass-radius diagram for transiting exoplanets and their host stars. The grey circles indicate the bodies of the solar system. (Figure adapted from Southworth (2015)).

In multi-planet systems the situation is easier. Hundreds of them have been found by the Kepler Mission and their false positive rate is very low. The gravitational interaction between the planets leads to deviations of the strict periodicity of the transits, the so-called transit timing variations (TTVs). Space based missions with their ability to observe many consecutive transits with high precision can detect even small perturbations and are thus sensitive to additional transiting and non-transiting planets in the system, i.e. with a TTV variation of five minutes, the Kepler-19 system indicates the presence of a second, non-visible planet (Ballard et al., 2011). TTVs also help to determine the maximum mass of a planet or put narrow constraints on the planetary masses and radii if the orbits are close, e.g. for Kepler-36 (Carter et al., 2012) and Kepler-88 (Barros et al., 2014) TTVs permitted a more precise determination of the planetary radii and masses. In circumbinary planets, the transit timing variation is due to the orbital motion of the stars rather than an additional planet. These planets can easily be confirmed by the transit duration variation method (TDV) where the changes of the transit duration are considered. Kepler-16b is an example of successful application of the TDV (Welsh et al., 2014).

For close, massive planets the minimum mass can also be inferred from light variations due to relativistic beaming (Loeb & Gaudi, 2003). This technique is based on the idea that the gravitational interaction between the planet and the star leads to a variation of the density of photons during the orbit from the observer's viewpoint. Though this effect is very small compared to the emitted and reflected starlight from the planet, it can be applied to distant stars and fast-rotating stars which are usually discarded by RV measurements due to their low signal-to-noise spectra or broad spectral lines. It also allows to measure the eccentricity of the orbit. In 2013, Kepler-76b was detected by this method (Faigler et al., 2013).

1.1.2 Studying planetary atmospheres

Transiting exoplanets also allow to study planetary atmospheres via transmission spectroscopy or secondary eclipse measurements. In transmission spectroscopy one uses the fact that while the planet transits its star, some rays of light travel through the upper atmosphere of the planet and imprint characteristic features. For example, in the infrared, molecules such as H_2O, CO, CO_2 and CH_4 are predicted. The presence of water absorption has now been shown in several hot Jupiters, for example, in HD 209458b and XO-1b via observations with the Hubble Space Telescope (Deming et al., 2013). In contrast, some planets show featureless transmission spectra, e.g. the Neptune-mass exoplanet GJ 436b (Knutson et al., 2014). This could indicate either high-altitude clouds or a hydrogen-poor atmospheric composition.

Although the star is much brighter than the planet, the light of the planet can be detected in some cases. For example, when the planet passes behind its host star the small dip in the total brightness of the system shows its contribution. If the secondary eclipse is observed in different wavelength bands, the spectrum of the irradiated "day-side" of the planet can be inferred. In this way the temperature of the planet and some atmospheric properties as cloud coverage and the chemical composition can be inferred. The reflected light of the star dominates in the optical whereas the thermal emission of the planet dominates in the infrared. That's why a lot of the secondary eclipse measurements made use of the multiple infrared channels of the Spitzer Space Telescope. The first exoplanet investigated by this technique was the hot Jupiter TrES-1b (Charbonneau et al., 2005). It was observed with Spitzer at 4.5 µm and 8.0 µm which yielded an effective temperature of $T_{\mathrm{eff}} = 1060\,\mathrm{K} \pm 50\,\mathrm{K}$ and an albedo of $A = 0.31 \pm 0.14$. This method also helps to constrain the eccentricity and the argument of periastron.

The reflected light variations of short-period planets during a full orbit can also be used to detect or characterise planets. Although the effect is small, a couple of planets have been discovered that way, e.g. Kepler-70b and Kepler-70c (Charpinet et al., 2011). As this effect does not need planetary transits to occur, space-based surveys may find quite a bunch of those planets in the future. In addition, the phase curve helps to constrain the thermal properties of giant planets and their atmosphere, e.g. the size distribution of particles in the atmosphere.

1.1.3 Measuring the spin-orbit angle

The angle Ψ between the stellar spin axis and the orbital axis of the planet is called stellar obliquity or spin-orbit angle. It allows important insights in the dynamical history of planetary systems. Several mechanisms are believed to influence the spin orbit angle. Firstly, the primordial alignment of the protoplanetary disk with the star is important. The disk may be misaligned with respect to the stellar equator due to strong magnetic fields (Lai et al., 2011) or by the gravitational torque from a companion star (Batygin, 2012). Secondly, during and after the disk dissipation planet-planet scattering (Ford & Rasio, 2008), the Lidov-Kozai effect with a companion star, and the resonance between the binary and planetary orbit (Touma & Sridhar, 2015) may lead to misaligned orbits (Malmberg et al., 2007). Thirdly, originally misaligned orbits may be realigned by tidal interaction with the star (Albrecht et al., 2012; Xue et al., 2014).

The spin-orbit angle can be measured by different means. Firstly, the distortion of the spectral line profile during transit (see Fig. 1.2), the so called Rossiter-McLaughlin effect, can be measured. This method only gives the sky-projected value λ of the stellar obliquity. Secondly, if the planet transits over a starspot several times, the relative motion of the spot to the planet can be measured and thus the spin-orbit angle. For instance, the sky-projected spin orbit angle of WASP-19 was measured to $\lambda = 1.0° \pm 1.2°$ using multi-band photometry of two transits (Tregloan-Reed et al., 2013). With 3 or more observations of the same starspot at different positions even Ψ can be determined. Thirdly, for fast rotating stars the inhomogeneity of the stellar surface gravity and hence surface brightness can be used to estimate Ψ, for example $\Psi = 60° \pm 2°$ was found for Kepler-13Ab using this method (Masuda, 2015).

By now, the spin orbit angle has been measured for about 90 systems[2], mainly hot Jupiters, and a significant fraction has misaligned or even retrograde orbits. Most of the misaligned planetary orbits are found around hot stars ($T_{\mathrm{eff}} > 6250\,\mathrm{K}$) (Winn, 2011).

---

[2] Number from TEPCat (http://www.astro.keele.ac.uk/jkt/tepcat/)

This finding could, however, also be explained by the younger ages of those systems (Triaud, 2011) and thus the shorter time for tidal interaction between planet and star.

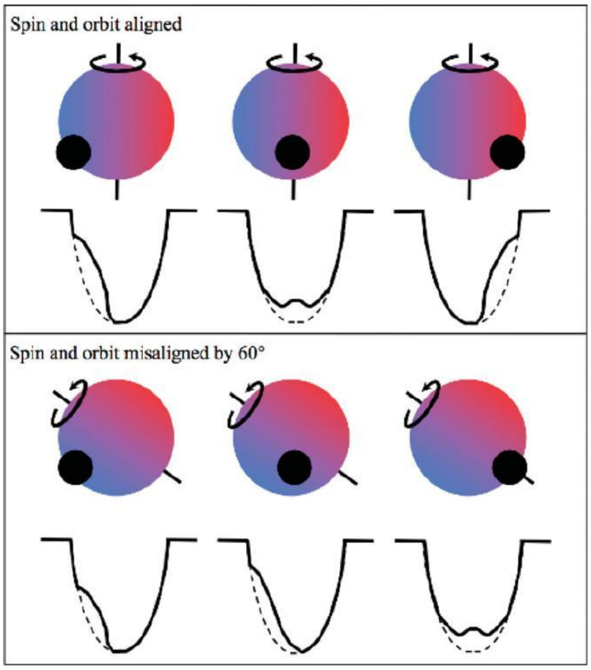

Figure 1.2: The Rossiter-McLaughlin effect occurs during a transit. It results in a distortion of the spectral line profile. The sketch shows the spectral line shape for three successive phases of a transit, on top of the image for an aligned orbit, at the bottom for a spin-orbit angle of $\Psi = 60°$ (Figure taken from Winn (2011)).

1.2 Multiplicity of transiting exoplanet host stars

1.2.1 Properties of binary/multiple systems

Observations of protostars show that most, if not all, stars are born in multiple systems (e.g. Larson, 1972). The mechanism responsible for that is generally believed to be the collapse and fragmentation of molecular cloud cores (Goodwin et al., 2007). With time the multiplicity fraction decreases due to close encounters with other systems in the dense birth environment or dynamical interaction among the components (Chen et al., 2013). Still, 46% of solar-type field stars in the solar neighbourhood are part of a binary (75%) or higher-order multiple (25%) system (Raghavan et al., 2010). The separation of stars in multiple systems spans a huge range; the separation distribution of solar-type stars is shown in Fig. 1.3. It is well fitted by a Gaussian in $\log a$ with a mean of approximately 50 AU (Raghavan et al., 2010). For lower mass stars the peak goes to smaller separations of 4 AU – 30 AU (Fischer & Marcy, 1992; Janson et al., 2014). The

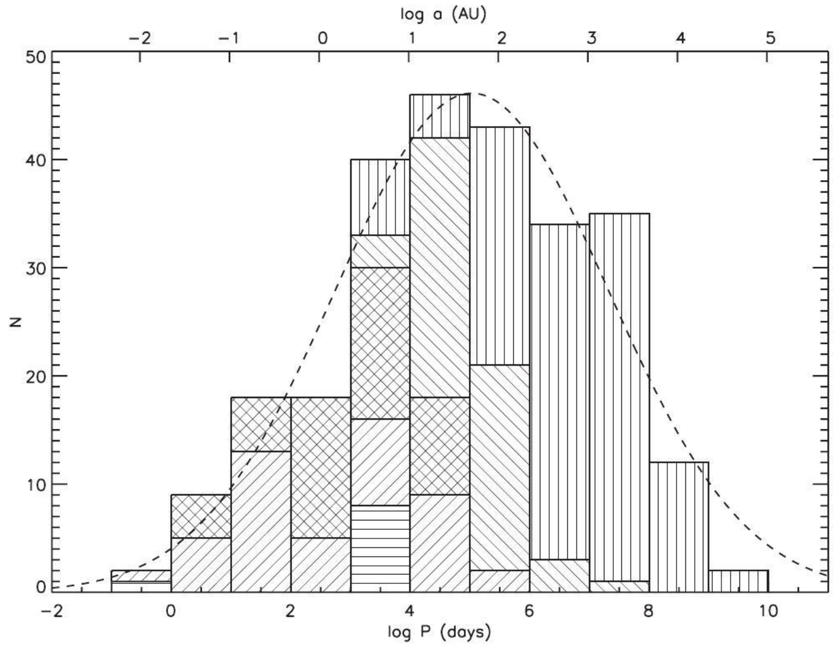

Figure 1.3: Separation distribution of solar-type stars. The pattern of the boxes indicates by which method the companions were found. Spectroscopic binaries are plotted with positively sloped lines, visual binaries with negative sloped lines, common proper motion pairs with vertical lines and unresolved companions with horizontal lines. The data are nicely fitted by a Gaussian with a peak at $\log P = 5.03$ days and $\sigma_{\log P} = 2.28$. The semi-major axis corresponds to a system with a total mass of $1.5 M_\odot$ (Figure taken from Raghavan et al. (2010)).

orbits of very close binaries with periods smaller than 12 days are usually circularised due to tidal interactions between the components. Most binaries in wider orbits are, however, eccentric with a nearly flat distribution out to about $e \approx 0.6$ followed by a slow drop (Raghavan et al., 2010). Binaries in eccentric orbits spend a longer time near apastron compared to periastron. This has the effect that for many configurations the instantaneous projected separation and the true semi-major axis differ by only about 5% (van Albada, 1968). The mass ratio distribution of binaries is flat between $q = 0.2$ to $q = 0.95$. Lower mass ratios are less common; equal mass pairs are somewhat more likely. The like-mass pairs usually reside in short period orbits of less than a few hundred years, whereas the unequal-mass pairs are mostly found in orbits with longer periods (Raghavan et al., 2010).

1.2.2 Planet formation and evolution in multiples

The formation of planets is strongly linked to the formation of stars. While the star forms by the gravitational collapse of a molecular cloud core, the infalling material possesses some amount of angular momentum which leads to the formation of a circumstellar disk. In that disk the planets form. The planet formation scenarios that are generally supported are core accretion (Pollack et al., 1996; Lissauer & Stevenson, 2007) and gravitational instability (Cameron, 1978; Boss, 1997). To explain very wide, massive planetary companions hundreds of AU away from their host star, the collapse of a molecular cloud core as for the formation of binary systems is sometimes evoked (Bate, 2012).

In the core-accretion scenario dust particles in the circumstellar disk start to coalesce and gradually grow through collisions with other particles to larger and larger clumps, eventually becoming planetesimals and planets. If the planets reach $10-15$ Earth masses (Mizuno, 1980), they will accrete a huge amount of gas in a short time and become gas giants. Due to the large amounts of solids needed to form such large cores and the long timescales involved, planet migration and disk evolution are usually assumed for the formation of giant planets outside of $5\,\mathrm{AU} - 10\,\mathrm{AU}$ from the host star (Rafikov, 2011) in order to accrete enough mass before the disk dissipates (Alibert et al., 2005). The planet formation efficiency in the core-accretion scenario depends very strongly on the metallicity of the system. High metallicity leads to a faster formation of planetary cores and leaves more time to accrete gas (Johansen et al., 2009). A correlation between metallicity and planet occurrence rate has indeed been observed. Planets around metal-rich stars are more abundant than planets around metal-poor stars (Fischer & Valenti, 2005). Note, however, that the formation of kilometre sized bodies is still enigmatic (Johansen et al., 2014).

Planets further outside, for instance the outer planets of the HR 8799 system, may have formed by gravitational instability. In the gravitational instability model, giant planets form by the gravitational collapse and fragmentation of large scale spiral structures in the circumstellar disk. The capacity of a disk to form fragments is generally described by the Toomre criterion (Toomre, 1981) and the cooling efficiency (Gammie, 2001). A disk becomes unstable if the Toomre parameter is smaller one and hence the surface density large and if the cooling is fast enough. These conditions can be only met at large separations ($\gtrsim 50\,\mathrm{AU}$) from the star in more massive disks (Vazan & Helled, 2012). If planets are formed this way, they form on relatively short time scales of $\lesssim 10\,000$ years at a few dozen AU and are massive ($1\,\mathrm{M_{jup}} - 10\,\mathrm{M_{jup}}$) (Rogers & Wadsley, 2012).

After the in-situ formation, the planetary orbits are subject to drastic changes. The most important mechanism is the interaction of the planets with the disk which can lead to large variations of the semi-major axis, the eccentricity and the inclination. Though eccentricity and inclination are usually damped quickly, the semi-major axis may increase or decrease permanently, depending on the planet-to-star mass ratio and the properties of the disk (see Baruteau et al., 2014, for a review on planet-disk interaction). Additional planetary companions may also modify the orbit and the migration path of each other (see also Davies et al., 2014, for a detailed review on the long-term dynamical evolution of planetary systems). For instance, planets can enter in mean-motion resonance and move inwards or outwards, keeping the relation of their orbits. A system of three or more planets can also get unstable and the least massive planet can be ejected on a very eccentric and wide orbit (Chatterjee et al., 2008; Veras & Mustill, 2013).

Moreover, the presence of gravitationally bound stellar companions can influence planet formation and evolution in multiple ways. Many, partly contradicting effects have been seen in numerical simulations: In a binary system the circumstellar disk is typically truncated (Artymowicz & Lubow, 1994; Pichardo et al., 2005) which leaves less material for planet formation. The disk material is dynamically heated which may hinder gravitational collapse since spiral structures do not grow or fragment but decay (Nelson, 2000; Mayer et al., 2005). The heating may or may not reduce the condensation of solid material required for core accretion depending on the disk mass (Mayer et al., 2005). In addition the lifetime of disks in close binaries is reduced compared to single stars and wide pairs (Cieza et al., 2009; Kraus & Hillenbrand, 2009) and thus gas giants should be rare in those systems, if the dominant planet formation mode is core accretion.

A stellar companion can also influence the planetary system after the disk dispersal. If the orbit of the companion is tilted with respect to the planetary orbit ($i > 39.2°$), it will induce periodic oscillation on the planet's eccentricity and inclination (Kozai, 1962; Malmberg et al., 2007). In a multi-planet system this may lead to strong planet-planet interactions, which can result in the ejection of one or more components. It can also lead to a giant planet in a close orbit, if the inclination i of the system and thus the eccentricity of the planet is very high and tidal dissipation occurs during the pericentre passage. Interestingly, also wide stellar companions in planar orbits can lead to strong perturbations or ejection of planets due to the perturbations of the binary orbit by other stars (Kaib et al., 2013) or resonance between the orbital motion of the binary and the orbital precession of the planets in a multi-planet system (Touma & Sridhar, 2015).

Despite simulations are predicting that both, close and wide, binaries can hinder the planet formation, a lot of planets have been found in multiple stellar systems. Especially the Kepler mission allowed for some studies on the influence of binarity on exoplanetary systems as it found a huge number of planets and is not influenced by the selection bias of radial velocity planet searches. Wang et al. (2014) used Adaptive Optics imaging of 56 Kepler planet host stars and find that planet formation is decreased in multiple systems with separations $\lesssim 1500\,\mathrm{AU}$. However, Horch et al. (2014) have observed over 600 Kepler objects of interest using speckle-imaging and claim that the exoplanet host stars have a similar binary fraction than field stars. In accordance to that, (Deacon et al., 2015) comes to the conclusion that wide binary companions with projected separations $a > 3000\,\mathrm{AU}$ do not influence planet formation.

In addition to studying the correlation between binarity and orbit parameters, the detection of sources within a few arcsec of a planet host star is important to measure accurate radii of the planets themselves. We need precise radii estimates (up to $\approx$ 20%) especially for the smaller planets to infer from the density whether the planet is comprised of silicates and iron and thus Earth-like or contains voluminous layers of hydrogen, helium and ices (Rogers, 2015). As discussed above, this is not possible from using transit data alone as the pixel size of the instruments usually exceeds a few arcsec due to the large field of view, e.g. for the Kepler candidate list the factor by which the radius is underestimated due to multiplicity is 1.49 ± 0.12 on average for targets without follow-up observations. For targets with typical follow-up observations (2 to 3 radial velocity measurements over 6 to 9 month, spectroscopy of the primary star, and high resolution imaging) this factor reduces to 1.20 ± 0.06 (Ciardi et al., 2015). In addition, the planet's infrared emission spectrum can be underestimated by more than 10% (Crossfield et al., 2012). This shows how crucial those observations are to understand planetary compositions and atmospheres. It does not matter for this correction, whether the star is part of the system or not. Its constant additional flux on the light curve is sufficient to bias primary and secondary eclipse interpretations.

1.3 The Lucky Imaging technique

Since atmospheric turbulence degrades both the spatial resolution and the sensitivity of the telescope, high-angular resolution imaging is needed to access the close environment of a star (about $0.1'' - 2''$) and search, e.g. for stellar or substellar companions. While very faint targets as exoplanets are only visible from the ground with higher order Adaptive Optics at the largest optical telescopes, close stellar companions can be detected at mid-sized telescopes with faster and low cost high-angular resolution techniques as Lucky Imaging. To understand the Lucky Imaging approach, I will first discuss the atmospheric effects on the incoming stellar light, followed by the Lucky Imaging observing and data reduction strategy.

1.3.1 The turbulent atmosphere

Let us first consider an ideal telescope situated in space. The angular resolution of such a telescope is diffraction limited and can be approximated by the Full Width Half Maximum (FWHM) of the Point Spread Function (PSF)

$$\text{FWHM(diffraction limited)} = \lambda / D$$

where λ is the wavelength of the observed radiation and D the telescope diameter. In ground-based observations this angular resolution is, however, seldom reached. The reasons for this are temporal and local variations of the temperature and pressure in the atmosphere. They lead to fluctuations of the refractive index of air and cause phase differences of the incoming wavefronts. Quantitatively, the atmospheric turbulence is well described by the statistic treatment of Kolmogorow (Kolmogorov, 1941). He assumes that energy is injected at large scales where large eddies form. The large eddies eventually break up into smaller and smaller eddies until the eddies are so small that the energy is dissipated by viscous friction. The resulting turbulence can be described by characteristic values.

The first parameter is called the Fried parameter or atmospheric coherence length r_0. It corresponds to the circular area in which the wavefront error is smaller than $\lambda/6$ and the wavefront can be approximated as planar. For a long exposure this value sets the telescope resolution to

$$\text{FWHM(seeing limited)} = \lambda/r_0.$$

r_0 varies with $\lambda^{6/5}$, which means that the atmospheric seeing is better at longer wavelengths. For example, r_0 ranges between 20 cm to 40 cm in the I-band for good observing sites, corresponding to a seeing of $0.45''$ to $0.9''$.

The second important parameter is the atmospheric coherence time. It corresponds to the time after which the variance of the observed wavefront changes by $1\,\text{rad}^2$. If the eddy pattern changes much slower than the time needed to transport the eddy-structures over the telescope by the wind (which is often the case), the atmospheric coherence time can be approximated by the Fried parameter and the wind speed v as (Taylor, 1938)

$$\tau_0 = 0.31 \cdot r_0/v$$

Using typical values of $r_0 = 20\,\text{cm}$ and $v = 10\,\text{m/s}$ in I-band at the Calar Alto site (estimated from V-band values given in Ziad et al., 2005), gives $\tau_0 = 0.006\,\text{s}$. This corresponds to the exposure time at which the wavefront distortion changes are small.

1.3.2 Lucky short exposures

The idea of Lucky Imaging is to take a huge number of short exposures with integration times close to the atmospheric coherence time, so that the single frames have clear speckle patterns which are not smeared out. Only the least distorted frames are then shifted-and-added to reconstruct the final image. A typical Lucky Imaging time series of a binary star can be seen in Figure 1.4. It clearly shows that the speckle pattern of neighbouring frames correlates well and that the image quality varies significantly within the frames. Quantitatively, the image quality can be measured by the Strehl ratio (SR), that is the ratio of the observed peak count and the peak count that a perfectly diffraction limited PSF would have. The Strehl ratio depends on the wavefront variance σ^2 with approximately $\text{SR} = \exp(-\sigma^2)$ (Ross, 2009). As the telescope diameter in the optical and near infrared is usually several times bigger than the coherence length r_0, only a few images will have a $\sigma^2 < 1\,\text{rad}^2$ and hence a $\text{SR} > 0.37$. Their number can be calculated by

$$P \approx 5.6 \cdot \exp[-0.1557 \cdot (D/r_0)^2]$$

for $D/r_0 > 3.5$ as has been shown by Fried (1978) in drawing random wavefront distortion distributions for a specific r_0. For the Calar Alto 2.2 m telescope under excellent conditions, $r_0 = 40\,\text{cm}$, the probability to obtain short exposures with a Strehl ratio of 0.37 or more is then 0.05, e.g. 1000 out of 20 000 frames, a typical number of frames. Though these conditions are seldom reached, the Strehl ratio of most frames in the I-band is still significantly higher than in the seeing limited case. The resulting Lucky

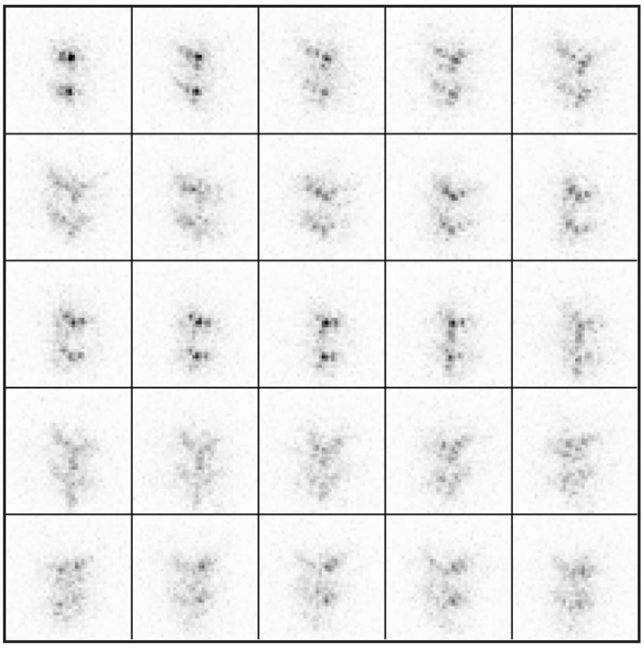

Figure 1.4: Consecutive frames of the double star WDS 14139+2906 with 30 ms exposure time, observed at the 2.2 m telescope in Calar Alto at an effective wavelength of 980 nm. The field of view is 1.9″x1.9″ with East up and North to the right (Figure taken from Hormuth (2007)).

Image usually has a Strehl ratio of about 0.1, which is a factor of 10 higher than in the seeing limited case (Hormuth, 2007). The amelioration of the image resolution by frame selection is shown in Figure 1.5. Note that there is an optimal wavelength range for the use of Lucky Imaging which depends on the turbulence and the telescope diameter. As $r_0 \propto \lambda^{6/5}$, the probability of getting an image with high Strehl ratio gets much smaller at shorter wavelengths, e.g. it is negligible in the V-band for the same telescope configuration and seeing. On the other hand, if longer wavelength ranges are used, e.g. the observations take place in the K-band, the probability of getting a frame with a SR > 0.37 is higher, but the telescope resolution is worse, e.g. 0.25″ for a 2.2 m telescope. See Hormuth (2007); Hormuth et al. (2008) for more details on Lucky Imaging.

1.4 Target sample

Initially, the goal of this project was to study those transiting exoplanets for which the spin-orbit angle was measured by the Rossiter-McLaughlin effect. This are mainly hot Jupiters because for them the Rossiter-McLaughlin effect is more easily detected. Approximately 1/3 of them have orbits that are misaligned with respect to the stellar

Figure 1.5: The Lucky Imaging frame selection enhances the image resolution considerably. Here 50 000 frames with 25 ms each were taken in SDSS z'-band at the NTT. From left to right: a) Sum of all 50 000 frames, b) Sum of all 50 000 frames with the centre of gravity shifted to the same reference position, c) Same with best 50% of images chosen by Strehl ratio, d) Same with best 10%, e) Same with best 1% (Figure taken from Hippler et al. (2009)).

spin axis and the origin of the misalignment is poorly understood (see Section 1.1.3). As stellar companions can cause misalignment, we wanted to investigate if there is a correlation between spin-orbit misalignment and the presence or absence of a binary companion. The spin-orbit angle distribution of the targets that we observed is shown in Fig. 1.6. Since the knowledge about close stellar sources is also crucial for the determination of accurate planetary properties, we later relaxed the criterion and included all sources that were bright enough for successful Lucky Imaging and which preferentially lacked Lucky Imaging or other high-angular resolution observations. Most of the targets observed were announced by the SuperWASP and HATNet project. In addition, we followed up some of the known companion candidates in order to see whether they share common proper motion with the transiting exoplanet host star. The observations of the transiting exoplanet host stars were done at Calar Alto. The distance distribution and spectral type of the targets can be found in Fig. 1.6. The selection criteria were as follows:

- $-15^\circ < \delta < 90^\circ$: stars that are visible from Calar Alto
- $i \leq 13$ mag: stars that are bright enough for the Lucky Imaging technique
- Exoplanet systems that are well studied, e.g. no exoplanet candidate systems
- We observed only very few Kepler targets as a lot of them were observed by different Lucky Imaging and AO based surveys (Lillo-Box et al., 2012; Lillo-Box et al., 2014; Adams et al., 2012, 2013; Dressing et al., 2014; Wang et al., 2014; Law et al., 2014; Gilliland et al., 2015; Horch et al., 2014)

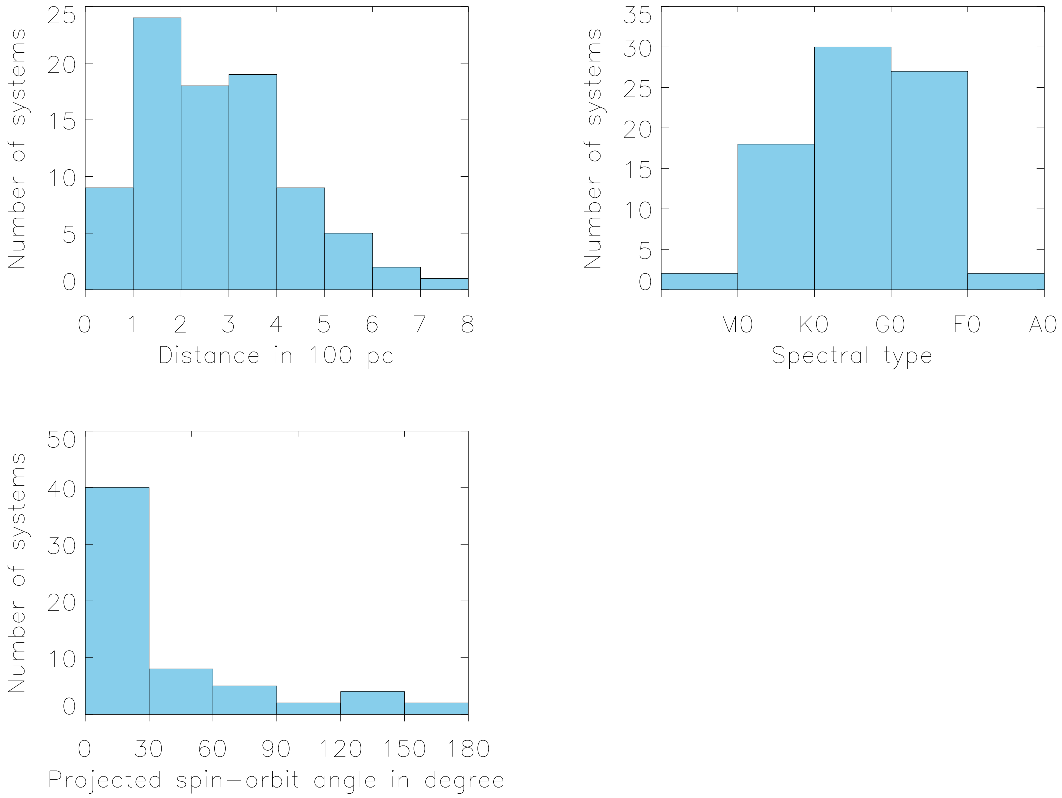

Figure 1.6: Top: Distance and spectral type of the 109 observed transiting exoplanet host stars. Bottom: The distribution of the spin-orbit angle for the 62 systems for which the Rossiter-McLaughlin effect has been measured.

2

A Lucky Imaging search for stellar companions to transiting planet host stars

During our first Lucky Imaging survey in June 2013, we observed 49 transiting exoplanet systems at the 2.2 m telescope at Calar Alto. We detect previously unknown companion candidates to WASP-14 and WASP-58. We find that they increase the planet-to-star radius ratio given in the discovery papers by 0.3% and 0.5%, respectively. The source near WASP-14 is by now a confirmed common proper motion companion (Ngo et al., 2015). Our results are published in A&A and the paper can be found on the following pages.

A&A 575, A23 (2015)
DOI: 10.1051/0004-6361/201424091
© ESO 2015

Astronomy & Astrophysics

A Lucky Imaging search for stellar companions to transiting planet host stars[★]

Maria Wöllert[1], Wolfgang Brandner[1], Carolina Bergfors[2], and Thomas Henning[1]

[1] Max-Planck-Institut für Astronomie, Königstuhl 17, 69117 Heidelberg, Germany
e-mail: `woellert@mpia.de`
[2] Department of Physics and Astronomy, University College London, Gower Street, London WC1E 6BT, UK

Received 29 April 2014 / Accepted 19 December 2014

ABSTRACT

The presence of stellar companions around planet hosting stars influences the architecture of their planetary systems. To find and characterise these companions and determine their orbits is thus an important consideration to understand planet formation and evolution. For transiting systems even unbound field stars are of interest if they are within the photometric aperture of the light curve measurement. Then they contribute a constant flux offset to the transit light curve and bias the derivation of the stellar and planetary parameters if their existence is unknown. Close stellar sources are, however, easily overlooked by common planet surveys due to their limited spatial resolution. We therefore performed high angular resolution imaging of 49 transiting exoplanet hosts to identify unresolved binaries, characterize their spectral type, and determine their separation. The observations were carried out with the Calar Alto 2.2 m telescope using the Lucky Imaging camera AstraLux Norte. All targets were imaged in i' and z' passbands. We found new companion candidates to WASP-14 and WASP-58, and we re-observed the stellar companion candidates to CoRoT-2, CoRoT-3, CoRoT-11, HAT-P-7, HAT-P-8, HAT-P-41, KIC 10905746, TrES-2, TrES-4, and WASP-2. We deduce from the stellar density around all sources that *two* companion candidates out of the targets with the first position measurement (CoRoT-11, HAT-P-41, KIC 10905746, WASP-14 and WASP-58) are probably unbound. In addition, we re-analyse the influence of the sources close to WASP-14 and WASP-58 on the planetary parameters given in the literature and find no significant changes.

Key words. techniques: high angular resolution – binaries: visual – planetary systems

1. Introduction

Since the first detection of a transiting planet around a main-sequence star in 2000 (Henry et al. 2000), many hundreds of giant planets have been found by transit surveys. Interestingly, a vast number of these planets are located close to their host star with semi-major axes smaller than 0.5 AU. In addition, many of them are not in circular, well aligned orbits, but show a variety of eccentricities and orbit inclinations. In fact, about 30% of the investigated systems have been found to be on orbits that are misaligned with respect to the stellar equator (see Southworth 2011, for a list of investigated systems).

Giant planets are, however, believed to form beyond the ice line in a well-aligned circumstellar disk at several AU from their host star. This means that they have to move inwards at a later stage. Several mechanisms have been discussed to explain the findings. First of all, migration, which is the interaction of the embedded planet with the surrounding disk (see Baruteau et al. 2013, for a review), can cause inward-spiraling of the planet. Yet, disk-planet interaction in a planetary system with only one massive planet tends to damp the planet's eccentricity and inclination and cannot account for eccentric or inclined close-in orbits. Planet-planet interaction in multiple planetary systems can, however, excite the eccentricities and inclinations of the planetary orbits as has been shown in numerical simulations (e.g. Ford & Rasio 2008). Similar but stronger effects are caused by a companion star that may interact with the planets around the primary via the Lidov-Kozai mechanism (Naoz et al. 2011). It has been shown in simulations that both tight and wide binary companions can strongly perturb the formation and evolution of planetary systems (Bouwman et al. 2006; Fabrycky & Tremaine 2007; Malmberg et al. 2011; Petrovich 2015). In addition, the tidal field of the Milky Way induces a pseudo-random walk of the pericenters of wide binaries leading to strong perturbations of the planets in the system (Kaib et al. 2013). It is thus crucial to look for close and wide stellar companions and correlate their properties with those of the close-in giant planets to understand the influence of binarity on the evolution of planetary systems. A fair number of transiting exoplanet host stars (TEPs) have already been subject to high angular resolution studies (e.g. Daemgen et al. 2009; Lillo-Box et al. 2012; Adams et al. 2012; Bergfors et al. 2013; Faedi et al. 2013; Ginski et al. 2013; Law et al. 2013) and a couple of gravitationally bound companions has been found. The increasing number of transiting exoplanet detections enables, however, a more thorough analysis of planetary systems in binaries.

Another important aspect of the search for stellar companions is the dilution of the light curve by a blended companion, no matter if it is bound or not. An unresolved faint secondary star within the photometric aperture dilutes the measured transit or occultation depth by the fraction $F_{\text{bright}}/F_{\text{total}}$. For example, Crossfield et al. (2012) showed that an M dwarf near WASP-12 diluted the planet's infrared emission spectrum by up to 15%, an effect substantially larger than the previously quoted uncertainty on the planet's emission. Daemgen et al. (2009), Narita et al. (2010), Bergfors et al. (2013) have reported optical imaging of stars located near several transit systems whose hot Jupiters have well-characterized spectra: HAT-P-7, TrES-2, TrES-4, WASP-2, and WASP-12.

In this paper, we present the results of our photometric and astrometric Lucky Imaging study of another 49 TEPs, which complements the study of Daemgen et al. (2009) and Bergfors et al. (2013). Besides the derivation of i and z magnitudes, photometric spectral types, and the relative position of the companion candidates, we discuss the probability of physical

---

[★] Table 1 is available in electronic form at `http://www.aanda.org`

Table 2. Candidate binary systems and their properties.

Name	Sep [″]	PA [°]	$\Delta i'$ [mag]	$\Delta z'$ [mag]	Date of obs.
CoRoT-2	4.090 ± 0.005	208.6 ± 0.2	3.38 ± 0.05	3.00 ± 0.05	26 Jun. 2013
CoRoT-3-south	5.209 ± 0.006	174.7 ± 0.2	3.24 ± 0.06	3.10 ± 0.06	26 Jun. 2013
CoRoT-3-east	4.995 ± 0.156	92.2 ± 1.6	5.53 ± 0.13	5.38 ± 0.17	26 Jun. 2013
CoRoT-11	2.545 ± 0.006	307.2 ± 0.2	2.34 ± 0.05	2.68 ± 0.06	26 Jun. 2013
HAT-P-7	3.843 ± 0.034	89.8 ± 0.4	7.58 ± 0.17	6.88 ± 0.20	26 Jun. 2013
HAT-P-8	1.034 ± 0.067	139.2 ± 1.2	7.34 ± 0.10[1]	6.68 ± 0.07[1]	27 Jun. 2013
HAT-P-41	3.619 ± 0.005	184.1 ± 0.2	3.65 ± 0.05	3.40 ± 0.05	26 Jun. 2013
KIC 10905746	4.075 ± 0.006	98.7 ± 0.2	2.42 ± 0.1	2.31 ± 0.1	28 Jun. 2013
TrES-2	1.106 ± 0.005	136.3 ± 0.2	3.83 ± 0.04	3.37 ± 0.05	25 Jun. 2013
TrES-4	1.596 ± 0.017	0.0 ± 0.6	4.49 ± 0.08	4.16 ± 0.09	25 Jun. 2013
WASP-2	0.711 ± 0.019	105.1 ± 0.5	3.51 ± 0.04	3.26 ± 0.06	25 Jun. 2013
WASP-14	1.423 ± 0.034	102.2 ± 1.0	5.35 ± 0.11	5.45 ± 0.16	26 Jun. 2013
WASP-58	1.275 ± 0.015	183.2 ± 0.4	5.64 ± 0.18	5.09 ± 0.13	25 Jun. 2013

References. (1) Bergfors et al. (2013).

companionship of the observed sources and the effect of the flux contribution a companion candidate has on stellar and planetary parameters.

2. Observations and data reduction

2.1. Lucky Imaging with AstraLux

The 49 TEPs were observed at the 2.2 m telescope at Calar Alto in June 24–28, 2013. We imaged each target with the Lucky Imaging camera AstraLux Norte (Hormuth et al. 2008) in SDSS i' and z'-passband. Lucky Imaging enables nearly diffraction-limited observations by taking a series of many short exposures of the target and combining only the least distorted frames to the final image. Depending on the target brightness, we obtained between 20 000 and 60 000 individual frames with exposure times of 15 ms each. The 10% of images with the highest Strehl ratio were then shifted and added to produce the final image. The field of view of the final image was about 12″ × 12″ with the transiting exoplanet system at the centre. As indicated by the *1st epoch* flag in Table 1, we observed 42 of the 49 stars with Lucky Imaging for the first time.

Astrometric reference stars in the globular cluster M 13 were observed at the beginning and the middle of each night to calibrate the detector rotation and pixel scale. The plate scale and detector rotation was deduced from the measured detector position of five stars of M 13 with the image reduction and analysis facility IRAF using the task imexamine. We calculated the separation and rotation angle of the five stars pairwise and compared these values to data from high-quality astrometric HST/ACS observations. This analysis yielded a plate scale of 23.48 ± 0.01 mas/px and a detector rotation of 1.7° ± 0.1° west of north. Additionally, twilight sky-flats and bias were obtained in both filters at the beginning of each observing night.

2.2. Photometry and astrometry

In our sample of 49 TEPs we found 13 companion candidates by visual inspection of the reduced Lucky Imaging frames; they are listed in Table 2 and the z'-band frames are depicted in Fig. 1. Eleven of them were previously known: CoRoT-2 (Alonso et al. 2008), CoRoT-3 (Deleuil et al. 2008), CoRoT-11 (Gandolfi et al. 2010), HAT-P-7 (Narita et al. 2010), HAT-P-8 (Bergfors et al. 2013), HAT-P-41 (Hartman et al. 2012), KIC 10905746 (Fischer et al. 2012), TrES-2 (Daemgen et al. 2009), TrES-4 (Daemgen et al. 2009), and WASP-2 (Collier Cameron et al. 2007). The candidate companions to WASP-14 and WASP-58 have not been reported in the literature so far.

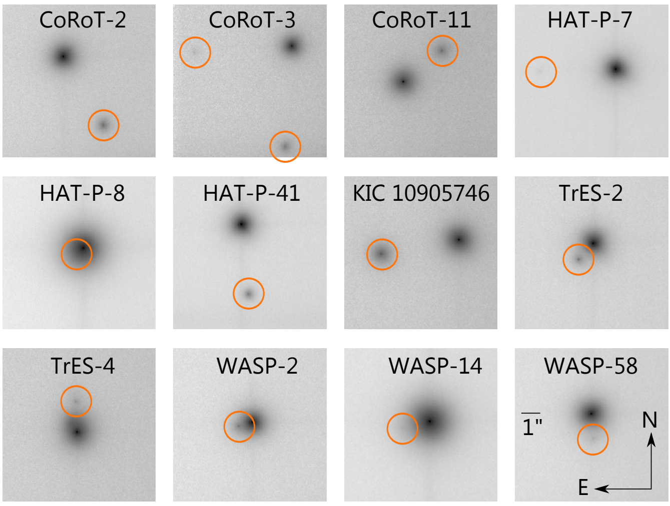

Fig. 1. z' filter images of the 12 exoplanet host stars for which companion candidates have been detected. The image scale is logarithmic. The size and orientation is identical for all images and indicated in the *lower right image*.

We obtained the positions of the two stellar components by fitting a model psf to the data. The theoretical psf is built from the ideal point spread function without atmospheric turbulences and telescope aberrations, which is then convolved with a Gaussian blurring function. Finally, a Moffat profile is added to the blurred theoretical profile (see Wöllert et al. 2014, for more information on the procedure). The separation and position angle given in Table 2 is the average value from our i' and z' measurements; the uncertainties are determined to take the position uncertainty in every single image into account, as well as the uncertainties in pixel scale and instrument rotation. For the very faint companions to HAT-P-8 and WASP-14 the algorithm did not converge and we estimated the position by eye. The companion of HAT-P-8 is itself a binary (Ginski et al. 2013; Bechter et al. 2014), which causes an elongation of the psf and might be the reason for the non-convergence.

We used the psf-subtracted images to calculate the 5σ-contrast curve for every target with or without companions; a list of all observed targets and their sensitivity limits at $r = 0.25''$, $0.5''$, $1.0''$, and $2.0''$ can be found in Table 1, the average z'-passband sensitivity can be found in Fig. 2. The noise of each pixel was estimated using the standard deviation of the residual signal in a box of 5 × 5 pixel around it. This value was then compared to the flux of the star in a 5 × 5 pixel box centred

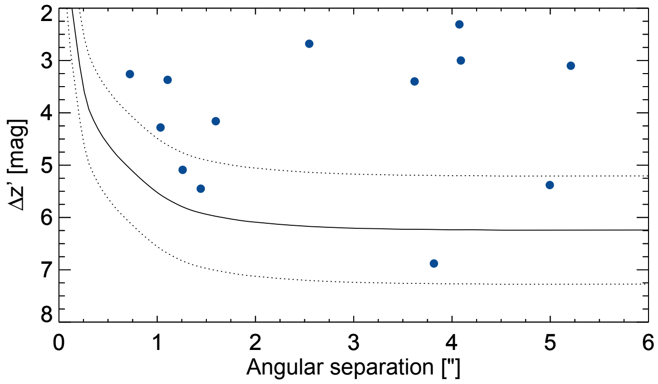

Fig. 2. Average sensitivity of the survey (solid line). The dashed lines corresponds to 1σ deviations of the contrast curves. The blue circles indicate the detections.

on the peak. The contrast at a specific angular separation range was calculated as the median of the contrast of all pixels in the corresponding distance.

The brightness difference of the components in the i' and z' passbands was determined by aperture photometry using the IDL routine APER. We chose an aperture radius of 4.5 pixel centred on the stars to ensure that most of the flux is covered. The sky background was measured in an annulus from 6 pixel to 8 pixel. The error bars in magnitude differences are propagated from the photometric errors estimated with APER.

3. Companion properties

3.1. Spectral types

The spectral types of the companion candidates are derived from the observed magnitude differences in SDSS i' and z'-band between the host and the companion, and by assuming negligible foreground extinction. The latter is justified as the TEP are located off the Galactic plane and not in the direction of any nearby molecular cloud. The i' and z' magnitudes of the host stars in turn are estimated from the spectral types given in the literature or, if not known, from 2MASS *JHK*-photometry (Cutri et al. 2003) (HAT-P-41) or from the $V - J$ colour (KIC-10905746). To convert the spectral type to i' and z' brightness, we use the *ugriz* stellar spectral energy distribution models for main-sequence stars from Kraus & Hillenbrand (2007). We assume an uncertainty of 0.10 mag in both filters to consider the flux uncertainty in i' and z' due to our estimate. We neglect the small magnitude differences, which arise from the conversion from i, z to i', z'; they are of the order 0.01 mag in both filters for the spectral types of our host stars. Knowing the primaries i' and z' colours we calculate the i' and z' magnitude of the companion candidate. For the companion candidates we do not neglect the differences in the photometric system because of their redder colour and we use the conversion formulas on the SDSS webpage to get i and z magnitudes. Since the r' magnitude is needed to convert i' to i, we use a rough estimate of r' based on the measured $i' - z'$ colour. This is sufficient since the two photometric systems only deviate strongly for very late sources that we did not detect.

Assuming a physical association between TEP and companion candidate, we compute absolute i and z magnitudes of the secondary. With the exception of the binary companion candidate to CoRoT-3-east, the absolute magnitudes and the spectral types based on the $i - z$ colour are consistent within the uncertainties (Table 3). Our spectral type estimates also agree with the values in the literature that are given for some of the targets. The spectral types of the other companion candidates to HAT-P-41, KIC-10905746, and WASP-58 are most likely late-type as expected for a fainter associated companion; for CoRoT-11 and WASP-14 the photometric spectral typing points at early-type stars not at the same distance as the TEP. This makes physical companionship unlikely, but further measurements are needed to give a final answer.

3.2. Probability of chance alignment

For the newly discovered companion candidates, we only measured one epoch and can make no clear statement on whether these stars are physically bound or unbound objects. We can, however, make a statistical argument on how many candidates of our whole sample are likely to be unrelated field stars. First, we estimate the density of field stars ρ_i around each target by selecting all stars brighter than $m_K = 14$ mag within 30′ of the target in the 2MASS PSC (Cutri et al. 2003). These criteria ensure that the stars are visible with AstraLux and are a good approximation of the mean stellar density around the source. We then assume that the stars are Poisson distributed and we calculate the probability of detecting one or more field stars $\overline{P_i(0)}$ (i.e. the complement of finding zero stars) with the maximum angular separation Θ:

$$\overline{P_i(0)} = 1 - \exp(-\pi\Theta^2 \cdot \rho_i). \tag{1}$$

The probability of finding one or more field stars within our FoV of 6″ ranges between 0.9% and 38%; for the observed companion candidates with first epoch measurements, we find 38% for CoRoT-11, 14% for HAT-P-41, 4.4% for KIC 10905746, 0.9% for WASP-14, and 3.2% for WASP-38. The average probability of finding a field star is 4.7%. For the whole survey of 42 stars with first relative position measurement our expectation is thus two unrelated field stars. This means that out of our five objects one or two are likely not bound. Good candidates are CoRoT-11 and WASP-14 because of their early spectral type. In addition, the stellar density around CoRoT-11 is rather high. The seven follow-up targets with previous AstraLux epochs and previously known companion candidates (see Table 1) were excluded from this analysis to avoid introducing any bias.

3.3. System parameter changes of WASP-14 and WASP-58

The newly discovered companion candidates will, if they are within the photometric aperture, contribute a constant flux offset that affects the stellar and planetary parameters derived from the depth and shape of the transit light curve: R_p/R_*, b, a/R_* and ρ_*. The additional flux contribution from a stellar companion has the greatest effect on the planet-to-star radius; assuming no limb darkening and flat-bottomed transits, this parameter is directly proportional to the depth of the transit (see Seager & Mallén-Ornelas 2003),

$$\Delta F = (F_{\text{no transit}} - F_{\text{transit}})/F_{\text{no transit}} = (R_\text{p}/R_*)^2. \tag{2}$$

We account for the secondary star flux using the relation between ΔF_old, assuming only the flux from the brighter planet host, and ΔF_new, including the companion flux (see Daemgen et al. 2009),

$$\Delta F_\text{new} = (1 + 10^{-\Delta z/2.5}) * \Delta F_\text{old}, \tag{3}$$

where Δz is our measured magnitude difference between the planet host star and the companion candidate in z-band (see Table 2). We calculate new planet-to-star ratios for the WASP-14 and WASP-58 systems using ΔF from the planet discovery papers by Joshi et al. (WASP-14b; 2009) and Hébrard et al. (WASP-58b; 2013). The new companions are both >5 mag

Table 3. Spectral type estimates of the candidate companions from $(i - z)$ colour.

Name	SpT(A)	$M_i(A)$	$M_z(A)$	$M_i(B)^*$	$M_z(B)^*$	$M_i(B) - M_z(B)$	SpT(B)	Lit.
CoRoT-2	G7V	4.89 ± 0.10	5.08 ± 0.10	8.28 ± 0.11	8.08 ± 0.11	0.20 ± 0.16	G4-M0	M0[1]
CoRoT-3-south	F3V	3.27 ± 0.10	3.33 ± 0.10	6.50 ± 0.16	6.44 ± 0.20	0.07 ± 0.26	A2-K7	K4-K5[1]
CoRoT-3-east	F3V	3.26 ± 0.10	3.33 ± 0.10	8.78 ± 0.12	8.72 ± 0.12	0.07 ± 0.16	F1-K5	
CoRoT-11	F6V	3.88 ± 0.10	3.92 ± 0.10	6.19 ± 0.11	6.62 ± 0.12	-0.43 ± 0.16	early	
HAT-P-7	F6V	3.88 ± 0.10	3.92 ± 0.10	11.53 ± 0.11	10.79 ± 0.11	0.74 ± 0.16	M2-M5	M5.5[2]
HAT-P-8	F5V	4.14 ± 0.10	4.50 ± 0.10	11.48 ± 0.14	11.18 ± 0.12	0.30 ± 0.18[3]	–	M1-M3.5[3,4]
HAT-P-41	F9	4.35 ± 0.10	4.36 ± 0.10	8.00 ± 0.20	7.76 ± 0.22	0.25 ± 0.30	F5-M2	
KIC 10905746	K7	6.90 ± 0.10	6.58 ± 0.10	9.34 ± 0.14	8.88 ± 0.14	0.46 ± 0.20	K5-M3	
TrES-2	G0V	4.44 ± 0.10	4.44 ± 0.10	8.30 ± 0.11	7.80 ± 0.11	0.50 ± 0.16	K7-M3	M1-M2[1] , K0-M0[3]
TrES-4	F8	4.26 ± 0.10	4.28 ± 0.10	8.76 ± 0.13	8.44 ± 0.13	0.32 ± 0.19	K2-M2	M2[1] , K4.5-M1.5[3]
WASP-2	K1.5	5.84 ± 0.10	5.71 ± 0.10	9.36 ± 0.15	8.97 ± 0.19	0.40 ± 0.24	K2-M3	M1V-M4V[3]
WASP-14	F5V	3.69 ± 0.10	3.74 ± 0.10	9.03 ± 0.11	9.20 ± 0.12	-0.17 ± 0.16	early	
WASP-58	G2V	4.54 ± 0.10	4.51 ± 0.10	10.20 ± 0.21	9.59 ± 0.16	0.62 ± 0.26	K7-M5	

Notes. (*) Assuming physical companionship.

References. (1) Faedi et al. (2013); (2) Narita et al. (2012); (3) Bergfors et al. (2013); (4) Bechter et al. (2014).

fainter than the planet host stars and therefore contribute comparatively little flux. For the WASP-14 system we find that, after accounting for the previously unknown companion candidate, the planet-to-star ratio R_*/R_p increases by 0.3%, which is well within the ≈1.4% errors derived by Joshi et al. (2009). Similarly, the companion candidate to WASP-58 only adds 0.5% to the same parameter, therefore not affecting the results by Hébrard et al. (2013).

4. Discussion and summary

A stellar companion to an exoplanet hosting system is expected to affect planet formation and the subsequent dynamical evolution in several ways. Our observations of transiting planet host stars are part of an ongoing effort to find and characterise binary companions using the Lucky Imaging technique. During this run we took high-resolution images of 49 exoplanet host stars, which revealed two previously unknown stellar companion candidates to the sources WASP-14 and WASP-58. Close, undetected sources, whether bound or not, influence the derivation of stellar and planetary properties of the host system. For WASP-14 and WASP-58 we show, however, that their presence only has a minor impact because of their faintness. Apart from these two sources we also measured the astrometric position of CoRoT-11, HAT-P-41, and KIC 10905746 for the first time. We deduce from the mean stellar density around our targets that three out of those five candidate companions are likely to be gravitationally bound. This is also supported by the fact that HAT-P-41, KIC-10905746, and WASP-58 have a spectral type of late K or early M as expected for a fainter associated companion. By contrast, CoRoT-11 is situated in a dense stellar region and the detected source at 2.5″ most likely has an early spectral type; it is thus unlikely to be bound.

In addition, we did follow-up observations of CoRoT-2, CoRoT-3, HAT-P-7, HAT-P-8, TrES-2, TrES-4, and WASP-2. Our spectral type estimations for these sources agree with earlier observations. The new positional data for CoRoT-2, CoRoT-3, and TrES-2 is not sufficient to decide on common proper motion, which is already known for HAT-P-7 (Narita et al. 2012), HAT-P-8 (Ginski et al. 2013; Bechter et al. 2014), TrES-4 (Bergfors et al. 2013), and WASP-2 (Bergfors et al. 2013).

The knowledge of gravitationally bound companions can be used to correlate binarity and exoplanet properties in future. This analysis is, however, hampered by the fact that no orbital motion of the stellar companions is visible so far. Thus, for now the true stellar separation and the relative orientation of the planetary and the stellar orbit remain unknown.

References

Adams, E. R., Ciardi, D. R., Dupree, A. K., et al. 2012, AJ, 144, 42
Adams, E. R., Dupree, A. K., Kulesa, C., & McCarthy, D. 2013, AJ, 146, 9
Alonso, R., Auvergne, M., Baglin, A., et al. 2008, A&A, 482, L21
Baruteau, C., Crida, A., Paardekooper, S.-J., et al. 2013, in Protostars and Planets VI (University of Arizona Press), eds. H. Beuther, R. Klessen, C. Dullemond, & Th. Henning [arXiv:1312.4293]
Bechter, E. B., Crepp, J. R., Ngo, H., et al. 2014, ApJ, 788, 2
Bergfors, C., Brandner, W., Daemgen, S., et al. 2013, MNRAS, 428, 182
Bouwman, J., Lawson, W. A., Dominik, C., et al. 2006, ApJ, 653, L57
Collier Cameron, A., Bouchy, F., Hébrard, G., et al. 2007, MNRAS, 375, 951
Crossfield, I. J. M., Barman, T., Hansen, B. M. S., Tanaka, I., & Kodama, T. 2012, ApJ, 760, 140
Cutri, R. M., Skrutskie, M. F., van Dyk, S., et al. 2003, VizieR Online Data Catalog: II/246
Daemgen, S., Hormuth, F., Brandner, W., et al. 2009, A&A, 498, 567
Deleuil, M., Deeg, H. J., Alonso, R., et al. 2008, A&A, 491, 889
Fabrycky, D., & Tremaine, S. 2007, ApJ, 669, 1298
Faedi, F., Staley, T., Gómez Maqueo Chew, Y., et al. 2013, MNRAS, 433, 2097
Fischer, D. A., Schwamb, M. E., Schawinski, K., et al. 2012, MNRAS, 419, 2900
Ford, E. B., & Rasio, F. A. 2008, ApJ, 686, 621
Gandolfi, D., Hébrard, G., Alonso, R., et al. 2010, A&A, 524, A55
Ginski, C., Mugrauer, M., Seeliger, M., & Löhne, T. 2013, A&A, 559, A71
Hartman, J. D., Bakos, G. Á., Béky, B., et al. 2012, AJ, 144, 139
Hébrard, G., Collier Cameron, A., Brown, D. J. A., et al. 2013, A&A, 549, A134
Henry, G. W., Marcy, G. W., Butler, R. P., & Vogt, S. S. 2000, ApJ, 529, L41
Hormuth, F., Brandner, W., Hippler, S., & Henning, T. 2008, J. Phys. Conf. Ser., 131, 012051
Joshi, Y. C., Pollacco, D., Collier Cameron, A., et al. 2009, MNRAS, 392, 1532
Kaib, N. A., Raymond, S. N., & Duncan, M. 2013, Nature, 493, 381
Kraus, A. L., & Hillenbrand, L. A. 2007, AJ, 134, 2340
Law, N. M., Morton, T., Baranec, C., et al. 2013, Am. Astron. Soc. Meet. Abstr., 221, 334.06
Lillo-Box, J., Barrado, D., & Bouy, H. 2012, A&A, 546, A10
Malmberg, D., Davies, M. B., & Heggie, D. C. 2011, MNRAS, 411, 859
Naoz, S., Farr, W. M., Lithwick, Y., Rasio, F. A., & Teyssandier, J. 2011, Nature, 473, 187
Narita, N., Kudo, T., Bergfors, C., et al. 2010, PASJ, 62, 779
Narita, N., Takahashi, Y. H., Kuzuhara, M., et al. 2012, PASJ, 64, L7
Petrovich, C. 2015, ApJ, 799, 27
Seager, S., & Mallén-Ornelas, G. 2003, ApJ, 585, 1038
Southworth, J. 2011, MNRAS, 417, 2166
Wöllert, M., Brandner, W., Reffert, S., et al. 2014, A&A, 564, A10

Page 5 is available in the electronic edition of the journal at `http://www.aanda.org`

Table 1. All transiting exoplanet systems investigated, radial detection limits, and y/n flag indicating only if 1st epoch observations are available.

	5σ detection limit ($\Delta z'$ [mag])				1st
Name	0.25″	0.5″	1.0″	2.0″	epoch
Targets without candidate companions					
HAT-P-3	3.84	4.62	5.55	6.20	y
HAT-P-4	3.97	4.74	5.56	6.19	y
HAT-P-12	3.69	4.45	5.22	5.65	y
HAT-P-14	3.99	5.04	6.47	7.32	y
HAT-P-16	4.05	4.88	5.87	6.63	y
HAT-P-17	3.84	4.95	6.29	7.09	y
HAT-P-18	3.64	4.43	5.24	5.56	y
HAT-P-21	3.75	4.35	5.18	5.72	y
HAT-P-22	3.95	4.97	6.12	7.19	y
HAT-P-23	3.50	4.19	5.06	5.43	y
HAT-P-26	3.64	4.59	5.62	6.15	y
HAT-P-27	3.73	4.35	5.20	5.63	y
HAT-P-31	3.98	4.75	5.68	6.16	y
HAT-P-32	3.17	3.91	4.31	4.48	y
HAT-P-34	4.05	5.40	6.80	7.38	y
HAT-P-36	3.63	4.53	5.27	5.64	y
HAT-P-40	3.72	4.45	5.21	5.89	y
HD 97658	3.43	5.03	6.06	7.36	y
Kepler-8	3.19	3.88	4.35	4.49	y
Kepler-17	3.29	3.49	4.29	4.40	y
Kepler-25	4.22	5.30	6.55	7.11	y
Kepler-50	3.95	5.49	6.70	7.23	y
Qatar-1	3.65	4.43	5.27	5.55	y
WASP-10	3.62	4.29	5.04	5.49	y
WASP-21	3.67	4.52	5.34	5.90	y
WASP-24	3.86	4.65	5.56	6.06	y
WASP-28	3.20	3.77	4.43	4.96	y
WASP-37	3.13	3.65	4.20	4.69	y
WASP-38	3.83	5.27	6.96	7.90	y
WASP-39	3.42	4.27	5.08	5.55	y
WASP-47	3.71	4.46	5.36	5.71	y
WASP-48	3.94	5.02	5.84	6.09	y
WASP-52	3.91	4.54	5.39	5.85	y
WASP-59	3.62	4.34	5.27	5.68	y
WASP-60	3.47	4.20	5.04	5.42	y
WASP-80	4.01	5.03	6.11	6.64	y
XO-1	3.97	4.85	5.79	6.46	y
Targets with candidate companions					
CoRoT-2	4.10	4.83	5.73	5.99	n
CoRoT-3	3.69	4.41	5.29	5.81	n
CoRoT-11	3.29	4.17	4.82	5.01	y
HAT-P-7	4.03	5.51	6.86	7.41	n
HAT-P-8	4.24	5.13	6.26	7.11	n
HAT-P-41	4.00	5.48	6.74	7.20	y
KIC-10905746	3.70	4.46	5.26	5.56	y
TrES-2	4.03	5.06	6.14	6.58	n
TrES-4	3.62	4.40	5.32	5.78	n
WASP-2	3.93	4.97	6.00	6.40	n
WASP-14	4.20	4.99	6.14	7.07	y
WASP-58	4.36	5.30	6.19	6.60	y

Notes. HAT-P-17 and HAT-P-32 have been observed as well by Adams et al. (2013) using adaptive optics at the MMT. In agreement with our results they do not see a companion candidate around HAT-P-17, but they find one around HAT-P-32 at 2.87″, PA = 109°, and $\Delta K = 3.4$ mag.

3

A Lucky Imaging search for stellar sources near 74 host stars

Further observations of transiting exoplanet host stars were done in October 2014 and March 2015 using the same setup as in the previous work. This time we found new companion candidates within 4″ around HAT-P-27, HAT-P-28, HAT-P-29, HAT-P-35, WASP-56, WASP-76, and WASP-103. The paper was published in A&A.

A&A 579, A129 (2015)
DOI: 10.1051/0004-6361/201526525

Astronomy & Astrophysics

A Lucky Imaging search for stellar sources near 74 transit hosts*

Maria Wöllert and Wolfgang Brandner

Max-Planck-Institut für Astronomie, Königstuhl 17, 69117 Heidelberg, Germany
e-mail: `woellert@mpia.de`

Received 13 May 2015 / Accepted 17 June 2015

ABSTRACT

Context. Many transiting-planet host stars lack high-resolution imaging so that close stellar sources can be missed. Those unknown stars potentially bias the derivation of the planetary and stellar parameters from the transit light curve, regardless of whether they are bound or not. In addition, bound stellar companions interact gravitationally with the exoplanet host star, the disk, and the planets and can thus influence the formation and evolution of the planetary system strongly.

Aims. We extended our high-resolution Lucky Imaging survey for close stellar sources by 74 transiting-planet host stars. Thirty-nine of these stars lack previous high-resolution imaging, 23 are follow up observations of companions or companion candidates, and the remaining stars have been observed by others with AO imaging but in different bands. We determine the separation of all new and known companion candidates and estimate the flux ratio in the observed bands.

Methods. All observations were carried out with the Lucky Imaging camera AstraLux Norte at the Calar Alto 2.2 m telescope in i' and z' passbands.

Results. We find new stellar sources within 1″ of HAT-P-27, HAT-P-28, HAT-P-35, WASP-76, and WASP-103 and between 1″ and 4″ of HAT-P-29 and WASP-56.

Key words. techniques: high angular resolution – binaries: visual – planetary systems

1. Introduction

During the past 15 years, more than 1000 confirmed and several 1000 candidate exoplanets have been found by ground- and space-based transit searches, such as HATNet (Bakos et al. 2004), SuperWasp (Pollacco et al. 2006), CoRoT (Baglin et al. 2006), and *Kepler* (Borucki et al. 2010; Batalha et al. 2013; Burke et al. 2014). Transiting exoplanets (TEPs) offer the unique opportunity to determine a variety of planetary properties, such as true mass, mean density, and surface gravity. They also allow the planet's atmosphere to be characterized through spectroscopy, the planet's temperature to be determined in secondary eclipse observations, and the angle to be measured between the orbital plane and the stellar rotation axis via the Rossiter-McLaughlin effect (Winn et al. 2005).

Since many follow-up observations of transiting planets were limited in angular resolution either by the instrument (e.g., *Spitzer*/IRAC) or – in the case of ground-based follow-up – seeing limitations, care has to be taken not to miss a blended close star. This is especially true for faint sources because bright stars may be recognized in follow-up spectra. Unknown, close stars add a constant flux to the light curve which bias both primary and secondary eclipse measurements. In the first case, the additional source leads to underestimating the planetary radius and consequently overestimating the planetary density. In the second case, the planet infrared emission spectrum can be underestimated by several tens of percentage points (e.g., Crossfield et al. 2012).

Finding stellar sources close to transiting exoplanet host stars is, however, not only crucial to determining the planetary parameters correctly, but also to understanding the influence of binarity on the formation and evolution of planetary systems. Even though not all of the detected close stars are gravitationally bound, a lot of them are, as has been shown via multi-epoch high-resolution observations (e.g., Narita et al. 2012, Bergfors et al. 2013, Ngo et al. 2015). The effects of binarity may be manifold: stellar companions might stir (Mayer et al. 2005), tilt (Batygin 2012) or truncate the protoplanetary disk (Artymowicz & Lubow 1994), or they can interact with the formed planets via, for example the Lidov-Kozai mechanism or other secular interactions (Wu & Murray 2003; Fabrycky & Tremaine 2007; Naoz et al. 2011). Stellar companions may thus be one important cause of the variety observed in planetary system architectures.

Several groups have already done systematic surveys of stellar companions using either the Lucky Imaging method (e.g., Daemgen et al. 2009; Faedi et al. 2013; Bergfors et al. 2013; Lillo-Box et al. 2012, 2014; Wöllert et al. 2015), speckle imaging (e.g. Howell et al. 2011; Horch et al. 2014; Kane et al. 2014; Everett et al. 2015), or AO-assisted imaging on its own or combined with radial velocity methods (e.g., Adams et al. 2012, 2013; Guenther et al. 2013; Dressing et al. 2014; Law et al. 2014; Wang et al. 2014; Ngo et al. 2015). Or they have searched for the colour-dependency of the transit depths (e.g., Colón et al. 2012; Désert et al. 2015). However, more and more transiting exoplanets have been found, and their precise characterization will enable us to get a more precise view of the important mechanisms that shape planetary systems.

In this paper we present the results of our ongoing effort to find stellar sources close to TEP host stars. The observations and data reductions were performed similarly to our previous paper Wöllert et al. (2015) and are briefly described in Sect. 2. In Sect. 3 we present the astrometric and photometric properties of the observed sources, and we summarize our findings in Sect. 4.

---

* Based on observations collected at the German-Spanish Astronomical Center, Calar Alto, jointly operated by the Max-Planck-Institut für Astronomie Heidelberg and the Instituto de Astrofísica de Andalucía (CSIC).

Table 1. TEP hosts with detection, radial contrast limits, and references to other high-resolution imaging papers if available.

Name	5σ detection limit ($\Delta z'$ [mag]) 0.25″	0.5″	1.0″	2.0″	Ref.
New companion candidates					
HAT-P-15	4.28	5.37	6.40	6.90	Ngo et al. (2015)*
HAT-P-27/WASP-40	3.90	4.82	5.75	6.20	Wöllert et al. (2015)*
HAT-P-28	3.24	3.94	4.76	5.12	
HAT-P-29	4.05	4.72	5.45	5.95	Ngo et al. (2015)*
HAT-P-35	2.81	3.37	3.94	4.11	
HAT-P-54	3.57	4.41	5.13	5.52	
Kepler-89	3.10	3.60	4.28	4.69	Adams et al. (2012)* , Lillo-Box et al. (2014)*
WASP-56	4.08	4.89	5.78	6.11	
WASP-76	3.81	4.79	6.21	7.18	
WASP-103	3.75	4.55	5.48	5.90	
Known companion candidates					
CoRoT-02	2.97	3.46	4.16	4.78	Alonso et al. (2008), Faedi et al. (2013), Wöllert et al. (2015)
CoRoT-03	2.85	3.22	3.65	3.97	Deleuil et al. (2008), Faedi et al. (2013), Wöllert et al. (2015)
CoRoT-11	3.25	3.85	4.65	4.97	Gandolfi et al. (2010), Wöllert et al. (2015)
HAT-P-20	3.64	4.30	5.22	5.97	Ngo et al. (2015)* , Bakos et al. (2011)†
HAT-P-24	3.51	4.39	5.11	5.67	Ngo et al. (2015)
HAT-P-30	4.01	5.06	6.09	6.72	Adams et al. (2013), Ngo et al. (2015)
HAT-P-32	3.78	4.61	5.35	5.84	Adams et al. (2013), Ngo et al. (2015), Wöllert et al. (2015)*
HAT-P-41	3.24	3.62	4.37	4.97	Hartman et al. (2012), Wöllert et al. (2015)
KELT-2	3.75	4.61	6.13	7.03	Beatty et al. (2012)†
KELT-3	3.95	4.75	5.45	5.95	Pepper et al. (2013)
Kepler-13	3.33	4.11	4.87	5.54	Santerne et al. (2012)
KIC10905746	3.33	3.78	4.56	5.09	Fischer et al. (2012)
LHS-6343	2.72	3.19	3.73	4.40	Johnson et al. (2011), Montet et al. (2015)
TrES-4	6.13	6.09	6.07	6.13	Daemgen et al. (2009), Bergfors et al. (2013), Faedi et al. (2013), Wöllert et al. (2015), Ngo et al. (2015)
WASP-11	3.80	4.81	5.70	6.25	Ngo et al. (2015)
WASP-12	4.03	4.78	5.56	6.12	Crossfield et al. (2012), Bergfors et al. (2013), Bechter et al. (2014)
WASP-14	4.26	5.29	6.82	7.70	Wöllert et al. (2015), Ngo et al. (2015)
WASP-33	3.33	4.77	6.64	7.90	Moya et al. (2011), Adams et al. (2013)
WASP-36	3.38	4.34	4.84	5.16	Smith et al. (2012)†
WASP-70	3.07	3.52	4.26	4.90	Anderson et al. (2014)†
WASP-77	3.71	4.54	5.60	6.42	Maxted et al. (2013)
WASP-85	4.25	5.26	6.21	7.12	Brown et al. (2014)†
XO-3	4.11	4.91	5.79	6.33	Bergfors et al. (2013), Adams et al. (2013)* , Ngo et al. (2015)*

Notes. $^{(*)}$ Outside FoV, $^{(\star)}$ no detection, $^{(\dagger)}$ seeing limited observation or catalog data.

2. Observations and data reduction

2.1. Sample selection

The initial goals of our survey were to focus on those TEPs with already existing measurements of the Rossiter-McLaughlin effect and to explore a possible relationship of the angle defined by the spin vectors of the TEP host star and the planetary orbit, and the presence or absence of a stellar companion. This selection criterion was later relaxed to include all TEP host stars bright enough ($i \leq 13$ mag) to facilitate high-quality Lucky Imaging. The majority of the targets were selected from TEPs that were identified either by the SuperWASP or the HatNet project. This was complemented by TEP hosts identified in other ground- or space-based surveys. We focused on stars without previous high-angular resolution observations, as well as on TEP host stars with previous detections of stellar companion candidates in order to derive constraints on the relative astrometry between TEP host and stellar companion candidate.

2.2. Lucky Imaging with AstraLux at Calar Alto

All observations were carried out at Calar Alto with the 2.2 m telescope in combination with the Lucky Imaging camera AstraLux Norte (Hormuth et al. 2008) during two observing runs, one night in October 2014 and three nights in March 2015. The targets were observed in SDSS i' and z'-passbands using the same set-up as described in Wöllert et al. (2015). The field of view was 12″ by 12″ with the exoplanet host star separated by at least 4″ from the image borders. Depending on the target brightness and observing conditions, we took between 10 000 and 54 000 individual frames with exposure times of 15 millisecond each so that the probability of getting a stable speckle pattern is sufficiently large. The individual AstraLux images are dark-subtracted and flat-fielded. For the data analysis we chose 10% of the images with the highest Strehl ratio and combined them using the shift-and-add technique.

To measure the separation and position angle of the companion candidates precisely, we took at least three images of the globular cluster M 13 each night. Using IRAF imexamine we determined the detector position of five widely separated stars in the field and calculated their separation and rotation angle pairwise. The result was compared to the values from high-quality astrometric HST/ACS observations. Because the instrument was not unmounted during the observing nights in March 2015, we used the images of all three nights for calibrating that run. The

Table 2. TEP hosts with no detection, radial contrast limits, and references to other high-resolution imaging papers if available.

Name	5σ detection limit ($\Delta z'$ [mag]) 0.25″	0.5″	1.0″	2.0″	Ref.
55 Cnc	2.90	2.70	3.04	3.85	Roell et al. (2012)
CoRoT-01	3.23	3.81	4.34	4.70	Adams et al. (2013)
CoRoT-07	3.81	4.47	5.26	5.80	Guenther et al. (2013)
CoRoT-24	2.78	3.26	3.44	3.51	Guenther et al. (2013)
EPIC-201367065	4.16	4.98	5.99	6.69	Crossfield et al. (2015)
EPIC-201505350	3.77	4.56	5.43	5.77	
GJ3470	4.01	4.97	5.61	5.96	
HAT-P-09	3.31	4.24	4.77	5.24	
HAT-P-25	3.80	4.72	5.57	5.80	Adams et al. (2013)
HAT-P-33	3.86	4.60	5.29	5.80	Adams et al. (2013), Ngo et al. (2015)
HAT-P-38	3.59	4.46	5.22	5.61	
HAT-P-39	3.28	4.23	4.87	5.32	
HAT-P-42	1.79	2.25	2.95	3.44	
HAT-P-43	3.33	4.18	4.82	5.12	
HAT-P-44	3.73	4.64	5.40	5.67	
HAT-P-45	3.43	4.12	4.75	5.11	
HAT-P-46	3.97	4.64	5.50	5.94	
HAT-P-49	2.83	3.38	3.98	4.64	
KELT-1	3.65	4.19	5.14	5.88	Siverd et al. (2012)
KELT-6	4.07	5.14	6.37	7.19	Collins et al. (2014)
KELT-7	3.80	5.45	6.78	7.70	Bieryla et al. (2015)
Kepler-63	3.59	4.36	5.36	5.73	Sanchis-Ojeda et al. (2013)
KOI-1474	2.79	3.33	3.79	4.16	
Qatar-2	3.59	4.32	5.12	5.47	
TrES-5	2.94	3.48	3.93	4.30	
WASP-30	3.28	3.72	4.63	5.11	
WASP-32	3.47	4.10	5.11	5.56	
WASP-35	3.72	4.42	5.37	5.98	
WASP-43	3.80	4.63	5.37	5.96	
WASP-44	2.85	3.37	4.08	4.47	
WASP-50	3.42	3.97	4.79	5.25	
WASP-54	4.04	5.02	6.22	6.93	
WASP-57	3.56	4.63	5.29	5.46	
WASP-65	3.89	4.73	5.63	6.09	
WASP-69	3.62	4.39	5.13	5.65	
WASP-71	3.59	4.17	5.22	5.94	
WASP-82	3.89	4.80	5.81	6.64	
WASP-84	3.90	4.91	5.81	6.66	
WASP-90	2.83	3.33	3.85	4.36	
WASP-104	3.99	4.88	5.75	6.31	
WASP-106	3.77	4.56	5.41	5.96	

plate scale and detector rotation were 23.46 ± 0.01 mas/px and 1.7° ± 0.1° west of north and 23.51 ± 0.01 mas/px and 2.0° ± 0.1° west of north for the observations in October 2014 and March 2015, respectively.

2.3. Photometry and astrometry

To find all stellar sources, in addition to those that are faint and close to the transiting planet host star, we first subtracted the point spread function (PSF) of the TEP host. Because the PSFs vary significantly from image to image and no standard PSF can be used for all observations, we fitted a theoretical model PSF to each star. The theoretical model PSF comprises the PSF from an ideal telescope without atmosphere, which was then convolved with a Gaussian and finally added to a Moffat profile. The model also weights the two PSF components (see Wöllert et al. 2014, for more information on the procedure). If a companion candidate was found, we fitted a scaled and differently weighted PSF to it to determine its position and the flux ratio of the two components. We used the PSF subtracted images as well to calculate the 5σ-contrast curve. For this purpose, we divided the flux in a box of 5 × 5 pixel around each pixel by the flux of star in a similarly sized box centred on the peak in the original, but not PSF-subtracted image. The contrast at a specific separation is then calculated as the median of the contrast of all pixels at the corresponding separation. The contrast at $r = 0.25''$, $0.5''$, $1.0''$, and $2.0''$ of targets with candidate companions is given in Table 1, and the contrast for all other targets is given in Table 2. Outside of 2.0″, the contrast decreases only very little, and the value given for 2.0″ can be assumed.

The flux ratio in both passbands was measured using the IDL routine APER that performs aperture photometry. We used an aperture size of 4.5 px, which is about the full width half maximum of the stellar PSFs. In contrast to the usual approach, the sky background was not measured in a close annulus around the star, but in a 50 × 50 px box in one corner of the image without a stellar source for the primary and at the opposite position of the TEP host with the same distance and aperture size for the fainter companion. This ensures that the flux contribution of the brighter TEP host is accurately subtracted from those of the fainter source

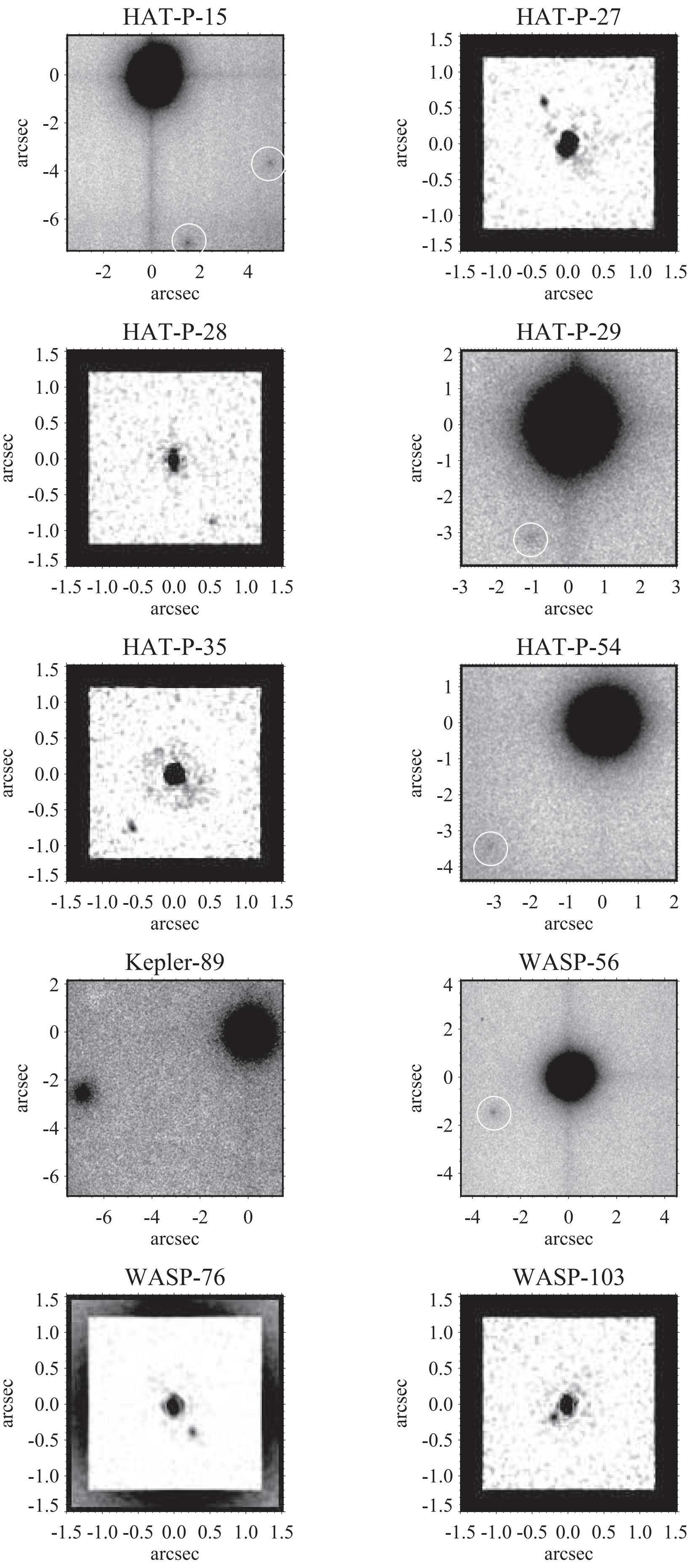

Fig. 1. z' filter images of the 10 exoplanet host stars for which new companion candidates have been detected with the exception of HAT-P-35, for which the i'-image is shown. The grey scale is proportional to the square root of the count. To improve the visibility of the close companions to HAT-P-27, HAT-P-28, HAT-P-35, WASP-76, and WASP-103, we additionally applied unsharp masking. The orientation is identical for all images with north up and east to the left.

Table 3. TEP hosts with candidate companions, observing date, inferred astrometric position, and flux ratio in the observed passbands.

Name	Date of obs.	Sep ["]	PA [°]	$\Delta\, i'$ [mag]	$\Delta\, z'$ [mag]	new?
CoRoT-02	21.10.2014	4.109 ± 0.025	208.56 ± 0.14	3.35 ± 0.15	3.07 ± 0.15	
CoRoT-03	21.10.2014	5.221 ± 0.013	175.62 ± 0.55	3.39 ± 0.25	3.48 ± 0.36	
CoRoT-11	21.10.2014	2.540 ± 0.005	307.38 ± 0.17	2.27 ± 0.09	2.14 ± 0.09	
HAT-P-15 south west	21.10.2014	6.253 ± 0.026	233.42 ± 1.54	7.17 ± 0.49	6.74 ± 0.45	yes
	07.03.2015	6.136 ± 0.014	235.71 ± 1.02	–	6.79 ± 0.22	
HAT-P-15 south	07.03.2015	7.091 ± 0.014	194.23 ± 1.02	–	6.66 ± 0.20	yes
HAT-P-20	21.10.2014	6.925 ± 0.012	321.10 ± 0.11	2.01 ± 0.08	1.67 ± 0.08	
HAT-P-24	06.03.2015	4.965 ± 0.008	171.32 ± 0.60	6.01 ± 0.18	5.80 ± 0.24	
HAT-P-27/WASP-40	27.06.2013[†]	0.656 ± 0.021	25.74 ± 1.19	⋆	⋆	yes
	09.03.2015	0.644 ± 0.007	28.40 ± 1.86	–	4.44 ± 0.32	
HAT-P-28	21.10.2014	0.972 ± 0.019	212.34 ± 2.05	6.2 :	4.09 ± 0.27	yes
HAT-P-29	06.03.2015	3.276 ± 0.104	160.71 ± 1.36	7.93 ± 0.25	6.73 ± 0.35	yes
	21.10.2014	3.285 ± 0.050	161.64 ± 2.36	6.31 ± 0.42	6.11 ± 0.58	
HAT-P-30	09.03.2015	3.842 ± 0.007	4.25 ± 0.14	4.50 ± 0.06	4.03 ± 0.06	
HAT-P-32	09.03.2015	2.930 ± 0.009	110.84 ± 0.43	–	5.43 ± 0.16	
HAT-P-35	09.03.2015	0.933 ± 0.010	139.75 ± 1.23	5.09 ± 0.24	⋆,◦	yes
HAT-P-41	21.10.2014	3.640 ± 0.011	184.00 ± 0.15	3.72 ± 0.13	3.61 ± 0.17	
HAT-P-54	21.10.2014	4.531 ± 0.062	135.95 ± 1.96	5.68 ± 0.53	5.69 ± 0.59	yes
	06.03.2015	4.593 ± 0.010	135.82 ± 0.27	⋆	5.61 ± 0.26	
KELT-2	21.10.2014	2.402 ± 0.008	332.85 ± 0.15	3.19 ± 0.09	3.13 ± 0.09	
	06.03.2015	2.396 ± 0.007	332.81 ± 0.14	2.82 ± 0.15	3.02 ± 0.15	
KELT-3	06.03.2015	3.762 ± 0.009	42.05 ± 0.23	3.93 ± 0.15	3.60 ± 0.15	
Kepler-13	21.10.2014	1.159 ± 0.003	280.02 ± 0.22	0.24 ± 0.02	0.26 ± 0.03	
Kepler-89	21.10.2014	7.316 ± 0.028	108.59 ± 0.11	3.66 ± 0.18	3.37 ± 0.23	yes
KIC10905746	21.10.2014	4.053 ± 0.007	98.61 ± 0.12	2.18 ± 0.16	1.91 ± 0.16	
LHS-6343	21.10.2014	0.723 ± 0.006	119.86 ± 1.30	2.29 ± 0.24	1.66 ± 0.13	
TrES-4	07.03.2015	1.583 ± 0.019	0.69 ± 0.31	4.06 ± 0.07	4.04 ± 0.09	
WASP-11	21.10.2014	0.374 ± 0.013	219.75 ± 0.79	2.94 ± 0.50	2.93 ± 0.45	
	06.03.2015	0.383 ± 0.033	218.33 ± 1.41	3.18 ± 0.26	2.91 ± 0.20	
WASP-12	06.03.2015	1.078 ± 0.008	250.08 ± 0.55	4.13 ± 0.10	3.68 ± 0.08	
WASP-14	06.03.2015	1.425 ± 0.024	102.39 ± 0.40	7.14 ± 0.22	5.95 ± 0.10	
WASP-33	21.10.2014	1.920 ± 0.012	275.87 ± 0.71	9.7 :	7.23 ± 0.22	
WASP-36	09.03.2015	4.845 ± 0.017	67.23 ± 0.95	8.5 :	6.45 ± 0.59	
WASP-56	06.03.2015	3.424 ± 0.009	113.35 ± 0.18	6.85 ± 0.24	5.95 ± 0.22	yes
WASP-70	21.10.2014	3.195 ± 0.029	167.83 ± 0.19	2.62 ± 0.18	2.49 ± 0.20	
WASP-76	21.10.2014	0.425 ± 0.012	216.90 ± 2.93	2.51 ± 0.25	2.85 ± 0.33	yes
WASP-77	21.10.2014	3.282 ± 0.007	154.02 ± 0.12	1.80 ± 0.06	1.63 ± 0.06	
WASP-85	09.03.2015	1.470 ± 0.003	100.09 ± 0.19	0.89 ± 0.01	0.85 ± 0.01	
WASP-103	07.03.2015	0.242 ± 0.016	132.66 ± 2.74	3.11 ± 0.46	2.59 ± 0.35	yes
XO-3	06.03.2015	6.078 ± 0.081	297.21 ± 0.13	8.13 ± 0.28	7.93 ± 0.25	

Notes. In the last column we indicate whether the companion was announced previously. – No observation in this band. (⋆) Companion candidate was too weak for flux measurement. (†) The source was not identified first by us (Wöllert et al. 2015), but it could be located after the new observation with better contrast. (◦) The exposure time in z' was five times shorter than the one in i'.

because our PSFs are almost point symmetrical in shape. The uncertainties of the flux ratios are propagated from the statistical photometric errors given by APER and the systematic errors are from using this method. The latter were estimated by comparing the results obtained by using different aperture sizes, as well as the flux ratios determined by PSF-fitting.

3. Results

For the 74 observed TEP host stars, we find new candidate companions to HAT-P-27, HAT-P-28, HAT-P-35, WASP-76, and WASP-103 within 1″, to HAT-P-29 and WASP-56 within 4″, and the candidates of HAT-P-15, HAT-P-54, and Kepler-89 are situated outside of 4″. Images in z' of all these sources can be found in Fig. 1. In addition, we did follow-up observations of 23 already known companion candidates. The astrometric positions and flux ratios in i' and z' of all companions candidate can be found in Table 3.

As can also be seen in Table 3, most sources appear to be redder than the primary, which would be expected for a lower mass companion. The uncertainties are, however, too large to allow a precise estimate of the spectral type. To achieve this, adaptive-optics-based observations or spectra would be needed. The knowledge of the companion candidate spectral type would then allow the planetary parameter and infrared emission spectra of the new close companions to be corrected, as well as comparing their photometric distance to those of the TEP host star to investigate whether the sources may be gravitationally bound or not. For this purpose their astrometric position needs to be followed up on in the upcoming years as well.

4. Summary

In our ongoing Lucky Imaging search for stellar sources close to transiting exoplanet host stars, we identified five new, close sources within 1″ to HAT-P-27, HAT-P-28, HAT-P-35, WASP-76, and WASP-103, which have been overlooked so far. The planetary and stellar parameters and the thermal radiation profile of the transiting planets of these sources may have to be corrected according to the spectral type of the companion candidate star, which remains to be determined. Also, the detected companion candidates to HAT-P-29 and WASP-56, which are located at 3.3″ and 3.4″, respectively, to the TEP host could have this influence because the photometric aperture used for the transit observations, e.g. with *Spitzer*, are about that size. The sources that are outside of 4″ to HAT-P-15, HAT-P-54, and Kepler-89 do not influence the planetary and stellar property derivation from the transit light curve, but can be of interest if they happen to be bound to the TEP host. This needs to be investigated with astrometric observations in upcoming years. In this work, we also gave the astrometric positions and i' and z' flux ratios of 23 already known candidate companions.

Acknowledgements. M.W. acknowledges support by the International Max Planck Research School for Astronomy & Cosmic Physics in Heidelberg (IMPRS-HD).

References

Adams, E. R., Ciardi, D. R., Dupree, A. K., et al. 2012, AJ, 144, 42
Adams, E. R., Dupree, A. K., Kulesa, C., & McCarthy, D. 2013, AJ, 146, 9
Alonso, R., Auvergne, M., Baglin, A., et al. 2008, A&A, 482, L21
Anderson, D. R., Collier Cameron, A., Delrez, L., et al. 2014, MNRAS, 445,1114
Artymowicz, P., & Lubow, S. H. 1994, ApJ, 421, 651
Baglin, A., Auvergne, M., Barge, P., et al. 2006, in ESA SP 1306, eds. M. Fridlund, A. Baglin, J. Lochard, & L. Conroy, 33
Bakos, G., Noyes, R. W., Kovács, G., et al. 2004, PASP, 116, 266
Bakos, G. Á., Hartman, J., Torres, G., et al. 2011, ApJ, 742, 116
Batalha, N. M., Rowe, J. F., Bryson, S. T., et al. 2013, ApJS, 204, 24
Batygin, K. 2012, Nature, 491, 418
Beatty, T. G., Pepper, J., Siverd, R. J., et al. 2012, ApJ, 756, L39
Bechter, E. B., Crepp, J. R., Ngo, H., et al. 2014, ApJ, 788, 2
Bergfors, C., Brandner, W., Daemgen, S., et al. 2013, MNRAS, 428, 182
Bieryla, A., Collins, K., Beatty, T. G., et al. 2015, AJ, 150, 12
Borucki, W. J., Koch, D., Basri, G., et al. 2010, Science, 327, 977
Brown, D. J. A., Anderson, D. R., Armstrong, D. J., et al. 2014, ArXiv e-prints [`arXiv:1412.7761`]
Burke, C. J., Bryson, S. T., Mullally, F., et al. 2014, ApJS, 210, 19
Collins, K. A., Eastman, J. D., Beatty, T. G., et al. 2014, AJ, 147, 39
Colón, K. D., Ford, E. B., & Morehead, R. C. 2012, MNRAS, 426, 342
Crossfield, I. J. M., Barman, T., Hansen, B. M. S., Tanaka, I., & Kodama, T. 2012, ApJ, 760, 140
Crossfield, I. J. M., Petigura, E., Schlieder, J. E., et al. 2015, ApJ, 804, 10
Daemgen, S., Hormuth, F., Brandner, W., et al. 2009, A&A, 498, 567
Deleuil, M., Deeg, H. J., Alonso, R., et al. 2008, A&A, 491, 889
Désert, J.-M., Charbonneau, D., Torres, G., et al. 2015, ApJ, 804, 59
Dressing, C. D., Adams, E. R., Dupree, A. K., Kulesa, C., & McCarthy, D. 2014, AJ, 148, 78
Everett, M. E., Barclay, T., Ciardi, D. R., et al. 2015, AJ, 149, 55
Fabrycky, D., & Tremaine, S. 2007, ApJ, 669, 1298
Faedi, F., Staley, T., Gómez Maqueo Chew, Y., et al. 2013, MNRAS, 433, 2097
Fischer, D. A., Schwamb, M. E., Schawinski, K., et al. 2012, MNRAS, 419, 2900
Gandolfi, D., Hébrard, G., Alonso, R., et al. 2010, A&A, 524, A55
Guenther, E. W., Fridlund, M., Alonso, R., et al. 2013, A&A, 556, A75
Hartman, J. D., Bakos, G. Á., Béky, B., et al. 2012, AJ, 144, 139
Horch, E. P., Howell, S. B., Everett, M. E., & Ciardi, D. R. 2014, ApJ, 795, 60
Hormuth, F., Brandner, W., Hippler, S., & Henning, T. 2008, J. Phys. Conf. Ser.,131, 012051
Howell, S. B., Everett, M. E., Sherry, W., Horch, E., & Ciardi, D. R. 2011, AJ,142, 19
Johnson, J. A., Apps, K., Gazak, J. Z., et al. 2011, ApJ, 730, 79
Kane, S. R., Howell, S. B., Horch, E. P., et al. 2014, ApJ, 785, 93
Law, N. M., Morton, T., Baranec, C., et al. 2014, ApJ, 791, 35
Lillo-Box, J., Barrado, D., & Bouy, H. 2012, A&A, 546, A10
Lillo-Box, J., Barrado, D., & Bouy, H. 2014, A&A, 566, A103
Maxted, P. F. L., Anderson, D. R., Collier Cameron, A., et al. 2013, PASP, 125,48
Mayer, L., Wadsley, J., Quinn, T., & Stadel, J. 2005, MNRAS, 363, 641
Montet, B. T., Johnson, J. A., Muirhead, P. S., et al. 2015, ApJ, 800, 134
Moya, A., Bouy, H., Marchis, F., Vicente, B., & Barrado, D. 2011, A&A, 535,A110
Naoz, S., Farr, W. M., Lithwick, Y., Rasio, F. A., & Teyssandier, J. 2011, Nature,473, 187
Narita, N., Takahashi, Y. H., Kuzuhara, M., et al. 2012, PASJ, 64, L7
Ngo, H., Knutson, H. A., Hinkley, S., et al. 2015, ApJ, 800, 138
Pepper, J., Siverd, R. J., Beatty, T. G., et al. 2013, ApJ, 773, 64
Pollacco, D. L., Skillen, I., Collier Cameron, A., et al. 2006, PASP, 118, 1407
Roell, T., Neuhäuser, R., Seifahrt, A., & Mugrauer, M. 2012, A&A, 542, A92
Sanchis-Ojeda, R., Winn, J. N., Marcy, G. W., et al. 2013, ApJ, 775, 54
Santerne, A., Moutou, C., Barros, S. C. C., et al. 2012, A&A, 544, L12
Siverd, R. J., Beatty, T. G., Pepper, J., et al. 2012, ApJ, 761, 123
Smith, A. M. S., Anderson, D. R., Collier Cameron, A., et al. 2012, AJ, 143, 81
Wang, J., Fischer, D. A., Xie, J.-W., & Ciardi, D. R. 2014, ApJ, 791, 111
Winn, J. N., Noyes, R. W., Holman, M. J., et al. 2005, ApJ, 631, 1215
Wöllert, M., Brandner, W., Reffert, S., et al. 2014, A&A, 564, A10
Wöllert, M., Brandner, W., Bergfors, C., & Henning, T. 2015, A&A, 575, A23
Wu, Y., & Murray, N. 2003, ApJ, 589, 605

4

The young binary HD 102077: Orbit, spectral type, kinematics, and moving group membership

The investigation of the binary system HD 102077 was thought to get acquainted with the Lucky Imaging data analysis and other useful astronomical techniques as orbit and age determination, light curve analysis, and spectroscopy. It is not in line with the other work of the thesis, but rather a project on its own. The idea behind the project was to investigate whether HD 102077 is a member of the young and nearby moving group TW Hya (TWA) and to determine its age. TWA comprises about two dozen members whereof some are brown dwarfs. To understand the formation and evolution of brown dwarfs after the early phase of Deuterium burning, but also of the planets, basic physical properties as luminosity, mass and age need to be measured for individual objects. While the luminosity can be measured directly when knowing the distance, a correct determination of mass and age is more challenging, but possible if the brown dwarf is known to belong to a cluster with a reasonable age estimate. We find, however, that HD 102077 is very likely not a member of this moving group and thus its age can not be used for the TWA age determination.

A&A 564, A10 (2014)
DOI: 10.1051/0004-6361/201323262

Astronomy
&
Astrophysics

The young binary HD 102077: Orbit, spectral type, kinematics, and moving group membership*

Maria Wöllert[1], Wolfgang Brandner[1], Sabine Reffert[2], Joshua E. Schlieder[1],
Maren Mohler-Fischer[1], Rainer Köhler[1], and Thomas Henning[1]

[1] Max-Planck-Institut für Astronomie, Königstuhl 17, 69117 Heidelberg, Germany
e-mail: `woellert@mpia.de`
[2] Landessternwarte, Königstuhl 12, 69117 Heidelberg, Germany

Received 17 December 2013 / Accepted 5 February 2014

ABSTRACT

The K-type binary star HD 102077 was proposed as a candidate member of the TW Hydrae association (TWA) which is a young (5−15 Myr) moving group in close proximity (∼50 pc) to the solar system. The aim of this work is to verify this hypothesis by different means. We first combine diffraction-limited observations from the ESO NTT 3.5 m telescope in SDSS-i' and SDSS-z' passbands (three epochs) and ESO 3.6 m telescope in H-band (one epoch) with literature data to obtain a new, amended orbit fit of the visual binary. We then estimate the spectral types of both components from the $i' - z'$ colours and reanalyse the Hipparcos parallax and proper motion taking the orbital motion into account. Moreover, we use two high-resolution spectra of HD 102077 obtained with the fibre-fed optical echelle spectrograph FEROS at the MPG/ESO 2.2 m telescope to determine the radial velocity and the lithium equivalent width (EW) of the system. Finally, we use all the information to discuss the kinematic properties of HD 102077 and to estimate the age of the system. The orbital elements of the HD 102077 trajectory are well constrained and we derive a total system mass of $2.6 \pm 0.8\ M_\odot$ and a semi-major axis of 14.9 ± 1.6 AU. From the $i' - z'$ colours we infer an integrated spectral type of K2V, and individual spectral types of $K0 \pm 1$ and $K5 \pm 1$ for primary and secondary, respectively. The radial velocity corrected for the orbital motion of the system is 17.6 ± 2 km s^{-1}. Even though the parallax determination from the Hipparcos data is not influenced by the orbital motion, the proper motion changes to $\mu_\alpha * \cos\delta = -137.84 \pm 1.26$ mas yr^{-1} and $\mu_\delta = -33.53 \pm 1.45$ mas yr^{-1}. With the resultant space motion, the probability of HD 102077 being a member of TWA is less than 1%. Furthermore, the lithium equivalent width of 200 ± 4 mÅ is consistent with an age between 30 Myr and 120 Myr and thus older than the predicted age of TWA. The comparison of HD 102077's temperature and luminosity to isochrones supports this result. In conclusion, HD 102077's age, galactic space motion, and position do not fit TWA or any other young moving group.

Key words. instrumentation: high angular resolution – astrometry – binaries: general – stars: fundamental parameters – stars: individual: HD 102077 – stars: late-type

1. Introduction

The TW Hya association (TWA) is a loose group of stars (Gregorio-Hetem et al. 1992) that have common galactic kinematics, age, and origin (Kastner et al. 1997; Weinberger et al. 2013). The association has 22 high probability members with individual distances between 28 pc and 70 pc (Torres et al. 2008). The age of its members has been estimated using different indicators of youth such as activity and lithium abundance as well as their position in the Hertzsprung-Russell diagram and is about 10 ± 5 Myr (Weinberger et al. 2013). Young, nearby associations like TWA are of great importance to understanding the local star forming history, and provide a sample of young stars, brown dwarfs, and planets for high-resolution studies. Therefore, several groups have been looking for additional members (Schlieder et al. 2010, 2012a; Zuckerman et al. 2011; Shkolnik et al. 2012; Rodriguez et al. 2013; Malo et al. 2013; Moór et al. 2013).

The binary HD 102077 (also called HIP 57269, V 838 Cen, and RST 3558AB) was proposed as a candidate member of TWA based on its kinematics by Makarov & Fabricius (2001). Kinematic candidate members, however, need to be verified by spectroscopic measurements. The first spectroscopic follow up was done by Song et al. (2002), who measured the Li 6708 Å strength of HD 102077. They find a fairly large equivalent width (EW) of 196 mÅ, which is a strong indication of a young system. The authors argue, however, that an age of more than 30 Myr is more likely and thus do not consider HD 102077 as a new member of TWA. Apart from the lithium absorption line, HD 102077 shows strong X-ray emission which also hints at a young age (Makarov 2003). The WISE data (Cutri et al. 2012) shows, however, no infrared excess and thus no sign of a disk. Even though HD 102077 is a young star, several research groups have assigned it low metallicity values. Holmberg et al. (2007) used the Stroemgren UVBY photometry by Olsen (1994) to derive a [Fe/H] of −0.9. Casagrande et al. (2011) redid their analysis and find [Fe/H] = −0.76. An independent metallicity measurement was done by Randich et al. (1993). They fitted spectral templates to high-resolution spectra with $R = 50\,000$ over the region of ≈6680–6730 Å and obtained [Fe/H] = −0.4. The photometric determination of the metallicity content is not very accurate because of HD 102077s binarity and variability and this may be the cause of the discrepancy. For instance, Cutispoto (1990) measured the $UBVRI$ colours over several photometric phases

---

* Based on observations made with ESO Telescopes at the La Silla Paranal Observatory under programme IDs 084.D-0669(A), 088.C-0753(A), 091.D-0494(A), 53.7-0107, 091.A-9013(A).

and observed that $U-B$ varies by 0.04 mag and that the star gets bluer at light maximum. Even stronger variations have been observed by Udalski & Geyer (1985). They find brightness changes of 0.08 mag with a probable period of 1.84 or 2.2 days. Since the V-band lightcurves at different epochs differ greatly in shape and mean magnitude (Cutispoto 1990, 1993, 1998) the starspot size and distribution seem to vary considerably. Duplicity of one of the two components could also add to the observed variations.

König et al. (2003) measured the radial velocity of the system and find that the space motion is quite different from the average space velocity of TWA. Nevertheless, they point out that the distance of HD 102077, its location in the sky, its spectral type, its position in the H-R diagram, its $v \sin i$, and X-ray emission are very similar to other confirmed TWA members. This group also presents evidence of a third component in the system. The proposed star is at a distance of 8.46″ from the primary and it shows calcium and lithium absorption. The lithium EW of 0.18 ± 0.2 Å and a spectral type of $K5 \pm 1$ point to a similar age to the A component. We checked the imaging archives to see whether there is an indication of common proper motion. The stars do seem to move together with respect to the background stars in the field when comparing an R-band image from 1983 to an R-band image from 1992 and the 2MASS K-band image from 1999. The point spread functions (PSFs) are, however, blended in all these images and thus no quantitative proper motion measurement is possible. Nevertheless, the calcium and lithium absorption features as well as the likely common proper motion is strong evidences of a bound system.

The integrated spectral type of HD 102077 of $K0/1Vp$ was first determined by Anders et al. (1991) by high-dispersion observations of the Li 6707 Å doublet and König et al. (2003) find $K1/2$ using DFOSC at the 1.54 m Danish telescope. The spectral type of the primary components is, however, less clear. Fabricius & Makarov (2000) analysed the Hipparcos Tycho data and find that the brighter component has a redder $B-V$ colour, corresponding to spectral types K4 and K2, but they do not give an explanation for this unexpected result. Cutispoto (1998) uses the $UBVRI$ colours of the integrated system and ΔH_p from the Hipparcos satellite catalog to classify HD 102077 as consisting of a $K0/1V$ and a $K5V$.

The source HD 102077 is a visual binary star and thus allows the determination of the total system mass. The first orbital parameters were derived by Heintz (1986). His best fit to data from seven epochs is a low eccentricity orbit with a period of 32.35 years and a semi-major axis of 0.28″. At that time, the parallax of HD 102077 was not known. Therefore, Heintz used Kepler's Third Law and the mass-luminosity relation to estimate the dynamical parallax. He obtained 42.3 pc and deduced a total system mass of 1.6 $M_\odot$.

In this paper, we present the results of our astrometric, photometric, and spectroscopic study of HD 102077. We derive a new orbit fit of the binary system, and we determine the $i'-z'$ colours and from these the spectral types of the individual components. We measure the radial velocity and the lithium EW of the system. Finally, we use these results to discuss a possible TWA membership of HD 102077.

2. Observations and data reduction

2.1. Literature data

The source HD 102077 has been observed in the optical with various telescopes and instruments since 1929 (see Table 1). All measurements until 1985 were done with a filar micrometer. Because of the small separation of the two components close to the resolution limit of the telescopes used, we adopt a high uncertainty in the separation of 0.1″ and 5° in the position angle for all micrometer measurements. The uncertainties of the later measurements are the values reported by the authors in the papers or in follow-up studies. We note that the binary was not resolved by Worley in 1972 nor by Heintz in 1984 (Heintz 1986).

Table 1. Astrometric measurements of HD 102077.

Date	PA [°]	ρ [″]	Ref.
1929.065	348.9 ± 5.0	0.24 ± 0.1	Ro
1949.529	270.0 ± 5.0	0.17 ± 0.1	Ro
1964.32	60.5 ± 5.0	0.19 ± 0.1	Ho
1976.125	164.4 ± 5.0	0.14 ± 0.1	Wo
1980.231	243.5 ± 5.0	0.14 ± 0.1	Wo
1983.168	264.6 ± 5.0	0.19 ± 0.1	Wo
1985.34	278.5 ± 5.0	0.33 ± 0.1	He
1989.3059	298.7 ± 0.2	0.416 ± 0.003	Mc
1990.3462	302.9 ± 0.2	0.42 ± 0.003	Ha
1991.25	306 ± 1.0	0.43 ± 0.006	Hi
1994.504	320.2 ± 0.7	0.418 ± 0.004	*
2001.0825	352.9^a ± 0.7	0.335 ± 0.004	Ma
2009.2598	115.5 ± 0.3	0.1795 ± 0.001	To
2010.08	135.9 ± 0.5	0.183 ± 0.003	*
2011.0373	157.3^a ± 0.2	0.1874 ± 0.002	Hk
2012.011	177.3 ± 0.5	0.196 ± 0.003	*
2013.3042	202.9 ± 0.7	0.21 ± 0.003	*

References. Ro: Rossiter (1955), Ho: Holden (1965), Wo: Worley (1978), He: Heintz (1986), Mc: McAlister et al. (1990), Ha: Hartkopf et al. (1993), Hi: ESA (1997), Ma: Mason et al. (2011), To: Tokovinin et al. (2010), Hk: Hartkopf et al. (2012), *: this work, (a) position angle corrected by 180°.

2.2. AO observation with COME-on+/SHARPII

The observations of HD 102077 in the H-band were obtained on July 2, 1994, with the adaptive optics (AO) system ComeOn+ (Rousset et al. 1994) and the near-infrared camera Sharp2 (Hofmann et al. 1992) at the ESO 3.6 m telescope in La Silla, Chile. For sky subtraction, HD 102077 was observed in two different quadrants of the detector with 30 individual frames each. Exposure times of the single frames were 1 s. The star positions for both configurations were measured with IRAF imexamine assuming a two-pixel object radius. Their values were averaged, and the standard deviation was used to estimate measurement uncertainties.

Astrometric calibrations were achieved through observations of the astrometric binary IDS 17430S6022 (van Dessel & Sinachopoulos 1993). These observations yield an image scale of 50.20 ± 0.12 mas/pixel and show that the y-axis of the detector was aligned with the north direction to within ±0.20 deg.

2.3. Lucky Imaging with AstraLux

Three additional epochs were obtained using the Lucky Imaging camera AstraLux Sur at the ESO 3.5 m New Technology Telescope at La Silla (see Hormuth et al. 2008; Hippler et al. 2009, for more information on AstraLux). Lucky Imaging is a passive technique which enables nearly diffraction-limited observations on 2- to 4-m telescopes. The seeing is reduced by taking a series of many short exposures of the target and combining only the least distorted frames to the final image.

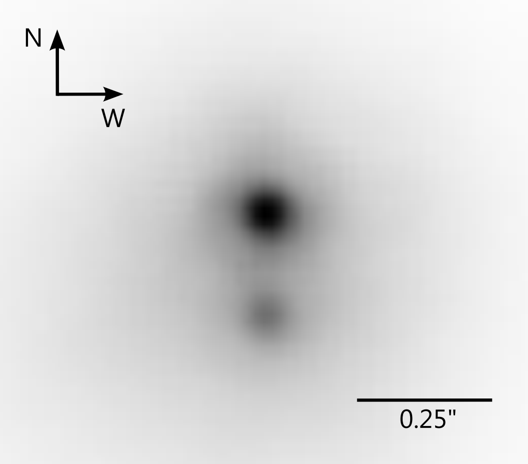

Fig. 1. z' filter image of HD 102077 with AstraLux at La Silla observatory from January 5, 2012. The image scale is linear.

We observed HD 102077 on February 7, 2010; on January 2, 4, and 5, 2012; and on April 21, 2013. At each time we imaged HD 102077 in i'- and z'-passband except on January 4, 2012, when we only took a z'-band image, and January 2, 2012 when we observed HD 102077 in z'-band twice. The z'-band image from January 5, 2012, is shown in Fig. 1 as an example. The exposure time of individual frames was 30 ms in 2010 and 15 ms on the other dates. In order to match a total integration time of 300 s, the number of integrations was set to 10 000 and 20 000, respectively.

The single frames were corrected for electronic offset and differences in pixel sensitivity using a masterflat and -bias, respectively. After noise filtering and resampling the pixel scale from 30.5 mas/pixel to 15.25 mas/pixel, the Strehl ratio of the PSF was measured. Only 1% of the images with the highest Strehl ratio were then combined to the final image. The assembling is based on the Drizzle algorithm (Fruchter & Hook 2002). It shifts the selected images such that the brightest pixel of the reference star is always positioned at the same pixel coordinates.

Astrometric reference stars in the open cluster NGC 3603 were observed each night to calibrate the detector rotation and pixel scale. We measured the detector position for five stars of NGC 3603 with IRAF imexamine, calculated the separation and rotation angle pairwise, and compared these values to data from high-quality astrometric HST/WFP2 observations (Rochau et al. 2010). This analysis yielded a plate scale of 15.25 ± 0.03 mas/px, 15.25 ± 0.01 mas/px, and 15.24 ± 0.02 mas/px and a detector rotation of 1.8° ± 0.2°, 2.1° ± 0.2°, and 3.8° ± 0.2° west of north in 2010, 2012, and 2013 respectively. Additionally, twilight skyflats and bias were measured in both filters at the beginning of each observing night.

The positions of the binary components as well as their magnitude differences in the i' and z' filters were obtained by fitting a model PSF to the data. The co-adding of images of short exposures with random atmospheric distortions is described by (Hormuth et al. 2008):

$$\mathrm{PSF_{obs}}(r) = W\left(\frac{1}{r^2/\sigma_\mathrm{m}^2+1}\right)^{\beta} + (1-W)\left(\mathrm{PSF_{th}}(r) * \frac{1}{\sqrt{2\pi\sigma_\mathrm{g}^2}}\exp\left(-\frac{r^2}{2\sigma_\mathrm{g}^2}\right)\right). \quad (1)$$

On the right-hand side $\mathrm{PSF_{th}}$ is the ideal point spread function without atmospheric turbulences and telescope aberrations, which is then convolved with a Gaussian blurring function of parameter σ_g. To obtain the observed PSF, a Moffat profile with parameters β and σ_m is added to the blurred theoretical profile; W weights the two PSF components. Our code determines all parameters simultaneously by a Levenberg-Marquardt least-squares fit to both binary components.

In order to unveil systematic errors of the code we constructed binaries from seven single stars that we imaged on the same night. The synthetic binaries had similar separation and brightness ratios to HD 102077, and were introduced at position angles of 0°, 45°, 90°, 135°, 180°, and 270°. We compared the fit results with the set system properties and found no systematic offset in separation, position angle, and flux ratio.

In addition to the flux ratio of the binary component aperture photometry with IRAF apphot was used for our observations from 2010 to determine the i' and z' magnitudes of the integrated system. We chose an aperture radius of 21 px centred on the primary star to ensure that most of the flux of both components is covered. The sky background was measured in an annulus from 25 px to 35 px. The corresponding photon flux is then calculated taking into account the system gain, the exposure time, the mirror area, and the quantum efficiency of our CCD in i' and z' passband which is 0.8 and 0.4, respectively. For an absolute calibration of the instrument we observed two astrometric standard stars at a comparable airmass during the same night and analysed them in the same way. To calibrate our instrument we only considered offsets between our instrumental magnitude and the standard value given in literature and no colour terms.

2.4. High-resolution spectroscopy with FEROS

Two high-resolution spectra of HD 102077 were obtained on July 26 and July 27, 2013, with the fibre-fed optical echelle spectrograph FEROS (Kaufer & Pasquini 1998) at the MPG/ESO 2.2 m telescope at La Silla Observatory in Chile. FEROS covers the whole optical spectral range from 3600 Å to 9200 Å and provides a spectral resolution of ≈48 000. The fibre aperture of FEROS is 2 arcsec and thus contains the light of both components. The exposure time of each spectrum was 1500 s and resulted in a signal-to-noise ratio (S/N) of 223 and 192 at 5450 Å, respectively. The spectra were taken in the objectcal mode and were reduced with the online Data Reduction System (DRS) at the telescope. The reduction includes detection of spectral orders, wavelength calibration and background subtraction, flatfield correction and order extraction, as well as merging the individual orders after rebinning the reduced spectra to constant wavelength steps. Since the FEROS pipeline applies the barycentric correction inaccurately (Müller et al. 2013), we recalculated the barycentric correction with the IDL routine baryvel.pro including the rotation of Earth at the observatory.

The stellar parameters of HD 102077 are determined by fitting synthetic spectra to the stellar spectrum using the spectral synthesis code Spectrocopy Made Easy, SME (Valenti & Piskunov 1996). We use these stellar parameters to compute a template spectrum which we then cross-correlate with the measured spectrum to determine the radial velocity of the system. Furthermore, we measure the Li 6708 Å EW.

3. Physical properties of the HD 102077 binary

3.1. Orbit determination

The orbit of a binary system can be characterized by the relative motion of the secondary around the primary. Even though

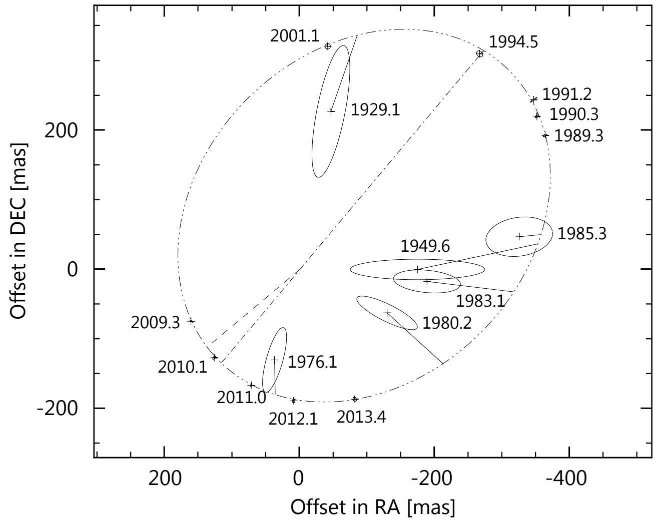

Fig. 2. Best fitting orbit of HD 102077 in the rest frame of the primary. The observed positions are marked by their error ellipses and lines connecting the observed and calculated positions at the time of the observation. The dash-dotted line indicates the line of nodes, the dashed line the periastron. We note that the micrometer measurements all tend to estimate a smaller projected separation.

Table 2. Parameters of the best orbital solution.

Orbital element	Value
Date of periastron T_0 (JD)	$2\,455\,142^{+4}_{-6}$
Period P (years)	$35.5^{+0.3}_{-0.3}$
Semi-major axis a (mas)	$306.2^{+1.1}_{-1.4}$
Inclination i (°)	$28.5^{+0.4}_{-1.3}$
Eccentricity e	$0.409^{+0.004}_{-0.002}$
Argument of periastron ω (°)	$348.60^{+0.09}_{-0.91}$
PA of ascending node Ω (°)	$140.0^{+0.1}_{-1.3}$
System mass M_S ($M_\odot$/kpc^3)	$22\,834^{+265}_{-359}$
Semi-major axis a (AU)	$14.9^{+1.6}_{-1.6}$
System mass M_S ($M_\odot$)	$2.6^{+0.8}_{-0.8}$

we only see a projection of the movement on the celestial sky, a sequence of observations at many different epochs, preferably covering more than one complete orbit, makes it possible to determine all orbital elements. The astrometric data of HD 102077 covers more than two full orbits (see Table 1).

To find the best fit to that data we employ a grid-search in eccentricity e, period P, and time of periastron T_0. For every set of these values we solve the Kepler equation and we get the eccentric anomaly E for every point in time t that has been measured:

$$E - e \sin E = \frac{2\pi}{P}(t - T_0).$$

Then the elliptical rectangular coordinates of the real orbit X and Y are calculated at every epoch,

$$\begin{aligned} X &= \cos E - e \\ Y &= \sqrt{1 - e^2} \cdot \sin E, \end{aligned}$$

and X and Y are connected with the measured projected points x, y via the four Thiele-Innes coefficients A, B, F, G:

$$\begin{aligned} x &= A \cdot X + F \cdot Y \\ y &= B \cdot X + G \cdot Y. \end{aligned}$$

The Thiele-Innes coefficients in turn depend on the orbital elements, the semi-major axis a, the angle between node and periastron ω, the position angle of the line of nodes Ω, and the inclination i:

$$\begin{aligned} A &= a\,(\cos\omega\cos\Omega - \sin\omega\sin\Omega\cos i) \\ B &= a\,(\cos\omega\sin\Omega + \sin\omega\cos\Omega\cos i) \\ F &= a\,(-\sin\omega\cos\Omega - \cos\omega\sin\Omega\cos i) \\ G &= a\,(-\sin\omega\sin\Omega + \cos\omega\cos\Omega\cos i). \end{aligned}$$

Using all epochs A, B, F, and G are calculated using singular value decomposition. Finally, the orbital elements can be computed. The goodness of every fit is measured with the χ^2 test. The minimal χ^2 corresponds to the best fit. The best orbital solution for HD 102077 has a reduced χ^2 of 2.6 and can be seen in Fig. 2; the corresponding orbital elements can be found in Table 2. Uncertainties were estimated by analysing the χ^2 function around its minimum. The errors given in Table 2 represent the 68% confidence interval (see Köhler et al. 2008 for more details).

The semi-major axis of 14.9 ± 1.6 AU and the system mass of $2.6 \pm 0.8\ M_\odot$ were calculated using the revised Hipparcos parallax of 20.6 ± 2.1 mas. The uncertainties of these values are clearly dominated by the distance uncertainty. We note that we excluded the data point from 1964 for our orbital fit. It shows a significant and unexplainable offset compared to all other data points and we have no means to recheck its derivation. We also added 180° to the position angle measurements from 2001 and 2011 in order to match the other observations.

3.2. *Stellar parameters*

3.2.1. $i'-z'$ colours

The spectral type of the integrated system as well as the spectral types of the individual components are determined from $i' - z'$ colours which we compare to the spectral type models for main-sequence stars by Kraus & Hillenbrand (2007). Even though HD 102077 may still be in its pre-main-sequence phase, it is reasonably close to the zero-age main sequence to justify the adoption of main-sequence colours and magnitudes. We derive an integrated spectral type of K2V. To determine the $i' - z'$ colours of the individual components we need to disentangle their signal. This is achieved by fitting a theoretical PSF to both stars simultaneously. Averaging the results of all five z'-band images and three i'-band images we get a flux ratio of 0.377 ± 0.02 and 0.325 ± 0.01, respectively. Together with the apparent integrated i'- and z'-magnitudes, this yields a spectral type of $K0 \pm 1$ for the primary and $K5$ ± 1 for the secondary.

3.2.2. Spectra

In fitting model spectra to our binary system we find $T_\mathrm{eff} \approx$ 5265 K, $\log g \approx 4$, Fe/H ≈ -0.37, and $\upsilon \sin i \approx 8.3$ km s^{-1}. However, these results should be taken with care since we only fit one component to the unresolved binary system. The lines are expected to be broadened from the relative motion of the two components which can be calculated from our orbit fit to be 5 ± 0.5 km s^{-1} in July 2013 when the spectra were taken. We find a radial velocity of 19.8 km s^{-1} with a small uncertainty of 0.1 km s^{-1} introduced by the measurement and larger uncertainty introduced by the orbital motion. The measured velocity

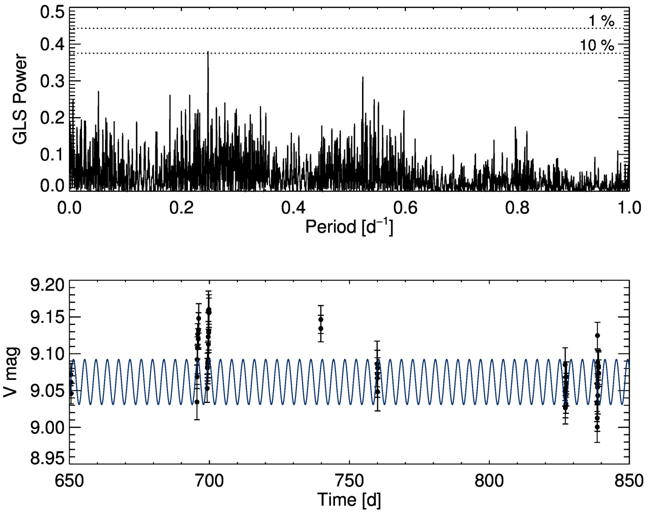

Fig. 3. *Top*: generalized Lomb-Scargle periodogram for Hipparcos V-band data. The highest power is reached for a period of 4.04 days. The false alarm probability of 1% and 10% are indicated by the dotted lines. *Bottom*: a part of the Hipparcos light curve is overplotted with the most significant periodic signal.

lies between the radial velocity of the primary and the secondary and it depends on the mass ratio and on the flux ratio of the two components. Since the exact values are not known we adopt an uncertainty of 2.5 km s^{-1}, half of the relative speed, corresponding to the highest possible uncertainty.

We also calculated the radial velocity of the individual components with an IDL analysis package that is based on the 2D cross correlation technique described in Mazeh et al. (2002) (Bender, priv. comm.). The cross correlation of the two spectra of HD 102077 with one K0 template gives 19.8 ± 0.4 km s^{-1} and confirms the above mentioned value. The simultaneous cross correlation with an K0 and an K5 template increases the correlation coefficient significantly and gives an individual radial velocity of 26.5 ± 0.9 km s^{-1} for the primary and 12.7 ± 0.7 km s^{-1} for the secondary in four different wavelength ranges and in both spectra. The radial velocity difference of about 14 km s^{-1} of the two components does not agree with the predicted value of 5 km s^{-1} from our orbit fit. This could be explained either by a third component in the system or by a parallax measurement that is too large by about a factor of 2.8. The second would, however, lead to an unreasonably high system mass of about 57 $M_{\odot}$. In addition, our reanalysis of the Hipparcos parallax does not suggest an incorrect parallax determination (see Sect. 4.3).

3.3. V-band variability

We analysed the variability of HD 102077 by studying the Hipparcos V-band data. During the mission lifetime the satellite scanned 166 times over HD 102077. The observations span more than three years and thus have a much longer baseline than all previous measurements. To find repeating signals we calculated the generalized Lomb-Scargle periodogram (Zechmeister & Kürster 2009) shown in Fig. 3. The highest power is obtained by a period of 4.04 days followed by a period of 1.8 days. These powers are, however, small and are most likely not associated with a real signal. To test whether the maximum peaks arose just by chance we deleted 20% of the data randomly and recalculated the periodogram; this procedure was repeated several times. Most often we find different prominent peaks. In addition, we analysed the light curve with two algorithms which do not assume a sinusoidal signal: a) box-fitting least squares (Kovács et al. 2002) which is optimized to find periodic transits; and b) Plavchan (Plavchan et al. 2008) which makes no assumption about the underlying periodic signal. Neither of these algorithms shows a solution with a high power and the most likely periods differ when deleting 20% of data randomly. This suggests that apart from the brightness variation of HD 102077 due to stellar activity as has also been seen in the shorter period observations (Cutispoto 1990, 1993, 1998) no other signal can be detected in the Hipparcos data.

3.4. Age estimate

3.4.1. Using isochrones

We use Pisa (FRANEC) pre-main-sequence isochrones (Tognelli et al. 2011) to estimate the age of HD 102077. The isochrones are computed for a fine grid of mass, age, metallicity, and helium abundance and give the bolometric luminosity as a function of the effective temperature of stars at a certain age. We deduce the effective temperature of HD 102077's two components from our spectral type estimates using the stellar SEDs of Kraus & Hillenbrand (2007). We find $\log T_{\rm eff} = 3.73^{+0.025}_{-0.015}$ for the primary and $\log T_{\rm eff} = 3.63^{+0.030}_{-0.022}$ for the secondary. We calculate the bolometric luminosity from the Tycho V_T and B_T colours of 9.44 mag and 10.50 mag for the primary and 10.56 mag and 11.47 mag for the secondary. We assume that the uncertainty of the Tycho-magnitudes is dominated by the stellar variability whose 1σ value is 0.04 mag. Using the theoretical calibration from Tycho to Johnson magnitudes (Bessell 2000) and the bolometric correction from Voigt (1988) we find a bolometric magnitude of $5.60^{+0.21}_{-0.23}$ mag for the primary and $6.33^{+0.21}_{-0.23}$ mag for the secondary. We now place both components in a H-R diagram (see Fig. 4) together with Pisa pre-main-sequence isochrones. As input parameters we use a metallicity value of −0.4 dex as was determined by Randich et al. (1993) and our own FEROS measurement and we assume solar helium mass fraction and mixing length. We overlayed stellar tracks for comparison. Both components lie above the main sequence, with an age between 25 Myr and 100 Myr for the primary, and 15 Myr and 50 Myr for the secondary.

3.4.2. Using the lithium I λ6708 Å equivalent width

To determine the stellar age independently from the stellar parameters, the EW of the Li I λ6708 Å line can be used (Wallerstein & Conti 1969). The reaction rates of the lithium burning depends on the age of the star and on its mass, and the corresponding effective temperature and young stars exhibit larger Li features than older stars. Although this age estimation method is under discussion because non-steady accretion can heavily affect the Li I depletion (Baraffe & Chabrier 2010), it is still a commonly used age indicator (e.g. Thomann et al. 2013).

Since the Li I line at 6708 Å is blended with an Fe I line, the line was fitted with a Voigt profile to account for the blending. Using the Voigt fit, the EW was derived. By using the S/N of the spectra as a weight, the average Li EW with error was calculated from the individual EWs derived from each single spectrum. Since the binary does not show WISE IR-excess, disk accretion is unlikely to occur and we do not expect veiling (Lynden-Bell & Pringle 1974; Kenyon & Hartmann 1987; Bertout et al. 1988). The resulting Li I EW is 200 ± 4 mÅ which agrees well with the

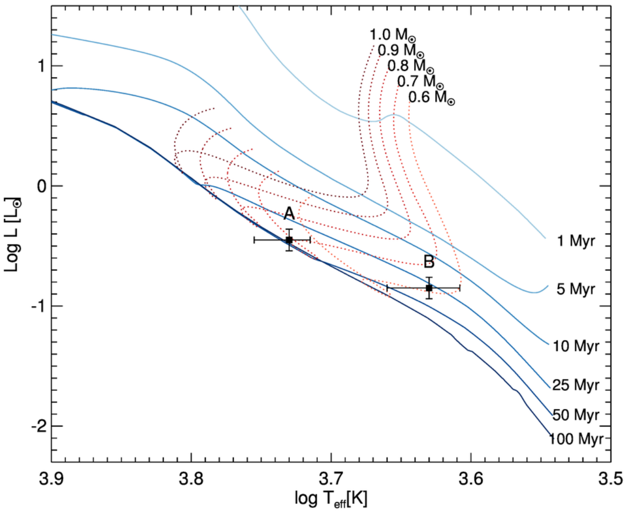

Fig. 4. Position of both components of HD 102077 in an H-R diagram along with the Pisa pre-main-sequence tracks and isochrones (Tognelli et al. 2011) for a metal abundance of $Z = 0.005$, a helium fraction of $Y = 0.273$, and a mixing length of ML = 1.68.

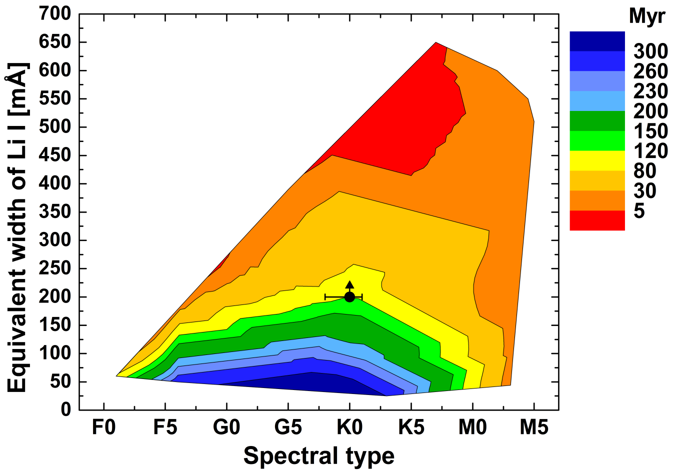

Fig. 5. Li I EW over spectral type. The coloured contours show the age calibration of Zuckerman & Song (2004). The black circle indicates the upper limit of the age of the primary component with spectral type error bars from photometry.

previously measured values for HD 102077 (Song et al. 2002) and its probable third, wider component discovered by König et al. (2003).

In order to determine the stellar age from the derived Li EW, an age calibration is needed. Zuckerman & Song (2004) used eight different stellar associations with calculated Li EWs and independently derived mean age. By doing so, they derived an age calibration of Li I EW over $(B - V)$ and spectral type, allowing a simple placement of object measurements in the calibration.

Figure 5 shows the Li EW measurement of HD 102077 of 200 ± 4 mÅ in the diagram. This corresponds to a maximum age of 120 Myr. The minimum age is not as well constrained as we measure the EW of the combined signal, and the later K-type secondary star is expected to have a smaller EW than the primary. The lithium analysis would benefit from taking the binarity of the system into account. Our spectral resolution and the S/N are, however, not high enough to disentangle the signal of both stars.

4. Discussion

4.1. Additional companions

In addition to the wide companion candidate described by König et al. (2003), our mass estimate of $2.6 \pm 0.8\ M_{\odot}$ may indicate that HD 102077 has another, so far unknown companion; this is considered because the two K-type stars should be less massive than $1.6\ M_{\odot}$. This would be in accordance with the classification as RS CVn by Weiler & Stencel (1979), Gurzadian & Cholakian (1992), and Pallavicini et al. (1992). In addition, the 2D cross correlation shows a large radial velocity difference which is in disagreement with the orbital fit, but could be caused by a third component. In contrast, the V-band variability seems to be linked with stellar activity and HD 102077 has also been classified as BY Draconis by several groups (Udalski & Geyer 1985; Alekseev & Gershberg 1996). Whether HD 102077 is only active or a spectroscopic binary is thus not clear. Further evidence is needed to answer this question.

4.2. Spectral type derivation

From the $i' - z'$ colours we determined an integrated spectral type of K2V. The spectral type determined with spectroscopic means was $K0/1Vp$ (Anders et al. 1991) and is thus one subclass earlier. This deviation is common in a spectral classification based on two colours. We found the individual spectral types to be $K0 \pm 1$ and $K5 \pm 1$ which are in agreement with $K0/1V$ and $K5V$ derived by Cutispoto (1998). This classification seems to be more reliable than the K4 and K2 determined by Fabricius & Makarov (2000) since the brighter primary star is expected to have the earlier spectral type unless the companion is a white dwarf. We note that the errors of the two spectral types are correlated. An earlier spectral type of the primary star implies a later type for the secondary.

4.3. Revisiting the HIPPARCOS data for HD 102077

In the original version of the HIPPARCOS Catalog (ESA 1997) the dataset of HD 102077 = HIP 57269 was solved as a two-component system, with identical proper motions and parallaxes. The separation and position angle are given in Table 1 and have been included in the visual orbital fit; the absolute astrometry given for HIP 57269 in the main HIPPARCOS Catalog corresponds to component A. The solution quality is grade "A", indicating the highest possible quality.

The two components of the system have been recognized separately in the HIPPARCOS raw data via a deviation from the distribution of photon count rate as a function of time from the distribution expected for a single star. For these component systems in the original HIPPARCOS Catalog, the intermediate astrometric data are hard to interpret, since the reference point for the data is not known a priori because it is a complicated function of the photometric and geometric characteristics of the system, and is different for the two data reduction consortia FAST and NDAC.

In the version of the HIPPARCOS Catalog by van Leeuwen & Evans (1997), the system was recognized as a double star, but again solved with the standard five astrometric parameter model; the astrometry given in the catalog seems to refer to component A, just as in the original version of the HIPPARCOS Catalog. Our goal is to re-interpret the HIPPARCOS Intermediate Astrometric Data, taking the orbital solution derived in the present paper into account, and thereby revising the standard astrometric parameters and in particular the parallax.

Table 3. Summary of photometric and spectroscopic results.

Property	Value
Spectral type primary	$K0 \pm 1$
Spectral type secondary	$K5 \pm 1$
Photometric period	none significant
Isochrone age (Myr)	>25
Lithium age (Myr)	<120
Mean radial velocity (km s^{-1})	17.6 ± 2
$\mu_\alpha * \cos\delta$ (mas/yr)	-137.84 ± 1.26
μ_δ (mas/yr)	-33.53 ± 1.45

We used the Hipparcos Intermediate Astrometric Data (abscissae) from van Leeuwen (2007) and fitted corrections to the standard five astrometric parameters (positions and proper motions in right ascension and declination, respectively, and the trigonometric parallax). Before the fitting, we corrected the abscissae for orbital motion, with the orbital parameters given in Table 2. Since the Hipparcos data are absolute astrometric measurements, the reference point for the orbital motion is the centre of mass of the system, against which both components are seen to be moving. In order to derive the centre of mass of the system, we used mass estimates of 0.9 $M_\odot$ for the primary and 0.7 $M_\odot$ for the secondary.

As expected, the largest adjustment occurs in the proper motions when the orbit is taken into account in the analysis of the Hipparcos data. This is because the Hipparcos measurements are spread out over approximately three years, whereas the orbital period is more than a factor of 10 larger, so that the orbital phase coverage of the Hipparcos measurements is relatively small. Thus, some orbital motion has been presumably subsumed into the proper motions before, whereas the corrected proper motions should be free of orbital motion. The new proper motions are $\mu_\alpha * \cos\delta = -137.84 \pm 1.26$ mas yr^{-1} and $\mu_\delta = -33.53 \pm 1.45$ mas yr^{-1}; we reassess the kinematic membership of HD 102077 to a moving group on the basis of these new proper motions in Sect. 4.4. The parallax of HD 102077 of 20.59 ± 2.14 mas, however, does not change at all when the orbit is taken into account in the fitting of the Hipparcos abscissae.

We caution that we might have misinterpreted the reference point of the Hipparcos Intermediate Astrometric Data, which would render our newly derived proper motions meaningless. However, we have verified that the parallax result is very robust and does not change at all even if we assume other reference points. So we conclude that the published Hipparcos parallax is correct even in the case of orbital motion.

4.4. Moving group membership

The source HD 102077 was proposed as candidate member of TW Hydrae (Makarov & Fabricius 2001). However, objections have been raised based on the space motion and weaker-than-expected lithium absorption (Song et al. 2002; König et al. 2003). We now revisit both points.

Our new, high-resolution measurements of the Li EW confirm the lithium absorption value and the comparison of our data to stellar isochrones also suggests a higher age of HD 102077 than is predicted for TW Hydrae.

Anders et al. (1991) measured the radial velocity of HD 102077 in July 1987 and König et al. (2003) in January 2002; we measured the radial velocity in July 2013. The results are 15.9 km s^{-1}, 19 ± 3 km s^{-1}, and 19.8 ± 0.1 km s^{-1} respectively. Another RV-measurement was done by Nordström et al. (2004) who find 16.8 ± 0.3 km s^{-1}, but they do not give the epoch. These radial velocity values do not take the orbital motion into account. According to our orbit fit the relative motion of both components was 3.8 km s^{-1} in July 1987, 0.6 km s^{-1} in January 2002, and 5.0 km s^{-1} in July 2013. As in Sect. 3.2.2 we adopt a maximum uncertainty of half the relative motion (e.g. 1.9 km s^{-1} for 1987). For the measurement by Nordström et al. (2004) we assume an uncertainty of 2 km s^{-1}. The weighted mean of this values gives 17.6 ± 2 km s^{-1}.

This RV value together with the newly derived proper motion can be used to calculate the space velocity as well as the kinematic membership likelihood. We derive *UVWXYZ* Galactic velocities and positions of the binary to be $U = -18.9 \pm 1.1$ km s^{-1}, $V = -29.7 \pm 2.5$ km s^{-1}, and $W = -11.7 \pm 2.9$ km s^{-1}, as well as $X = 17.7 \pm 1.4$ pc, $Y = -44.0 \pm 2.4$ pc, and $Z = 10.1 \pm 2.3$ pc and compare these values to those of TWA ($U = -9.9 \pm 4.2$ km s^{-1}, $V = -18.1 \pm 1.4$ km s^{-1}, $W = -4.5 \pm 2.8$ km s^{-1}, and $X = 12.5 \pm 7.1$ pc, $Y = -42.3 \pm 7.3$ pc, $Z = 21.6 \pm 4.2$ pc; Malo et al. 2013). We find that even though the Galactic position of HD 102077 is close to most of the TW Hydrae members its space motion is different. The space motion of HD 102077 also does not fit other young associations (see Fig. 6). To calculate the moving group membership probability quantitatively we use BANYAN II (Bayesian Analysis for Nearby Young AssociatioNs II) (Malo et al. 2013; Gagné et al. 2014) and find a probability of 0.4% of HD 102077 being a member of TWA. Even if the true parallax value happens to be outside of its 3σ confidence region, the kinematic membership probability does not get higher than 10%. Together with the estimated age this strongly suggests that HD 102077 is not a member of TWA. The probability of HD 102077 being a member of another young moving group is only non-zero for AB Doradus. With the newly derived system parameters it is about 0.03% and it is thus unlikely even though the age of the binary system matches the age of this moving group better. HD 102077 is most likely a member of the young Galactic field.

5. Summary

Our photometric and spectroscopic measurements made it possible to study various aspects of the young, late type binary HD 102077. We present a new, amended orbit fit with small uncertainties on the orbital elements. Using the revised Hipparcos parallax, we deduce a total system mass of 2.6 ± 0.8 $M_\odot$ which leaves the possibility of HD 102077 having a third, close companion. Further evidence for this hypothesis was found in the 2D cross correlation function of the two high-resolution spectra of HD 102077. They show a large radial velocity difference that is in disagreement with the orbital fit, but which could be caused by a third component. In addition, HD 102077 probably has a wider companion at about 400 AU. We also use the derived orbit to revise the kinematics of the system. We find a proper motion of $\mu_\alpha * \cos\delta = -137.84 \pm 1.26$ mas yr^{-1} and $\mu_\delta = -33.53 \pm 1.45$ mas yr^{-1}, as well as a radial velocity of 17.6 ± 2 km s^{-1}.

From the $i'-z'$ colours we determine the spectral type of both components to be $K0 \pm 1$ and $K5 \pm 1$, respectively. We then use this result together with the individual Tycho B_T and V_T colours to estimate an age of the system. We find that HD 102077 is very likely older than 25 Myr, which is in agreement with the lithium EW of 200 ± 4 mÅ and with the absence of circumstellar material. Our results are summarized in Tables 2 and 3.

With the amended kinematic data and the age estimate, we deduce the probability of HD 102077 being a member of one of the young moving groups and find no match. Even

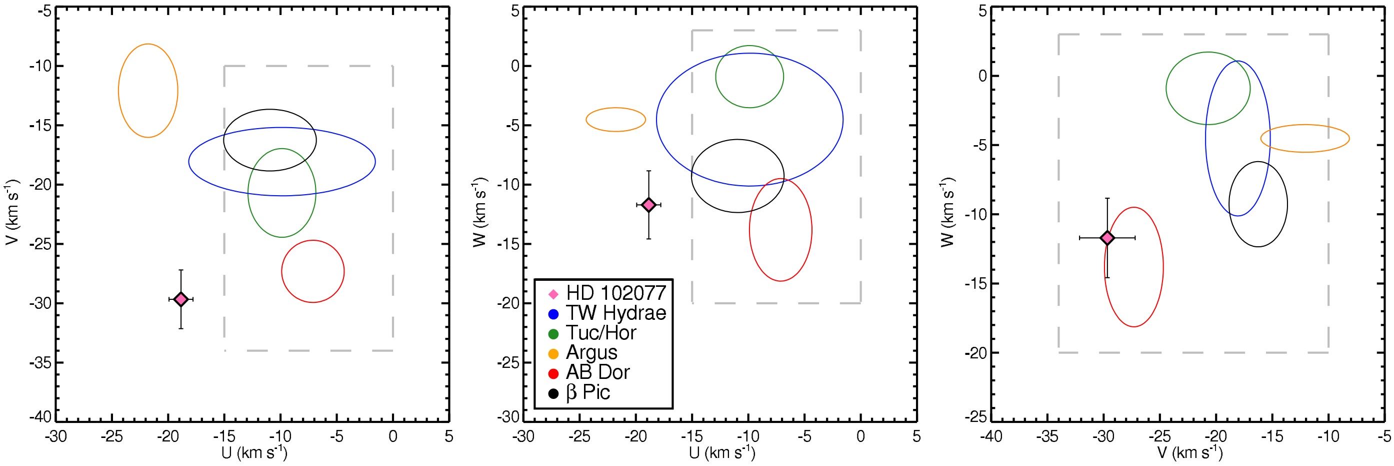

Fig. 6. 2D projections of the *UVW* space velocities compared to well known moving groups, including TWA. The dashed grey box is taken from Zuckerman & Song (2004) and shows the region of *UVW* space typically occupied by nearby young stars. The *UVW* velocities of the young moving groups are taken from Malo et al. (2013), the 2σ uncertainties are plotted. HD 102077 is clearly not a member of any of these groups.

the proposed candidate membership of HD 102077 to the TW Hydrae Association is very unlikely.

For future investigation it would be interesting to study the radial velocity orbit of HD 102077 to clearly answer the question whether the system contains a third component.

Acknowledgements. We thank the staff at La Silla observatory for their support as well as Carolina Bergfors for observing 3 epochs of HD 102077 and Felix Hormuth for his help with the analysis of the Lucky Imaging data. In addition, we thank Chad Bender for sharing his 2D cross-correlation code.

References

Alekseev, I. Y., & Gershberg, R. E. 1996, Astrophysics, 39, 33
Anders, G. J., Coates, D. W., Thompson, K., & Innis, J. L. 1991, MNRAS, 252, 408
Baraffe, I., & Chabrier, G. 2010, A&A, 521, A44
Bertout, C., Basri, G., & Bouvier, J. 1988, ApJ, 330, 350
Bessell, M. S. 2000, PASP, 112, 961
Casagrande, L., Schoenrich, R., Asplund, M., et al. 2011, VizieR Online Data Catalog, J/A+A/530/A138
Cutispoto, G. 1990, A&AS, 84, 397
Cutispoto, G. 1993, A&AS, 102, 655
Cutispoto, G. 1998, A&AS, 131, 321
Cutri, R. M., et al. 2012, VizieR Online Data Catalog: II/311
ESA 1997, VizieR Online Data Catalog: I/239
Fabricius, C., & Makarov, V. V. 2000, A&A, 356, 141
Fruchter, A. S., & Hook, R. N. 2002, PASP, 114, 144
Gagné, J., Lafrenière, D., Doyon, R., Malo, L., & Artigau, É. 2014, ApJ, in press [`arXiv:1312.5864`]
Gregorio-Hetem, J., Lepine, J. R. D., Quast, G. R., Torres, C. A. O., & de La Reza, R. 1992, AJ, 103, 549
Gurzadian, G. A., & Cholakian, V. G. 1992, Ap&SS, 188, 205
Hartkopf, W. I., Mason, B. D., Barry, D. J., et al. 1993, AJ, 106, 352
Hartkopf, W. I., Tokovinin, A., & Mason, B. D. 2012, AJ, 143, 42
Heintz, W. D. 1986, A&AS, 65, 411
Hippler, S., Bergfors, C., Brandner Wolfgang, et al. 2009, The Messenger, 137, 14
Hofmann, R., Blietz, M., Duhoux, P., et al. 1992, ESO Conf. Workshop Proc., 42, 617
Holden, F. 1965, Publications of Michigan Observatory, 9, 181
Holmberg, J., Nordström, B., & Andersen, J. 2007, A&A, 475, 519
Hormuth, F., Brandner, W., Hippler, S., & Henning, T. 2008, J. Phys. Conf. Ser., 131, 012051
Kastner, J. H., Zuckerman, B., Weintraub, D. A., & Forveille, T. 1997, Science, 277, 67
Kaufer, A., & Pasquini, L. 1998, Proc. SPIE, 3355, 844
Kenyon, S. J., & Hartmann, L. 1987, ApJ, 323, 714
Köhler, R., Ratzka, T., Herbst, T. M., & Kasper, M. 2008, A&A, 482, 929
König, B., Neuhäuser, R., Guenther, E. W., & Hambaryan, V. 2003, Astron. Nachr., 324, 516
Kovács, G., Zucker, S., & Mazeh, T. 2002, A&A, 391, 369
Kraus, A. L., & Hillenbrand, L. A. 2007, AJ, 134, 2340
Lynden-Bell, D., & Pringle, J. E. 1974, MNRAS, 168, 603
Makarov, V. V. 2003, AJ, 126, 1996
Makarov, V. V., & Fabricius, C. 2001, A&A, 368, 866
Malo, L., Doyon, R., Lafrenière, D., et al. 2013, ApJ, 762, 88
Mason, B. D., Wycoff, G. L., Hartkopf, W. I., Douglass, G. G., & Worley, C. E. 2011, VizieR Online Data Catalog, B/wds
Mazeh, T., Prato, L., Simon, M., et al. 2002, ApJ, 564, 1007
McAlister, H., Hartkopf, W. I., & Franz, O. G. 1990, AJ, 99, 965
Moór, A., Szabó, G. M., Kiss, L. L., et al. 2013, MNRAS, 435, 1376
Müller, A., Roccatagliata, V., Henning, T., et al. 2013, A&A, 556, A3
Nordström, B., Mayor, M., Andersen, J., et al. 2004, A&A, 418, 989
Olsen, E. H. 1994, A&AS, 104, 429
Pallavicini, R., Randich, S., & Giampapa, M. S. 1992, A&A, 253, 185
Plavchan, P., Jura, M., Kirkpatrick, J. D., Cutri, R. M., & Gallagher, S. C. 2008, ApJS, 175, 191
Randich, S., Gratton, R., & Pallavicini, R. 1993, A&A, 273, 194
Rochau, B., Brandner, W., Stolte, A., et al. 2010, ApJ, 716, L90
Rodriguez, D. R., Zuckerman, B., Kastner, J. H., et al. 2013, ApJ, 774, 101
Rossiter, R. A. 1955, Publications of Michigan Observatory, 11, 1
Rousset, G., Beuzit, J.-L., Hubin, N., et al. 1994, Proc. SPIE, 2201, 1088
Schlieder, J. E., Lépine, S., & Simon, M. 2010, AJ, 140, 119
Schlieder, J. E., Lépine, S., & Simon, M. 2012a, AJ, 143, 80
Schlieder, J. E., Lépine, S., & Simon, M. 2012b, AJ, 144, 109
Shkolnik, E. L., Anglada-Escudé, G., Liu, M. C., et al. 2012, ApJ, 758, 56
Song, I., Bessell, M. S., & Zuckerman, B. 2002, A&A, 385, 862
Thomann, C., James, D. J., Boberg, O. M., Cargile, P., & Aarnio, A. 2013, AAS Meeting Abstracts, 221, 250.29
Tognelli, E., Prada Moroni, P. G., & Degl'Innocenti, S. 2011, A&A, 533, A109
Tokovinin, A., Mason, B. D., & Hartkopf, W. I. 2010, AJ, 139, 743
Torres, C. A. O., Quast, G. R., Melo, C. H. F., & Sterzik, M. F. 2008, Handbook of Star Forming Regions, vol. II, 757
Udalski, A., & Geyer, E. H. 1985, IBVS, 2691, 1
Valenti, J. A., & Piskunov, N. 1996, A&AS, 118, 595
van Dessel, E., & Sinachopoulos, D. 1993, A&AS, 100, 517
van Leeuwen, F. 2007, A&A, 474, 653
van Leeuwen, F., & Evans, D. W. 1997, VizieR Online Data Catalog, J/A+AS/130/157
Voigt, H.-H. 1988, Abriß der Astronomie, 4. völlig neu bearbeitete Auflage (Mannheim, F.R. Germany: BI-Wissenschaftsverlag)
Wallerstein, G., & Conti, P. S. 1969, ARA&A, 7, 99
Weiler, E. J., & Stencel, R. E. 1979, AJ, 84, 1372
Weinberger, A. J., Anglada-Escudé, G., & Boss, A. P. 2013, ApJ, 762, 118
Weise, P., Launhardt, R., Setiawan, J., & Henning, T. 2010, A&A, 517, A88
Worley, C. E. 1978, Publications of the U.S. Naval Observatory Second Series, 24, 1
Zechmeister, M., & Kürster, M. 2009, A&A, 496, 577
Zuckerman, B., & Song, I. 2004, ARA&A, 42, 685
Zuckerman, B., Rhee, J. H., Song, I., & Bessell, M. S. 2011, ApJ, 732, 61

5

Discussion

In Chapter 2 and Chapter 3 we describe, what sources we found during our Lucky Imaging observations of transiting exoplanet host stars. We discuss how many background sources we expect for the survey based on the density of background sources around each target. The next step is to understand for each detected source, whether the detected companion candidate is a member of the exoplanet system. The best way of doing that is to monitor the orbital motion of the two stellar components around each other as we have done for the binary star HD 102077 (see Section 4.3.1). The companions that we detected around the transiting exoplanet host stars are, however, usually separated by several hundred AU and thus the orbital motion is not detectable during the time span that those targets were observed. The common way to overcome this problem is to analyse, whether both stars share common proper motion and whether their photometric distances are alike. If both are true, physical companionship is very likely, but not certain. In the following, I discuss the proper motion of the companion candidates of Chapter 2 by using two different statistical approaches. I then discuss whether the detected companions around exoplanet host stars have the same occurrence rate as field stars and I compare the companion fraction of exoplanet systems with misaligned planetary orbits to those with aligned orbits. Afterwards, I discuss whether Lucky Imaging was a suitable strategy for this project or whether Adaptive Optics observations would have been more beneficial. Finally, I mention a few ideas about projects that could be done in future.

5.1 Proper motion constraints on companion candidates

In our first survey (Chapter 2) we obtained new positional measurements for stellar companions or companion candidates to CoRoT-2, CoRoT-3, HAT-P-7, HAT-P-8, TrES-2, TrES-4, and WASP-2. I used these values and earlier measurements to check for the common proper motion of the companion candidates with the exoplanet host star. The values of the earlier measurements are taken from Daemgen et al. (2009); Narita et al. (2012); Bechter et al. (2014); Bergfors et al. (2013); Faedi et al. (2013); Ginski et al. (2013) and the 2MASS PSC. Note that the discovery papers of the companion candidates to CoRoT-11, HAT-P-41, and KIC 10905746 only give rough position information and no precise separation and position angle. They are thus not considered in the following analysis.

We depict the position changes with time in Figure 5.1. For comparison, these are overplotted with the predicted motion of an unrelated background object at infinity (model A) and a gravitationally bound companion without orbital motion (model B) that best fit the data. The orbital motion is negligible as the projected physical separations between the seven TEPs and companion candidates are in the range of 100 AU to 3500 AU. By assuming that the projected physical separation is identical to the true separation, the combination of separation and system mass identifies WASP-2 as the binary in our sample with the shortest orbital period of about 750 yr. Thus, over the 2050 day time span covered by our analysis, the position angle should have changed at most by 2.7 deg (assuming a circular orbit seen face-on), resulting in a maximum change in ΔRA/ΔDEC of 0.023″. This is smaller than most positional measurement uncertainties. Figure 5.1 shows that the candidate companions of HAT-P-7, HAT-P-8, TrES-4, and WASP-2 clearly share proper motion with the exoplanet host star. For CoRoT-2, CoRoT-3-South and -East, and TrES-2 the interpretation is, however, less clear.

5.1.1 Bayesian model comparison

Quantitatively, the relative probability of model A to model B can be computed by using Bayes theorem given the astrometric position measurements D and the background information I:

$$\underbrace{\frac{\text{prob}(A|D,I)}{\text{prob}(B|D,I)}}_{\text{posterior ratio}} = \underbrace{\frac{\text{prob}(D|A,I)}{\text{prob}(D|B,I)}}_{\text{likelihood ratio}} \times \underbrace{\frac{\text{prob}(A|I)}{\text{prob}(B|I)}}_{\text{prior ratio}} .$$

The priors $\text{prob}(A|I)$ and $\text{prob}(B|I)$ represent our state of knowledge about the truth of the model before the measurement. Since all potential companions have been found in larger surveys where we expect to find a few unrelated background objects, we cannot distinguish between the models beforehand and assume a prior ratio of one.

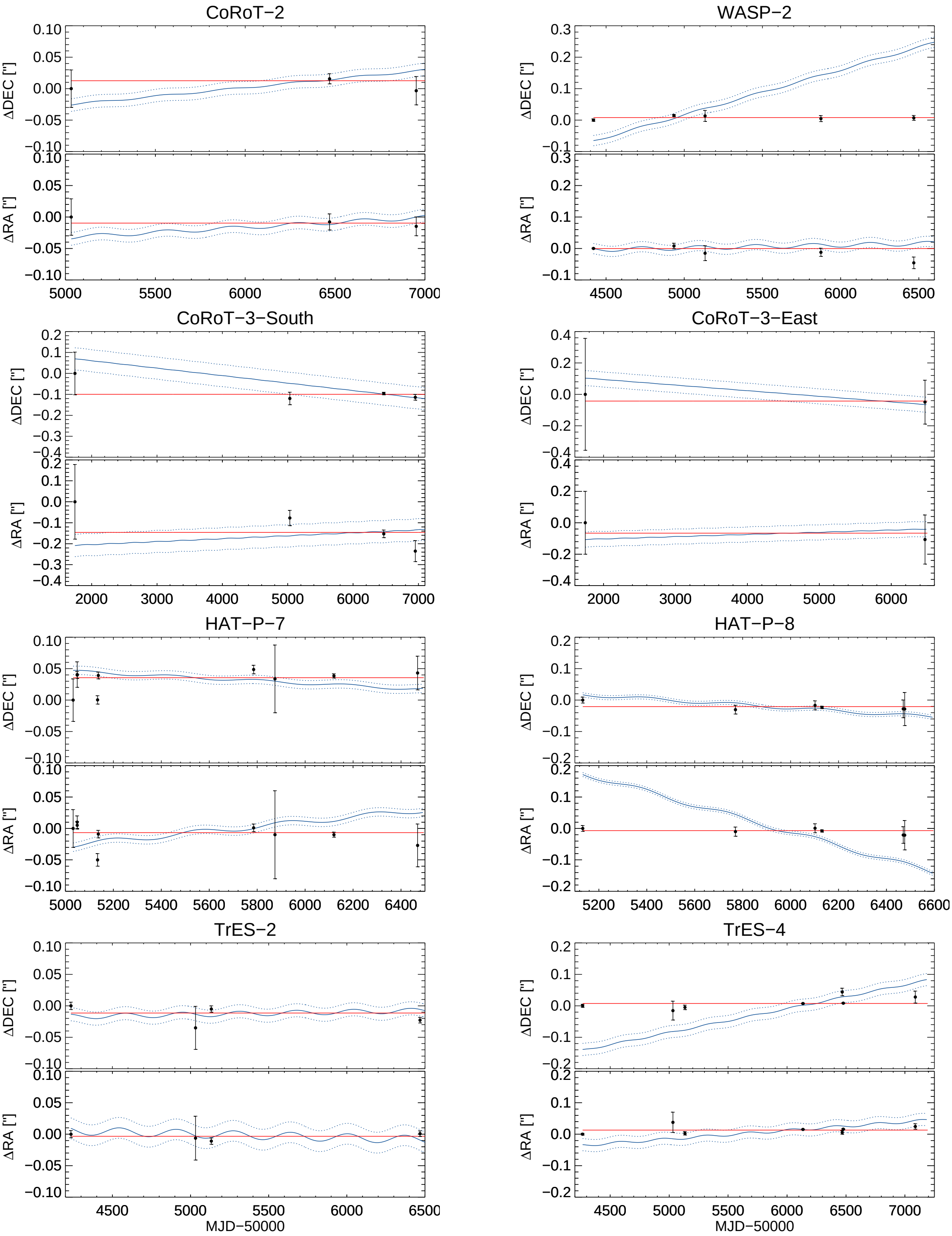

Figure 5.1: The position change measurements of the companion candidates in ΔRA and ΔDEC over time. The red line shows the expected motion of a gravitationally bound companion without orbital motion; the blue line depicts the expected motion of a background star at infinity. The dashed blue lines represent the envelope of the latter model due to the 1σ uncertainties of the proper motion and parallax of the TEP host star.

Table 5.1: Proper motion and parallax values of our follow-up targets. All proper motion measurements are from Röser et al. (2008). The parallaxes, if not otherwise indicated, correspond to the photometric distances that were estimated in Bergfors et al. (2013) from $i - z$ colours. [a]: Deleuil et al. (2008), [b]: Pál et al. (2008).

Name	μ_x [mas/year]	μ_y [mas/year]	parallax [mas]
CoRoT-2	-5.84 ± 1.9	-10.12 ± 1.9	3.35 ± 1.65
CoRoT-3	-15.57 ± 11.6	14.05 ± 11.6	1.50 ± 0.50^a
HAT-P-7	-13.86 ± 1.7	7.19 ± 1.7	3.125 ± 0.45^b
HAT-P-8	78.65 ± 1.7	17.89 ± 1.8	6.65 ± 1.00
TrES-2	2.34 ± 2.7	-1.55 ± 1.7	4.55 ± 0.45
TrES-4	-9.94 ± 2.5	-27.8 ± 2.5	3.45 ± 0.40
WASP-2	-3.38 ± 2.9	-52.31 ± 2.9	7.14 ± 0.55

For the calculation of the likelihood of each model we assume that all N measurements of the relative position of the two components x_i and y_i are uncorrelated and that the uncertainties σ_{xi} and σ_{yi} are Gaussian. The expected position changes Δx_i and Δy_i of an unrelated background object at time t after the first measurement (model A) can be calculated knowing the offset of the position of a star caused by parallactic motion $\mathrm{paroff}_x(t)$ and $\mathrm{paroff}_y(t)$ and the proper motion μ_x and μ_y of the exoplanet host star:

$$\begin{aligned}\Delta x_i &= \mathrm{paroff}_x(t) - \mathrm{paroff}_x(t=0) + \mu_x \cdot t \\ \Delta y_i &= \mathrm{paroff}_y(t) - \mathrm{paroff}_y(t=0) + \mu_y \cdot t.\end{aligned}$$

The expected position change of a gravitationally bound object (model B) is easier to determine since the orbital motion of our targets is negligible. It follows that $\Delta x_i = \Delta y_i = 0$. The true x and y-position of the first epoch measurement is, however, not known and has to be introduced to both models as model parameter λ_x and λ_y. Since we do not know something about the initial true position we assign a uniform prior $\mathrm{prob}(\lambda_x|A,I) = \mathrm{prob}(\lambda_y|A,I) = 1/(\lambda_{\mathrm{max}} - \lambda_{\mathrm{min}}) = 1/\Delta\lambda$ in the range $\lambda_{\mathrm{min}} \leq \lambda_{x,y} \leq \lambda_{\mathrm{max}}$. The likelihood of model A for the x-position measurements can then be calculated by:

$$\begin{aligned}\mathrm{prob}_x(D|A,I) &= \int \mathrm{prob}_x(D,\lambda_x|A,I)\,\mathrm{d}\lambda_x \\ &= \int \mathrm{prob}_x(D|\lambda_x,A,I)\,\mathrm{prob}_x(\lambda_x|A,I)\,\mathrm{d}\lambda_x \\ &= \frac{1}{\Delta\lambda}\int \prod_{i=1}^{N} \frac{1}{\sqrt{2\pi}\sigma_{xi}} \exp\left(-\frac{(x-\Delta x_i-\lambda_x)^2}{2\sigma_{xi}^2}\right)\mathrm{d}\lambda_x\end{aligned}$$

and alike $\mathrm{prob}_y(D|A,I)$. The total likelihood of model A is given by $\mathrm{prob}(D|A,I) = \mathrm{prob}_x(D|A,I) \cdot \mathrm{prob}_y(D|A,I)$. Likewise the likelihood of model B can be determined.

Table 5.2: Relative model probabilities for an unbound (A) vs. a bound system (B).

Star	$\frac{\text{prob(A)}}{\text{prob(B)}}$
CoRoT-2	0.54
CoRoT-3-South	0.06
CoRoT-3-East	0.35
HAT-P-7	$2.3 \cdot 10^{-15}$
HAT-P-8	0.0
TrES-2	1.17
TrES-4	$6.7 \cdot 10^{-17}$
WASP-2	0.0

For model A the influence of the parallax and proper motion uncertainties on the model probability has to be considered. We thus draw 50000 random pairs of parallax and proper motion values from a Gaussian distribution with the given mean and standard deviation from literature; they are listed in Table 5.1. The likelihood of model A is then the average from all combinations.

The calculated relative probabilities can be found in Table 5.2. As expected from the visual inspection of Figure 5.1 the probability of HAT-P-7, HAT-P-8, TrES-4, and WASP-2 being unbound is very small. The two companion candidates of CoRoT-3 are more likely bound than unbound and the companion candidates of CoRoT-2 and TrES-2 are roughly equally likely bound or unbound. For these systems more epochs are needed to decide if they share common proper motion. Note that the common proper motion of HAT-P-7 (Narita et al., 2012), HAT-P-8 (Bechter et al., 2014; Ginski et al., 2013), TrES-4 (Bergfors et al., 2013) and Wasp-2 (Bergfors et al., 2013) was previously stated in the referenced papers. Our results are thus in agreement with their findings. Using more positional measurements Ngo et al. (2015) showed that also the companion candidate of TrES-2 shares common proper motion.

5.1.2 Fitting possible relative space motions

The Bayesian approach compares the likelihood of two options, here an gravitationally bound object versus a background star thought to be at infinity. Obviously, there are many more possibilities: the star could be in the foreground, at approximately the same distance, but unbound or only slightly behind the transiting planet host star from Earth's perspective. Then both stars have measurable proper motions from Earth and their relative proper motion needs to be considered. As the majority of the 2MASS PSC sources still lack proper motion measurements, we used the *galaxia* implementation

(Sharma et al., 2011) of the Besançon *Model of stellar population synthesis of the Galaxy* (Robin et al., 2003) to get a representative view of the stellar properties in the direction of the TEP hosts. Around each of the 7 candidate companions with multiple relative position measurements, we simulated a 1-square degree field using a “warp” and “flared disk”. We only considered stars that are visible with AstraLux using the contrast for each target given in Chapter 2, Table 1. In general, the predicted stellar densities agree with the number count derived from 2MASS PSC (see Section 2.3.2) to within 20%. The range of plausible proper motions of the TEP host companion candidates with respect to the host can be estimated by a linear regression to the measured astrometric positions in RA and DEC. This neglects the difference in parallactic motion which is on the order of the measurement uncertainty for most field stars, e.g. see Fig. 5.1. The slopes of the best fit $\Delta\mu$ are small and $\Delta\mu = 0$, the motion of a bound companion without orbital motion, lies within $3\sigma_{\Delta\mu}$ in all except one case (TrES-2 in DEC). The slope and the standard deviation of the best fit, and the probability for a field star to be both within $6''$ of the TEP and to have a proper motion deviating by less than 3 or $5\sigma_{\Delta\mu}$ from the proper motion of the TEP host can be found in Table 5.3. Fig. 5.2 depicts the distribution of sources and their proper motions around WASP-2 and TrES-2 as an example. For the companion candidates CoRoT-2, CoRoT-3S, and CoRoT-3E the accuracy of the relative astrometry is still too coarse, resulting in a 17% to 33% chance for the companion candidate to be an unrelated field star. For the other companion candidates the resulting probabilities are small to negligible ($< 1.7\%$), thus there is a high probability for them to be a physical companion. This is in accordance with the result of the Bayesian analysis above.

Table 5.3: Probabilities $\overline{P_i(0)}$ for companion candidates with multi-epoch relative astrometry to be unrelated field objects. We used a linear regression to fit the multi-epoch relative astrometry, and 3 resp. 5 sigma upper limits on the uncertainty of the slope $\Delta\mu$ to compute the number of field objects with matching proper motions. All velocities are given in mas/year.

Name	$\Delta\mu RA$	$\sigma_{\Delta\mu RA}$	$\Delta\mu DEC$	$\sigma_{\Delta\mu DEC}$	$\overline{P_i(0)_{3\sigma}}$	$\overline{P_i(0)_{5\sigma}}$
CoRoT-2	-2.0	8.0	4.0	7.8	$1.7 \cdot 10^{-1}$	$1.7 \cdot 10^{-1}$
CoRoT-3S	-17	20	-4	30	$3.3 \cdot 10^{-1}$	$3.3 \cdot 10^{-1}$
CoRoT-3E	-16.6	8.5	-0.7	5.6	$3.0 \cdot 10^{-1}$	$3.3 \cdot 10^{-1}$
HAT-P-7	-1.2	1.9	3.2	1.6	$2.2 \cdot 10^{-4}$	$1.3 \cdot 10^{-3}$
HAT-P-8	-2.9	3.5	-7.7	3.6	$< 10^{-5}$	$< 10^{-5}$
TrES-2	0.7	1.1	-3.9	1.2	$8.0 \cdot 10^{-3}$	$1.7 \cdot 10^{-2}$
TrES-4	1.2	1.9	3.6	2.4	$< 10^{-5}$	$1.7 \cdot 10^{-5}$
WASP-2	-4.4	2.2	1.2	1.4	$< 10^{-5}$	$< 10^{-5}$

In the near future, the Gaia space observatory will deliver a space catalogue of approximately one billion stars brighter than 20 magnitudes in the passband between 400 nm

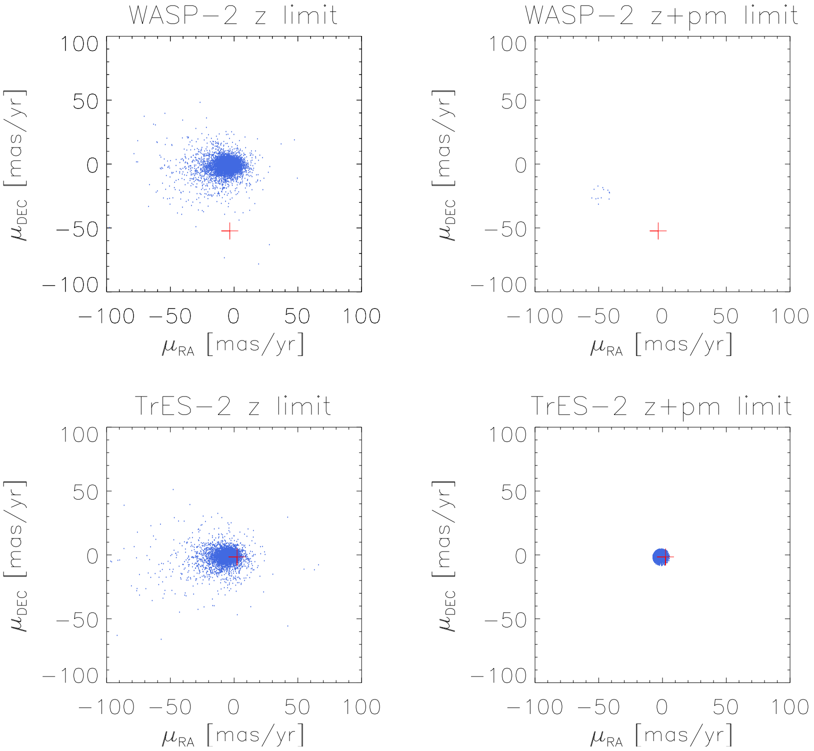

Figure 5.2: The plot shows the proper motion μ_{RA} and μ_{DEC} of starss within 1 deg^2 to WASP-2 and TrES-2 according to the *galaxia* implementation of the Besançon *Model of stellar population synthesis of the Galaxy*. The left plots include all stars that are bright enough to be detectable during our observation of the exoplanet host star, the right plots only include those stars that are both bright enough and that have a proper motion that is in accordance with the multiple positional measurements of the companion candidate. The red plus sign indicates the proper motion of the exoplanet host star itself.

and 1000 nm. This will allow to do the above analysis with real and improved measurements of the parallax and proper motion of each exoplanet host star and its surrounding stellar sources.

5.2 Companion fraction and spin-orbit angle

The presence of a stellar companion is one possible cause for a misaligned spin-orbit angle (see Section 1.1.3). In the following I will discuss whether binarity of the TEP host star correlates with the spin-orbit alignment of its planet. The analysis is based on the Lucky Imaging surveys of Daemgen et al. (2009); Bergfors et al. (2013); Faedi et al. (2013); Ginski et al. (2012, 2013, 2015); Guenther et al. (2013) in addition to our work to enlarge the sample size of planets for which the Rossiter-McLaughlin effect has been measured and to reduce the selection bias due to multiple observations of the same TEP host stars. All these surveys have similar contrast curves.

Altogether, 62 systems have been observed, whereof 20 planets have misaligned orbits, and 42 planets are consistent with a well-aligned circular orbit (see Table 5.4). Note in this context misaligned planets means that the spin-orbit angle is more than 3σ away from zero. Around 20 of these systems a companion candidate was detected; 12 of them have been shown to share proper motion (HAT-P-7, HAT-P-8, HAT-P-24, HAT-P-30, HAT-P-32, Kepler-13, TrES-2, TrES-4, WASP-2, WASP-11, WASP-12, WASP-14) whereas the other 8 systems do not have enough/precise enough measurements to decide on the common proper motion with the close exoplanet host star (CoRoT-2, CoRoT-3, CoRoT-11, HAT-P-18, HAT-P-27, TrES-1, WASP-33, XO-3). To calculate the companion fraction, we have to estimate the number of true companions. In Section 2.3.2 we showed that the average probability of finding an unrelated field star was 4.7% for our first survey. Assuming that this is a reasonable estimate for all surveys and that the detections follow a Poisson distribution we expect 2.9 ± 1.7 unrelated stars for the observed 62 targets. This gives thus 17.1 ± 1.7 bound sources and it yields a raw companion fraction of $28\% \pm 7\%$.

The true companion fraction is higher since mid to late M-dwarf companions are to faint to be detected with Lucky Imaging and also the brighter stars may only be detectable for part of their orbit depending on their orbital elements. To roughly estimate the number of companions that we missed, I use the contrast curve from Chapter 2, Fig. 2, the distance and spectral type distribution of our targets given in Fig. 1.6, and the spectral type conversion table from Kraus & Hillenbrand (2007). It follows that for G-type stars (the main spectral type of our targets), we are able to detect sources with absolute z'-band magnitudes of 9 mag-10 mag, corresponding to M4 companions. These stars have a mass of about $0.2\,\mathrm{M}_{\odot}$. Using the binary mass ratio distribution from Raghavan et al. (2010), it follows that we miss about 10% of the companion stars. This gives a corrected companion frequency of about $31\% \pm 7\%$. Solar type field stars on the other hand have a total multiplicity rate of $44 \pm 2\%$ (Raghavan et al., 2010). When we only consider targets with physical separations between 50 AU to 2000 AU to which Lucky Imaging observations are sensitive, the companion fraction goes down to $24\% \pm 1\%$ using the sources given in Raghavan et al. (2010). This value is in agreement with the multiplicity fraction found by us, but our uncertainties are large. Our result suggests that binarity does not hinder the formation of hot Jupiter systems and that hot Jupiters may even form more commonly in multiple stellar systems than around single stars.

Fig. 5.3 shows the projected spin-orbit angle versus the effective stellar temperature and indicates which targets have companion candidates and which do not. 6 out of the 20 misaligned systems have a common proper motion companion. Another 3 targets have a companion candidate. In the aligned sample of 42 stars, 6 plus potentially 5 systems have a bound stellar companion. On the first view, it seems that misaligned systems have slightly more stellar companions, but the uncertainties are large and thus no final conclusion can be drawn. Due to the fact that many hot Jupiter systems with misaligned orbits do not seem to have stellar companions (if they are not hidden within $< 0.1''$ or outside of $6''$), it is likely that the presence of stellar companions and thus the Lidov-Kozai mechanism (Davies et al., 2014) and the resonance between the binary and planetary orbit (Touma & Sridhar, 2015) are not the only ways to produce tilted orbits. As stated in Section 1.1.3 other plausible reasons are the primordial misalignment of the protoplanetary disk (Lai et al., 2011; Batygin, 2012) or planet-planet scattering (Ford & Rasio, 2008).

Fig. 5.3 also shows the projected separation of the detected sources. Most of the companions/companion candidates are at least several hundred AU away from the exoplanet host star. The distance distribution of field stars on the other hand peaks at around 50 AU (see Fig. 1.3) which corresponds to $0.1''$-$0.5''$ for most of our targets. At that separation, we are able to detect stellar companions down to early M-dwarfs. Finding only a few close sources may indicate that the binary companions of hot Jupiter systems are on average more separated than field stars. For a precise analysis, better parallaxes and estimates of the true separation as well as observations of more targets are needed.

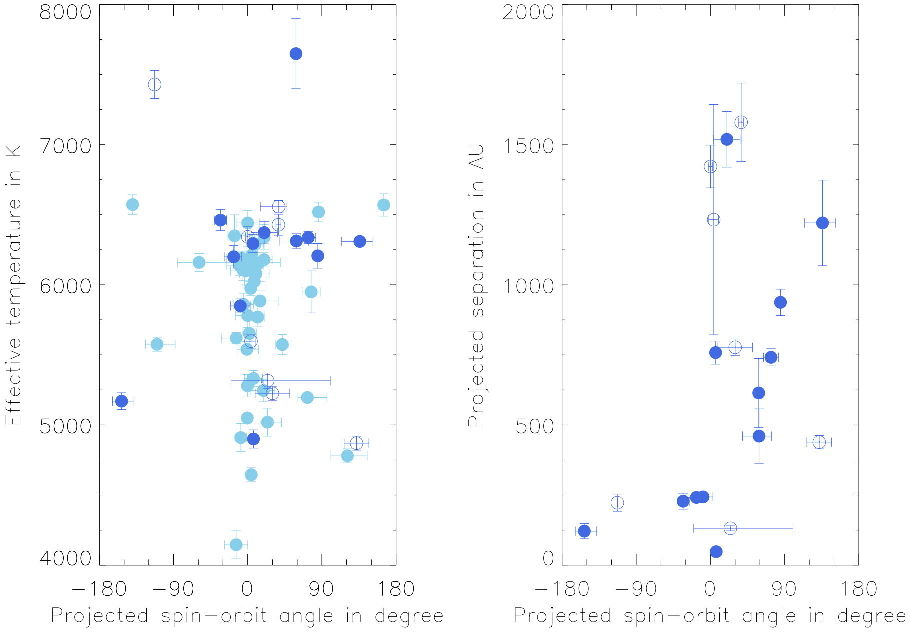

Figure 5.3: So far, 62 transiting exoplanet host stars with λ-measurements have been observed with Lucky Imaging. Left: λ versus T_{eff} is shown. Targets without detected companion are depicted with filled, light blue circles, targets with a common proper motion companion with filled, dark blue symbols, and targets with companion candidates with open, dark blue circles. Right: λ versus the projected separation of the companions/companion candidates is shown.

Table 5.4: Targets with λ-measurements that have been observed by Lucky Imaging. The Table indicates the names, the measured spin-orbit angle (from TepCat), if they have a detected companion candidate and if it is common proper motion, and the references to the positional measurements.

Name	Lambda [°]	CC?	cpm	ref
55 Cnc e	$72.4^{+23.7}_{-11.5}$	no		Wöllert & Brandner (2015)
CoRoT-01	$77.0^{+11.0}_{-11.0}$	no		Wöllert & Brandner (2015)
CoRoT-02	$4.0^{+5.9}_{-6.1}$	yes		Faedi et al. (2013); Wöllert et al. (2015); Wöllert & Brandner (2015)
CoRoT-03	$37.6^{+10.0}_{-22.3}$	yes		Faedi et al. (2013); Wöllert et al. (2015); Wöllert & Brandner (2015)
CoRoT-11	$0.10^{+2.6}_{-2.6}$	yes		Wöllert et al. (2015); Wöllert & Brandner (2015)
HAT-P-01	$-10.0^{+20.0}_{-20.0}$	no		Daemgen et al. (2009)
HAT-P-02	$-52.0^{+27.0}_{-22.0}$	no		Bergfors et al. (2013)
HAT-P-04	$3.7^{+2.1}_{-2.1}$	no		Wöllert et al. (2015)
HAT-P-06	$9.0^{+10.0}_{-10.0}$	no		Daemgen et al. (2009)
HAT-P-07	$-4.9^{+11.9}_{-11.9}$	yes	yes	Faedi et al. (2013); Bergfors et al. (2013); Narita et al. (2010); Wöllert et al. (2015)
HAT-P-08	$165.0^{+6.0}_{-6.0}$	yes	yes	Bergfors et al. (2013); Ginski et al. (2013); Bechter et al. (2014); Wöllert et al. (2015)
HAT-P-09	$136.0^{+16.0}_{-22.0}$	no		Wöllert & Brandner (2015)
HAT-P-11	$-17.0^{+9.2}_{-11.5}$	no		Bergfors et al. (2013)
HAT-P-13	$-16.0^{+8.0}_{-8.0}$	no		Bergfors et al. (2013)
HAT-P-14	$121.0^{+24.0}_{-21.0}$	no		Wöllert et al. (2015)
HAT-P-16	$1.90^{+8.6}_{-8.6}$	no		Wöllert et al. (2015)
HAT-P-17	$189.1^{+5.1}_{-5.1}$	no		Wöllert et al. (2015)
HAT-P-18	$-10.0^{+16.0}_{-16.0}$	yes		Ginski et al. (2015)
HAT-P-23	$19.0^{+14.0}_{-16.0}$	no		Wöllert et al. (2015)
HAT-P-24	$132.0^{+15.0}_{-15.0}$	yes	yes	Ngo et al. (2015); Wöllert & Brandner (2015)
HAT-P-27	$15.0^{+22.0}_{-22.0}$	yes		Wöllert & Brandner (2015)
HAT-P-30	$20.0^{+16.0}_{-16.0}$	yes	yes	Ginski et al. (2013); Ngo et al. (2015); Wöllert et al. (2015)
HAT-P-32	$24.2^{+76.0}_{-44.5}$	yes	yes	Ngo et al. (2015); Wöllert & Brandner (2015)
HAT-P-34	$73.5^{+9.0}_{-9.0}$	no		Wöllert et al. (2015)
HAT-P-36	$85.0^{+1.5}_{-1.5}$	no		Wöllert et al. (2015)
HD 017156	$0.0^{+14.0}_{-14.0}$	no		Daemgen et al. (2009)
HD 080606	$-14.0^{+18.0}_{-18.0}$	no		Bergfors et al. (2013)
HD 149026	$8.0^{+8.0}_{-8.0}$	no		Bergfors et al. (2013)

HD 189733	$3.0^{+25.0}_{-25.0}$	no		Daemgen et al. (2009)
HD 209458	$10.0^{+5.1}_{-5.1}$	no		Daemgen et al. (2009)
Kepler-08	$42.0^{+8.0}_{-8.0}$	no		Wöllert et al. (2015)
Kepler-13	$12.0^{+7.0}_{-7.0}$	yes	yes	Wöllert & Brandner (2015)
Kepler-17	$-0.5^{+0.3}_{-0.3}$	no		Wöllert et al. (2015)
Kepler-63	$-5.0^{+7.0}_{-7.0}$	no		Wöllert & Brandner (2015)
Qatar-1	$2.0^{+16.0}_{-16.0}$	no		Wöllert et al. (2015)
Qatar-2	$-36.0^{+11.0}_{-11.0}$	no		Wöllert & Brandner (2015)
TrES-1	$9.7^{+5.2}_{-5.2}$	yes		Faedi et al. (2013)
TrES-2	$5.0^{+7.0}_{-7.0}$	yes	yes	Daemgen et al. (2009); Faedi et al. (2013); Bergfors et al. (2013); Wöllert et al. (2015); Ngo et al. (2015)
TrES-4	$58.6^{+2.0}_{-2.0}$	yes	yes	Daemgen et al. (2009); Faedi et al. (2013) Bergfors et al. (2013); Wöllert & Brandner (2015); Ngo et al. (2015)
WASP-01	$0.0^{+15.0}_{-15.0}$	no		Daemgen et al. (2009)
WASP-02	$9.4^{+7.1}_{-7.1}$	yes	yes	Daemgen et al. (2009); Bergfors et al. (2013); Ngo et al. (2015); Wöllert et al. (2015)
WASP-03	$-1.0^{+10.0}_{-10.0}$	no		Bergfors et al. (2013)
WASP-04	$-110.0^{+22.0}_{-14.0}$	no		Bergfors et al. (2013)
WASP-05	$-11.0^{+11.0}_{-11.0}$	no		Bergfors et al. (2013)
WASP-07	$74.0^{+32.0}_{-46.0}$	no		Bergfors et al. (2013)
WASP-11	$12.6^{+3.0}_{-2.9}$	yes	yes	Ngo et al. (2015); Wöllert & Brandner (2015)
WASP-12	$-8.4^{+7.1}_{-7.1}$	yes	yes	Bergfors et al. (2013); Ngo et al. (2015); Bechter et al. (2014); Wöllert & Brandner (2015)
WASP-13	$4.3^{+4.5}_{-4.5}$	no		Bergfors et al. (2013)
WASP-14	$30.0^{+21.0}_{-21.0}$	yes	yes	Ngo et al. (2015); Wöllert et al. (2015); Wöllert & Brandner (2015)
WASP-15	$-9.0^{+12.0}_{-12.0}$	no		Bergfors et al. (2013)
WASP-24	$6.3^{+4.7}_{-4.7}$	no		Wöllert et al. (2015)
WASP-28	$-59.0^{+99.0}_{-26.0}$	no		Wöllert et al. (2015)
WASP-30	$-153.^{+15.0}_{-11.0}$	no		Wöllert & Brandner (2015)
WASP-32	$20.0^{+3.30}_{-3.30}$	no		Wöllert & Brandner (2015)
WASP-33	$-1.0^{+14.0}_{-12.0}$	yes		Moya et al. (2011); Adams et al. (2013); Wöllert & Brandner (2015)
WASP-38	$12.1^{+8.00}_{-10.0}$	no		Wöllert et al. (2015)
WASP-52	$7.2^{+3.7}_{-3.7}$	no		Wöllert et al. (2015)
WASP-71	$86.0^{+6.0}_{-6.0}$	no		Wöllert & Brandner (2015)
WASP-80	$-123.3^{+3.4}_{-4.4}$	no		Wöllert et al. (2015)

WASP-84	$7.0^{+5.0}_{-5.0}$	no	Wöllert & Brandner (2015)
XO-2	$59.0^{+15.0}_{-20.0}$	no	Daemgen et al. (2009)
XO-3	$8.0^{+13.0}_{-12.0}$	yes	Bergfors et al. (2013); Wöllert & Brandner (2015)

Ngo et al. (2015) made a similar survey and observed 50 targets with spin-orbit angle measurements using Keck NIRC2. In contrast to us, they do not find differences in the companion fraction between aligned ($51\% \pm 13\%$) and misaligned ($48\% \pm 12\%$) hot Jupiter systems. Their companion fraction is higher then the value found by us. This may indicate that we underestimate the number of targets that we are not able to detect.

It should be noted that λ is only the projection of the spin-orbit angle Ψ onto the celestial sphere and thus some of the seemingly aligned systems could be misaligned. The true spin-orbit angle can, however, be measured using star spots or gravity darkening (see Section 1.1.3). In addition, the inclination of the binary system and the exact orbital period are usually not known. This information is crucial to distinguish between the proposed scenarios, e.g. the Lidov-Kozai effect only works for systems with an inclination above 39.2°.

5.3 The performance of Lucky Imaging compared to Adaptive Optics

Apart from Lucky Imaging, Astronomers have developed a variety of techniques to obtain high-angular resolution images, especially higher-order Adaptive Optics (AO) is widely used. In the following, I will discuss the advantages and disadvantages of this technique for observations with a similar science case. As opposed to Lucky Imaging, AO is an active technique where the wavefront distortion is measured and corrected in real-time by adjusting the shape of one of the telescope mirrors. The rate of adjustments is set by the atmospheric coherence time as for Lucky Imaging; it is about a few milliseconds in the optical (see Section 1.3). Since the Shack-Hartmann wavefront sensor uses sup-apertures with sizes about the Fried parameter r_0 and the telescope apertures for Lucky Imaging are $\approx 7r_0$, the limiting magnitude for Lucky Imaging is fainter. The use of guide stars can, however, reduce this limit considerably for AO observations.

On the other hand, the contrast of AO observations is usually higher due to the narrower resulting psf and the larger telescope aperture in use. To find companions to solar type stars in the solar neighbourhood, typically 10 s are sufficient to detect even late M-dwarfs at a 10 m-class telescope in J, H, K passbands (e.g. Ngo et al., 2015). Late M-dwarfs are out of reach for Lucky Imaging observations as the needed exposure times would be unreasonably long, mainly due to the faintness of late type stars in the i' and z' passbands compared to the near-infrared J, H, K bands, e.g. for an M8V type system

$i-J = 3.6\,\mathrm{mag}$, $i-K = 4.8\,\mathrm{mag}$, and $z-K = 3.2\,\mathrm{mag}$ (Kraus & Hillenbrand, 2007), and the use of a few percent of all integrations only. A number of late M-dwarf companions are expected around solar-type stars, even though the binary frequency of field stars drops for mass ratios smaller or equal to 0.2 (Raghavan et al., 2010), and a couple of those stars has been observed around TEP host stars, e.g. by Ngo et al. (2015). An even more important effect of the narrower psf of AO observations is the higher astrometric and photometric precision. Usually the uncertainties of the separation and position angle are a factor of 10 smaller than for Lucky Imaging observations. This facilitates the common proper motion analysis clearly and orbital motion can be seen after a much shorter time. Lucky Imaging is thus a low complexity, low cost technique at mid-size telescopes which can be used to investigate whether companion candidates are in place. It is, however, not very well suited for the characterisation of the detected sources. In the near future, Lucky Imaging will probably be replaced by RoboAO systems (Baranec et al., 2014, 2015). These automated systems at mid-size telescopes with UV guide stars will have the advantage of providing a narrower PSF and a fainter limiting magnitude.

5.4 Future Work

The discovery papers of most transiting exoplanet host stars do not include high-angular resolution images, e.g. those of WASP, HatNet, Corot or Kepler targets. Still the importance of looking for close stellar sources, whether bound or not, are now commonly recognized and a lot of groups perform ongoing follow-up surveys of stars with detected planets. So far, most WASP and HatNet planets in the North have been targeted, a few dozen of the southern targets are still missing. They are in the observing scope of AstraLux Sur (Hippler et al., 2009) or NACO (Lenzen et al., 2003) for example. As a lot of the exoplanet host stars detected from space are faint (V-band magnitudes between 13 and 17), they cannot easily be followed up with Lucky Imaging or AO observations without guide stars. This is one reason why more than half of the Corot-planets are missing such observations. A lot of the brighter Kepler exoplanet candidates have, however, been imaged by high-resolution techniques, e.g. Robo-AO observations on 715 Kepler targets with i-magnitudes up to 16 were carried out by Law et al. (2014) using an artificial guide star. 623 Kepler exoplanet candidate host stars with an average Kepler magnitude of 13 were observed by Horch et al. (2014) using differential speckle imaging at the WIYN 3.5 m telescope and the Gemini-N 8.1 m telescope, and also Lucky Imaging observations at Calar Alto, were done on 174 targets by Lillo-Box et al. (2012); Lillo-Box et al. (2014). The Kepler targets are well suited for an analysis of exoplanet properties and binarity as they come from a volume-limited sample which lack a lot of the common selection biases. One possible disadvantage of the Kepler sample might be, however, the on average larger distances of the stars which for a given angular resolution puts limits on the smallest physical binary separation which can be resolved.

Besides the transiting exoplanets, several hundred planets have been detected by the radial velocity (RV) method. The RV surveys tend to avoid close binaries due to the arising challenges in the spectral line calibration and analysis. Nevertheless, some high-angular resolution surveys have been focused on these targets, e.g. Ginski et al. (2013, 2015) using Lucky Imaging at Calar Alto (71, 62 targets, respectively) or Mugrauer & Ginski (2015) and Thalmann et al. (2014) using NACO at the VLT (33, 26 targets, respectively).

All these surveys together discovered several hundred stellar companion candidates. If orbital motion will be detected for some of the companions in the next years by multiple additional precise positional measurements, the true semi-major axis and the angle between the planetary and binary orbit can be measured, even though only a part of the orbit will be visible in most cases due to the long orbital periods. This information can then be used to infer the importance of mechanisms as the Lidov-Kozai effect (Davies et al., 2014) or resonance between the orbital motion of the binary on the orbits of the planets (Touma & Sridhar, 2015) or to restrict the true binary separation distribution.

For a precise subtraction of the amount of light that is emitted by a close stellar source, high-angular resolution measurements in the same photometric bands that are used for the transit observations or spectra would also be useful. This would allow for a better characterisation of the radius and hence composition and atmosphere of the transiting exoplanet.

Finally, binaries are also interesting targets to look for massive outer planetary companions. So far, very few high-contrast planetary searches target close binaries which leaves the population of wide, massive planets poorly constrained (Thalmann et al., 2013). In addition, Rodigas et al. (2015) showed that binary differential imaging could be an effective method to get a high contrast close to the inner working angle where most of the planets are. This technique may even outperform classical angular differential imaging depending on the observing conditions. The idea behind that approach is that the two stars are observed simultaneously with approximately the same wavefront aberrations and thus their normalized PSFs subtract out well revealing faint planetary companions.

6

Summary

The study of the multiplicity properties of exoplanet host stars and their correlation to exoplanet properties gives important insights on how planets form and evolve. In this thesis, the Lucky Imaging technique was used to look for close stellar sources around about 100 transiting exoplanet host stars in two surveys. We detect 9 previously unknown companion candidates, Five of them are within $1''$ and thus not detectable with seeing-limited surveys. We also follow up 25 companion candidates. For each detected candidate, we determine the astrometric and photometric properties and we estimate the probability that the detected stellar source is bound to the exoplanet host star by counting the stellar density in the nearby field. Even if the star is not bound, it may have biased the derivation of the properties of the close, planetary system as its light contribution to the transit light curve is then wrongly attributed to the host star. We calculate the offset due to a previously unknown companion candidate on the planetary radius of two exoplanet systems and we find that in these cases the correction is smaller than 1% and thus within the uncertainties given in the discovery papers.

For the targets with multiple observations of our first survey, we use two different statistical approaches to quantify the probability of common proper motion with the close transiting exoplanet host star. Firstly, we compute the likelihood that the companion is bound relative to that it is an unrelated background object using Bayesian analysis. Secondly, we use the Besançon *Model of stellar population synthesis of the Galaxy* to get a representative view of the stellar properties in the direction of the TEP hosts and compare their brightness and proper motion to the limits given by the observational data for each host star. The two approaches show that the majority of the detected targets are likely bound and that for a couple of targets more or more precise observations are needed to decide on common proper motion.

For about half of the observed systems, the spin-orbit angle has been measured and we compare the occurrence rate of binary stars in this subsample to field stars. Additionally, we look for a correlation between the presence of a companion star and misaligned planetary orbits. We find that the companion fraction of the observed hot Jupiter systems and field stars agrees within uncertainties. Moreover, we detect slightly more stellar companions to hot Jupiter systems with misaligned orbits. This hints at that binarity does not hinder the formation of hot Jupiter systems and that the presence of an additional stellar companion sometimes leads to spin-orbit misalignment. Yet, not all of the misaligned systems seem to be part of a binary system and thus other mechanisms cause orbital misalignment as well. The uncertainties on the companion fractions are, however, too large to draw final conclusions.

To ameliorate the above analysis, it is crucial to look for companion candidates around more hot Jupiter systems with spin-orbit angle measurements and to investigate, whether the detected companion candidates are truly bound. For this purpose, Adaptive Optics observations in the near infrared would be beneficial. Compared to Lucky Imaging, this technique allows the detection of mid to late M-dwarfs as well as more precise positional measurements. The higher precision facilitates the common proper motion analysis and it allows to detect the orbital motion of the binary after a much shorter time. The binary orbit can then be used to distinguish between different scenarios on how a stellar companion influences the orbit of the planets. In addition to that, the astrometry mission Gaia will provide more precise parallax and proper motion measurements for most, if not all, observed targets in the coming years. This will help to infer which stars are bound as well as to determine their physical separation.

Finally, I present photometric and spectroscopic observations of the young K-type binary HD 102077 for which I determine a new, amended orbit fit, the spectral type of the two components, and I revise the age and the space motion. I use these findings to discuss whether HD 102077 is part of the TW Hydrae moving group as has been proposed earlier. I show that HD 102077 properties do not fit TW Hydrae or any other young moving group.

Acknowledgements

First of all I want to thank Thomas Henning, who gave me the great opportunity to study astronomy as an "Quereinsteiger" without the usual IMPRS applications, also for his valuable ideas regarding my thesis projects. Then, but not less import, I want to thank my supervisor Wolfgang Brandner, who always took the time to discuss my projects, but also Astronomy in general. He helped me to publish my papers when I was on maternity leave and supported me whenever I needed. I also want to thank all other colleagues with whom I had the pleasure to work with, in particular Beth Biller, Carolina Bergfors, Maren Mohler-Fischer, Joshua Schlieder and Ian Crossfield. Finally, I want to thank Anton Wöllert for helping me with the layout of this thesis.

Bibliography

Adams, E. R., Ciardi, D. R., Dupree, A. K., Gautier, T. N., Kulesa, C., & McCarthy, D. 2012, AJ, 144, 42

Adams, E. R., Dupree, A. K., Kulesa, C., & McCarthy, D. 2013, AJ, 146, 9

Albrecht, S., et al. 2012, ApJ, 757, 18

Alibert, Y., Mordasini, C., Benz, W., & Winisdoerffer, C. 2005, A&A, 434, 343

Artymowicz, P., & Lubow, S. H. 1994, ApJ, 421, 651

Baglin, A., Auvergne, M., Barge, P., Michel, E., Catala, C., Deleuil, M., & Weiss, W. 2007, in Fifty Years of Romanian Astrophysics, Vol. 895, 201–209

Bakos, G. Á., Lázár, J., Papp, I., Sári, P., & Green, E. M. 2002, PASP, 114, 974

Ballard, S., et al. 2011, ApJ, 743, 200

Baranec, C., et al. 2014, in SPIE Conference Series, Vol. 9148, 12

Baranec, C., et al. 2015, IAU General Assembly, 22, 55576

Barros, S. C. C., et al. 2014, A&A, 561, L1

Baruteau, C., et al. 2014, Protostars and Planets VI, 667

Batalha, N. M., et al. 2013, ApJS, 204, 24

Bate, M. R. 2012, MNRAS, 419, 3115

Batygin, K. 2012, Nature, 491, 418

Bechter, E. B., et al. 2014, ApJ, 788, 2

Bergfors, C., et al. 2013, MNRAS, 428, 182

Borucki, W. J., et al. 2010, Science, 327, 977

Boss, A. P. 1997, Science, 276, 1836

Broeg, C., et al. 2013, in European Physical Journal Web of Conferences, Vol. 47, 3005

Burke, C. J., et al. 2014, ApJS, 210, 19

Cameron, A. G. W. 1978, Moon and Planets, 18, 5

Carter, J. A., et al. 2012, Science, 337, 556

Charbonneau, D., et al. 2005, ApJ, 626, 523

Charpinet, S., et al. 2011, Nature, 480, 496

Chatterjee, S., Ford, E. B., Matsumura, S., & Rasio, F. A. 2008, ApJ, 686, 580

Chen, X., et al. 2013, ApJ, 768, 110

Ciardi, D. R., Beichman, C. A., Horch, E. P., & Howell, S. B. 2015, ApJ, 805, 16

Cieza, L. A., et al. 2009, ApJ, 696, L84

Copernicus, N. 1543, D revolutionibus orbium coelestium

Crossfield, I. J. M., Barman, T., Hansen, B. M. S., Tanaka, I., & Kodama, T. 2012, ApJ, 760, 140

Currie, T., Daemgen, S., Debes, J., Lafreniere, D., Itoh, Y., Jayawardhana, R., Ratzka, T., & Correia, S. 2014, ApJ, 780, L30

Daemgen, S., Hormuth, F., Brandner, W., Bergfors, C., Janson, M., Hippler, S., & Henning, T. 2009, A&A, 498, 567

Davies, M. B., Adams, F. C., Armitage, P., Chambers, J., Ford, E., Morbidelli, A., Raymond, S. N., & Veras, D. 2014, Protostars and Planets VI, 787

Deacon, N. R., et al. 2015, ArXiv e-prints

Deleuil, M., et al. 2008, A&A, 491, 889

Deming, D., et al. 2013, ApJ, 774, 95

Doyle, L. R., et al. 2011, Science, 333, 1602

Dressing, C. D., Adams, E. R., Dupree, A. K., Kulesa, C., & McCarthy, D. 2014, AJ, 148, 78

Faedi, F., et al. 2013, MNRAS, 433, 2097

Faigler, S., Tal-Or, L., Mazeh, T., Latham, D. W., & Buchhave, L. A. 2013, ApJ, 771, 26

Fischer, D. A., & Marcy, G. W. 1992, ApJ, 396, 178

Fischer, D. A., & Valenti, J. 2005, The Astrophysical Journal, 622, 1102

Ford, E. B., & Rasio, F. A. 2008, ApJ, 686, 621

Fressin, F., et al. 2013, ApJ, 766, 81

Fried, D. L. 1978, JOSA, 68, 1651

Gammie, C. F. 2001, ApJ, 553, 174

Gilliland, R. L., Cartier, K. M. S., Adams, E. R., Ciardi, D. R., Kalas, P., & Wright, J. T. 2015, AJ, 149, 24

Ginski, C., Mugrauer, M., Seeliger, M., Buder, S., Errmann, R., Avenhaus, H., & Mouillet, D. 2015, MNRAS

Ginski, C., Mugrauer, M., Seeliger, M., & Eisenbeiss, T. 2012, MNRAS, 421, 2498

Ginski, C., Mugrauer, M., Seeliger, M., & Löhne, T. 2013, A&A, 559, A71

Goodwin, S. P., Kroupa, P., Goodman, A., & Burkert, A. 2007, Protostars and Planets V, 133

Guenther, E. W., et al. 2013, A&A, 556, A75

Hellier, C., et al. 2011, in European Physical Journal Web of Conferences, Vol. 11, 1004

Hippler, S., et al. 2009, The Messenger, 137, 14

Horch, E. P., Howell, S. B., Everett, M. E., & Ciardi, D. R. 2014, ApJ, 795, 60

Hormuth, F. 2007, Master's thesis, Faculty of Physics and Astronomy, University of Heidelberg, Germany

Hormuth, F., Brandner, W., Hippler, S., & Henning, T. 2008, Journal of Physics Conference Series, 131, 012051

Janson, M., Bergfors, C., Brandner, W., Kudryavtseva, N., Hormuth, F., Hippler, S., & Henning, T. 2014, ApJ, 789, 102

Johansen, A., Blum, J., Tanaka, H., Ormel, C., Bizzarro, M., & Rickman, H. 2014, Protostars and Planets VI, 547

Johansen, A., Youdin, A., & Mac Low, M.-M. 2009, ApJ, 704, L75

Kaib, N. A., Raymond, S. N., & Duncan, M. 2013, Nature, 493, 381

Knutson, H. A., Benneke, B., Deming, D., & Homeier, D. 2014, Nature, 505, 66

Kolmogorov, A. 1941, Akademiia Nauk SSSR Doklady, 30, 301

Kozai, Y. 1962, AJ, 67, 591

Kraus, A. L., & Hillenbrand, L. A. 2007, AJ, 134, 2340

Kraus, A. L., & Hillenbrand, L. A. 2009, The Astrophysical Journal, 704, 531

Lai, D., Foucart, F., & Lin, D. N. C. 2011, in IAU Symposium, Vol. 276, 295–299

Larson, R. B. 1972, MNRAS, 156, 437

Law, N. M., et al. 2014, ApJ, 791, 35

Lenzen, R., et al. 2003, in Instrument Design and Performance for Optical/Infrared Ground-based Telescopes, Vol. 4841, 944–952

Lillo-Box, J., Barrado, D., & Bouy, H. 2012, A&A, 546, A10

Lillo-Box, J., Barrado, D., & Bouy, H. 2014, Astronomy & Astrophysics, 566, A103

Lissauer, J. J., & Stevenson, D. J. 2007, Protostars and Planets V, 591

Lissauer, J. J., et al. 2011, Nature, 470, 53

Loeb, A., & Gaudi, B. S. 2003, ApJ, 588, L117

Malmberg, D., Davies, M. B., & Chambers, J. E. 2007, MNRAS, 377, L1

Masuda, K. 2015, ApJ, 805, 28

Mayer, L., Wadsley, J., Quinn, T., & Stadel, J. 2005, MNRAS, 363, 641

Mayor, M., & Queloz, D. 1995, Nature, 378, 355

Mizuno, H. 1980, Progress of Theoretical Physics, 64, 544

Moya, A., Bouy, H., Marchis, F., Vicente, B., & Barrado, D. 2011, A&A, 535, A110

Mugrauer, M., & Ginski, C. 2015, MNRAS, 450, 3127

Narita, N., et al. 2010, PASJ, 62, 779

Narita, N., et al. 2012, Publications of the Astronomical Society of Japan, 64, L7

Nelson, A. F. 2000, ApJ, 537, L65

Newton, I. 1687, Philosophiae Naturalis Principia Mathematica. Auctore Js. Newton

Ngo, H., et al. 2015, ApJ, 800, 138

Orosz, J. A., et al. 2012, ApJ, 758, 87

Pál, A., et al. 2008, ApJ, 680, 1450

Pichardo, B., Sparke, L. S., & Aguilar, L. A. 2005, MNRAS, 359, 521

Pollacco, D. L., et al. 2006, PASP, 118, 1407

Pollack, J. B., Hubickyj, O., Bodenheimer, P., Lissauer, J. J., Podolak, M., & Greenzweig, Y. 1996, Icarus, 124, 62

Rafikov, R. R. 2011, ApJ, 727, 86

Raghavan, D., et al. 2010, ApJS, 190, 1

Rauer, H., et al. 2014, Experimental Astronomy, 38, 249

Ricker, G. R., et al. 2014, in SPIE Conference Series, Vol. 9143, 20

Robin, A. C., Reylé, C., Derrière, S., & Picaud, S. 2003, A&A, 409, 523

Rodigas, T. J., Weinberger, A., Mamajek, E. E., Males, J. R., Close, L. M., Morzinski, K., Hinz, P. M., & Kaib, N. 2015, ApJ, 811, 157

Rogers, L. A. 2015, ApJ, 801, 41

Rogers, P. D., & Wadsley, J. 2012, MNRAS, 423, 1896

Röser, S., Schilbach, E., Schwan, H., Kharchenko, N. V., Piskunov, A. E., & Scholz, R.-D. 2008, VizieR Online Data Catalog, 1312, 0

Ross, T. S. 2009, Applied optics, 48, 1812

Sharma, S., Bland-Hawthorn, J., Johnston, K. V., & Binney, J. 2011, ApJ, 730, 3

Southworth, J. 2015, in Astronomical Society of the Pacific Conference Series, Vol. 496, 321

Taylor, G. I. 1938, The spectrum of turbulence

Thalmann, C., et al. 2013, in Protostars and Planets VI Posters, 12

Thalmann, C., et al. 2014, A&A, 572, A91

Toomre, A. 1981, The Structure and Evolution of Normal Galaxies

Touma, J. R., & Sridhar, S. 2015, Nature, 524, 439

Tregloan-Reed, J., Southworth, J., & Tappert, C. 2013, MNRAS, 428, 3671

Triaud, A. H. M. J. 2011, A&A, 534, L6

van Albada, T. S. 1968, Bull. Astron. Inst. Netherlands, 20, 57

Vazan, A., & Helled, R. 2012, ApJ, 756, 90

Veras, D., & Mustill, A. J. 2013, MNRAS, 434, L11

Wang, J., Fischer, D. A., Xie, J.-W., & Ciardi, D. R. 2014, ApJ, 791, 111

Welsh, W. F., Orosz, J. A., Carter, J. A., & Fabrycky, D. C. 2014, in IAU Symposium, Vol. 293, 125–132

Welsh, W. F., et al. 2012, Nature, 481, 475

Winn, J. N. 2011, in IAU Symposium, Vol. 276, 230–237

Wöllert, M., & Brandner, W. 2015, A&A, 579, A129

Wöllert, M., Brandner, W., Bergfors, C., & Henning, T. 2015, A&A, 575, A23

Wolszczan, A., & Frail, D. A. 1992, Nature, 355, 145

Xue, Y., Suto, Y., Taruya, A., Hirano, T., Fujii, Y., & Masuda, K. 2014, ApJ, 784, 66

Ziad, A., et al. 2005, MNRAS, 362, 455